MATHEMATICAL MODELLING OF MOVEMENT AND GLIOMA INVASION

by

Radhia Eljazi

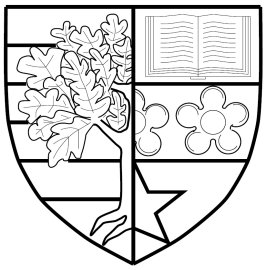

Submitted for the degree of
Doctor of Philosophy

Department of Mathematics
School of Mathematical and Computer Sciences
Heriot-Watt University

October 2016

Abstract

Modelling movement is an important topic in fields ranging from ecology to medicine. In particular, glioma, an often fatal brain tumour is characterised by its diffuse invasion into the surrounding normal brain tissue, enabling the tumour to escape therapy. In this thesis we focus on the mathematical modelling of glioma and movement in general. We begin by exploring the basic structure of the brain, describing glioma classification and the hallmarks of cancer as well as reviewing mathematical models of glioma. In Chapter 2 an Ordinary Differential Equation model is presented to describe the interaction between healthy and mutated cells in vivo and vitro scenarios. The model is extended to a Partial Differential Equation to cover the spatial dynamics of interaction and the possibility of travelling wave solutions. A leading hypothesis suggests that malignant glioma cells switch between proliferating and migrating phenotypes, a mechanism known as the "go or grow" hypothesis. Although the molecular mechanisms that control this switch are uncertain, it is generally assumed to depend on micro-environmental factors. In Chapter 3 we propose a simple mathematical model based on the go or grow hypothesis for brain tumours (gliomas). The model describes the competition between healthy glial cells and malignant cells, with the latter subdivided into invasive and proliferating subpopulations. Simulation and stability analysis is performed for spatial and non-spatial versions of the model. The model incorporates two types of switch between migration and proliferation glioma cells: a constant switch form and a density dependent form. In Chapter 4 we present a framework for modelling a different characteristic movement lengths based on a biased random walk in response to external control species. We use the model to understand different strategies by which a population may locate some resource in its environment. Further we consider a pilot application to glioma, showing how it can be used to model movement along different brain structures. Finally we conclude with a brief discussion that summarises the main results and highlights directions for future work.

Acknowledgements

My deepest appreciation goes to my supervisor Dr. Kevin Painter for his endless guidance, insightful suggestions and encouragement he has provided throughout my time as his student. This thesis would not have been possible without his extraordinary support.

Contents

Chapter 1

Introduction

According to the World Health Organisation [105], 8.2 million people die each year from cancer, approximately the population of London, and an estimated 13% of all deaths worldwide, but the key question is "What is Cancer?". Cancer is the name given to any disease caused by uncontrolled growth and spread of abnormal cells and, while it is often difficult to determine the exact cause that resulted in a particular cancer, numerous researches have provided a number of factors that lead to a greater chance of a cancer developing, including chemical and toxic compounds, radiation, smoking, diet and genetic predisposition [2].

There are well over a 100 types of cancer, and any part of the body can be affected. At a general level, cancers are classified according to their embryonic tissue of origin: for example, **carcinomas** are cancers derived from epithelial cells, while **sarcomas** arise from mesenchymal cells. Subsequent naming of cancers can be considered according to their organ and cell-type of origin: for example, while brain tumours comprise of a large number of different tumours that can originate from the many different cell types of the brain, **gliomas** represent those brain tumours that arise from the brain's glial cells, while **astrocytomas** correspond to those gliomas that specifically arise from the astrocytes, a specialised type of glial cell. Within specific names, tumours are often further subclassified according to their degree of malignancy, a clinical classification made on the basis of tissue samples obtained via biopsy. Further classifications of cancers include primary and secondary, with the former referring to the cancer formed at the original site, and the latter the result

of a metastasis from a cancer elsewhere in the body [102, 125].

1.1 Basic brain structure and cancers of the brain

The brain is amongst the most complex organs of the human body and, along with the spinal cord, comprises the body's central nervous system (CNS). A remarkable feature of the brain lies in great heterogeneity, with distinct regions of the brain classified according to their location and function (e.g. frontal, parietal, occipital and temporal lobes, cerebellum, hippocampus etc.) or the tissue structure (e.g. gray or white matter). In terms of the latter,gray matter is more dominated by the unmyelinated neuron cell bodies, while white matter is mainly composed from myelinated nerve fibers, or axons. In fact, it is this myelin that gives white matter its lighter shade under histological sectioning, and hence motivates the naming of these two principal tissue types. These axons transmit information between the control region (grey matter) and other parts of the body.

Gliomas form the most dominant class of primary brain tumour, arising from the supporting glial cells [98, 108] that provide the majority of cells of the central nervous system: while figures vary, glial cells are thought to make up to around 85 percent of the brain's cells and more than half its volume [32, 66]. Various types of glial cells exist, including oligodendrocytes, astrocytes, ependymal cells, Schwann cells, microglia, and satellite cells, which play various roles from supporting neurons to tissue repair. Gliomas are classified by their originating cell type (for example, astrocytoma, brainstem glioma, ependymoma, mixed glioma, oligodendroglioma and optic nerve glioma), their grade (low-grade or high-grade) and by location [93, 97].

Gliomas may remain undetected for a considerable length of time before resulting in symptoms leading to their diagnosis: classic symptoms include headaches, facial paralysis, double vision, dizziness, memory loss and lack of recognition. Diagnosis typically involves a scan, for example computed tomography (CT)-scans or magnetic resonance imaging (MRI), followed by a biopsy that allows a formal classification of tumour type and grade. Despite the improvements of diagnostic imaging and treatment in recent years, treatment of malignant gliomas remains difficult, even

following extensive surgery to remove the majority of the tumour. Treatment of brain tumours typically involves resection of the tumour mass, followed by radiotherapy and/or chemotherapy. Recurrence of the tumour around the edge of the resection area results in regrowth [60, 64], and a low mean survival time (order of a year) [107, 5] for high grade (i.e. malignant) gliomas. This poor prognosis has been attributed to the highly invasive and diffuse nature of gliomas, in that a significant fraction of tumour cells travel far from the main tumour mass and remain undetected. Gliomas, and indeed tumours more generally, are typically believed to arise through a multistep development process due to mutations in normal cells. For example, the review of Hanahan and Weinberg [50], see Figure 1.1, detail a number of cancer hallmarks, thereby potentially allowing their therapeutic targeting. Some of these hallmarks of cancer include:

- **Self-sufficiency in growth signal**: normal cells require extracellular growth signals (factors) to grow and divide, detected and internalised through transmembrane receptors, with cell growth ceasing when these signals are absent. As such, growth of normal cells can be closely regulated via the surrounding molecular environment. Certain cancer cells, on the other hand, may not require any external signals to grow or divide: they can produce their own growth factor, leading to unregulated growth.

- **Insensitivity to anti-growth signals**: growth inhibitors in the surrounding environment also act to keep the growth of normal cells under control through blocking cell division, with inhibitors transmitted through the PRB (the retinoblastoma protein) pathway. Mutations/damage to PRB can lead to insensitivity of the cell to these inhibitory signals, unlimited division and formation of a cancerous colony.

- **Evading apoptosis**: Programmed cell death (apoptosis) is a key component of a cell's normal behaviour, and can be triggered by, for example, adverse conditions (e.g. low oxygen) or imperfect cell division. Apoptosis therefore helps to control the normal number of cells in the environment and prevents the accumulation of damaged cells. Disruption in the signalling pathways

leading to apoptosis can lead to a greater population of cancer cells, as well as increasing the risk of further mutation.

- **Limitless reproductive potential**: while many normal cells have a limited proliferative potential before death, certain cancer cells may not be restricted by a certain number of divisions, again allowing unrestricted growth of the cancerous population and greater risk of further mutation.

- **Sustained angiogenesis**. The normal capillary network provides a natural brake on the supportable population of cells in the environment: once the oxygen/nutrient level is depleted, cell growth is inhibited. The capacity of cancer cells to trigger new blood vessel growth, **Angiogenesis**, can act to increase the oxygen supplied.

- **Tissue invasion and metastasis**. The capacity of certain cancer cells to migrate, allows infiltration of the tumour into surrounding healthy tissue, and, potentially, tumour metastases appearing distance from the primary tumour mass.

1.2 Overview of mathematical models of gliomas

Mathematical modelling of cancer growth has grown into a large and diverse field, with models aimed at tackling phenomena ranging from the mechanisms that control basic tumour growth to the detailed modelling of specific therapeutical interventions. It is not our aim to provide a comprehensive review on all these different aspects, rather we aim to provide an overview of the field: for reviews, see [68, 126, 26, 15].

A realistic mathematical model can play an important role in simplifying and understanding biological phenomena. A beneficial mathematical model is one that matches the model to experimental data and leads to meaningful biological interpretation and future resolution of the biological problem. Moreover, by proposing a new hypothesis that can be proven by experiments, a model can become a core component in advancing knowledge of a problem [116]. Mathematical models that

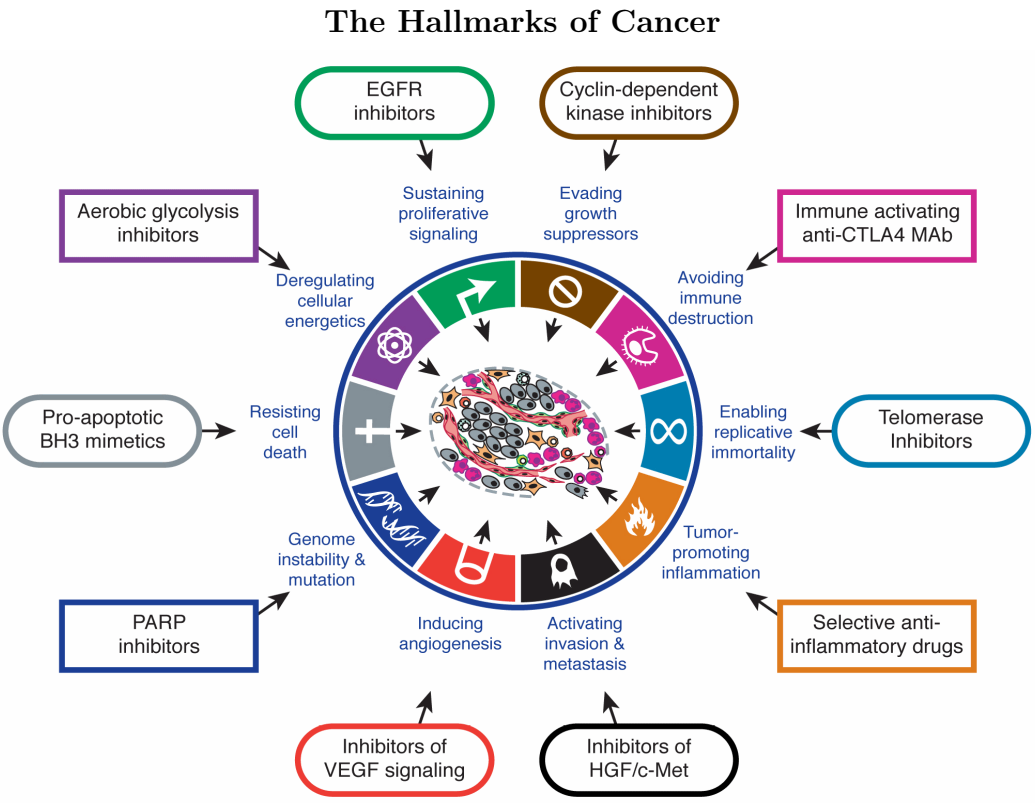

Figure 1.1: This figure, from [[50], Figure 6], illustrates cancer hallmarks with the therapeutics targeted to the known and emerging hallmarks of cancer. EGFR indicates epidermal growth factor receptor; CTLA4, cytotoxic T lymphocyte-associated antigen 4; mAb, monoclonal antibody; HGF, hepatocyte growth factor; VEGF, vascular endothelial growth factor; PARP, poly-(ADP ribose) polymerase.

fail to reflect new biological data can be modified to incorporate additional features. At the same time, any model should be considered with justifiable caution.

A number of mathematical models have attempted to characterise and predict the complex behaviour of glioblastoma tumour cells in either *in vitro* or *in vivo* settings: for good reviews, see [53, 76]. Gliomas are multiscale phenomena, with processes ranging from molecular and cellular (i.e. microscopic scales) to cellular interaction with the local tissue environment (mesoscopic scales) to whole-organ level (macroscopic scales). Mathematical models have attempted to describe all of these aspects, as well as the role of nutrients, brain geometry, treatment etc. A variety of forms of mathematical model have been developed, from continuous systems of ordinary differential equations to partial differential equations, along with discrete (agent-based) models and statistical models.

As examples, Alarcon et al [3] have studied a multiple scale model for intracellular scale problems, including at the molecular scale aspects such as gene mutation and cell cycle, and at the cellular scale, cell-cell interaction and vascular tumour growth. Modelling the early growth of tumour cells in vitro have been studied with variety of different types of models, such as stochastic Gompertz-like mathematical models [21]. Tracqui et al.[120] developed the earliest reaction-diffusion models of glioblastoma growth and diffusion, a work expanded on by Swanson et al [115] to take into account the spatial heterogeneity of the brain tissue. Reaction diffusion models have also take into account the separation of a particular population into subpopulations of proliferative and invasive cells, for example [110], due to their highly different behaviours. These models have been highly beneficial in estimating the size of model parameters related to basic tumour dynamics.

In the specific context of tumour dynamics, Gatenby [36, 34] used a competition model to investigate tumor-host interaction and treatment strategies. The model parameters identify the stage of tumour growth which can be translated into clinical factors, that predict the successful of treatment strategy. The model has been extended to investigate many biological behaviors, for example acid-mediated tumour invasion, where the acidic environment facilitates normal cell death and permits

tumour invasion [37, 38, 74, 79] and wavefront propagation in a competing cancer cells concept [41].

A number of models have modelled the different phases of tumour growth, such as avascular against vascular growth. Greenspan [48, 49] formulated an avascular tumour growth model as a moving boundary problem, while continuum models for vascular growth have been developed by Chaplain and others [16, 84]. The problem of invasion/infiltration of tumours into healthy tissue has been modelled by many, with models incorporating the many factors believed to play a role in invasion, including cell-cell adhesion, cell-matrix adhesion, chemotaxis, haptotaxis etc: for examples, see [121, 62, 88]. In the context of brain tumour invasion, a number of models have explored the differential invasion along different brain structures: glioma cells have been found to move along white matter fiber tracts[42], which can be imaged via Diffusion Tensor Imaging (DTI) [24]. Jbabdi [58] proposed to use diffusion tensor imaging data to simulate anisotropic growth of glioma.

Modelling the various forms of therapy has formed a particularly active are of research. In the context of gliomas, the impact of resection of the tumour has been investigated by [127, 113, 28]. Radiotherapy effects have been included in the studies by [92, 118, 114], while the impact of chemotherapy on spatio-temporal growth has been investigated in [120, 109].

1.3 Thesis outline

In this introduction we highlighted medical background of gliomas and presented an overview some of the mathematical models used to understand them. Chapter 2 presents a review of core mathematical techniques and their application to a simple model of glioma growth. In Chapter 3, we develop a model for the go-or-grow hypothesis of gliomas within a healthy tissue mathematical model. Chapter 4 presents multi step jumps of movement mathematical models based on random walk movement in response to multiple control species, a framework which is subsequently applied to heterogeneous glioma invasion. In Chapter 5 we conclude the thesis with a discussion and present ideas for future work.

Chapter 2

Core mathematical techniques and a simple model of glioma growth

In this chapter we review core mathematical tools and techniques and apply them to a purposely simple model for glioma growth, subject to competition from a healthy tissue. We start with a brief review of ordinary differential equation models and consider their stability and phase plane analysis. Subsequently, we proceed to consider the modelling of spatial movement processes, motivating them from either classical continuum descriptions or as a limit arising from underlying random walk processes. The goal of this chapter is to describe the modelling of gliomas and highlight how the various mathematical tools reviewed can lead to some core insights of the model equations, and explore how changes to the key parameters can lead to different invasion profiles. Having provided this review of core theory, we illustrate their application in a simplistic model for glioma growth within a healthy tissue.

2.1 A simple ODE model for glioma growth and a review of core analytical techniques

2.1.1 Introduction

Mathematical modelling of glioma growth dates back to the early 1990s [81, 119, 115, 14]. Time-only models attempt to capture the temporal growth of tumour cells,

which are typically assumed to follow exponential, Gompertzian, or logistic growth [77]. In many time-dependent phenomena, a common modelling technique is to propose a system of governing ordinary differential equations (ODEs). Significantly, we can then utilise a wide variety of tools and techniques, such as linear stability and phase plane analysis, to obtain a generic understanding into the behaviour of such equations. In this section we formulate a simple model for glioma growth within a healthy tissue environment and examine its properties via standard stability analyses. At the same time, we review and summarise these core techniques that will be subsequently exploited in the remaining thesis chapters.

2.1.2 Healthy tissue dynamics

The brain is probably the most complex and magnificent organ in the human body, and is principally composed of two main cell types, nerve cells and glial cells, with the latter generally considered to be more numerous [55]: a figure of 10 glial cells to every neuron is widely quoted, although the exact ratio still remains unknown and varies considerably between different brain regions [59]. It is widely believed that tumours develop from mutations that arise in single or a few cells within a normally functioning tissue. Here we shall focus on the brain tumours, and in particular gliomas, which make up to 80% of all malignant brain tumours [47]. Yet the "success" of a mutated cell (or cells) will be subject to its capacity to acquire sufficient nutrient and oxygen from its tissue environment: since all cells have some level of nutrient demand, there will inevitably be competition between the cells for any available nutrient. We denote our normal glial cell population by $n(t)$ and assume its dynamics, in the absence of mutated cells, is modelled by a standard logistic-type growth equation of the form

$$\frac{dn}{dt} = r_1 n \left(1 - \frac{n}{k_1}\right), \tag{2.1}$$

with initial condition

$$n(0) = n_0.$$

In the above, the first term describes a logistic growth term whereby cells divide at a rate $r_1\left(1-\frac{n}{k_1}\right)$: here, r_1 $(1/time)$ defines the maximum growth rate of the cells, while the parameter k_1 $(cells/volume)$ determines a population carrying capacity, the population density at which competition between the healthy cells for any available nutrient reduces the growth rate of cells to zero. Note that in the above we assume any death of cells is effectively absorbed into this competition, i.e. for cell densities $n > k_1$ competition between the cells becomes significantly strong as to lead to a negative growth rate and cell death. For the purposes of this simpler model we do not state explicit dimensional units for our variables, although to provide context we would note that if our cell density is measured in $(cells/mm^3)$ then an approximate value for the carrying capacity, based on estimates of normal glial cell densities, would be $k_1 = 8.5 \times 10^5$ $cells/mm^3$ in the anterior cingulate cortex (grey matter), where glial cells are more numerous than neurons [25]. We note that an explicit extra term to describe background cell death could also be included in the model, however we ignore this for simplicity.

The logistic equation was first used to describe human population in 1838 by Verhulst [123] before being revived by Pearl and Reed in 1920 [90]; for more details see Britton [13]. Through separating variables, equation (2.1) can be solved explicitly to yield:

$$n(t) = \frac{k_1 n_0 e^{r_1 t}}{k_1 - n_0 + n_0 e^{r_1 t}}.$$

A sketch of typical solutions is provided in Figure 2.1: it shows an increase with $n(t) \to k_1$, if the starting population is less than the carrying capacity k_1, while if the population exceeds the carrying capacity the population decay to $k1$, presumably due to limited nutrient/oxygen.

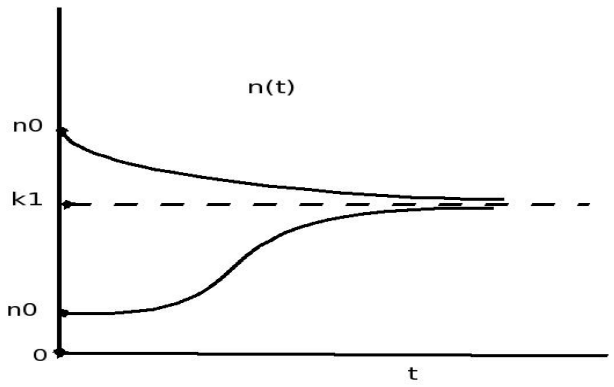

Figure 2.1: Illustration of the analytical solution of the logistic equation. The initial population n_0 increases or decreases to its carrying capacity k_1 with time t.

Rather than deal with the dimensional model, we nondimensionalise to reduce the number of parameters into convenient and dimensionless groupings. Specifically, we rescale by introducing new dimensionless variables as follows:

$$n^* = \frac{n}{k_1}, \qquad t^* = r_1 t.$$

The dimensionless form (after dropping the stars) is:

$$\frac{dn}{dt} = n\,(1-n)\,. \tag{2.2}$$

Stability analysis (see Appendix A.1) is performed about the steady states, i.e. the solutions to

$$\frac{dn}{dt} = n\,(1-n) = f(n) = 0$$

which gives "trivial"and "healthy"steady states $n = 0$ and $n = 1$. Linearization about the steady states gives

$$f'(0) = 1 > 0 \qquad \text{and} \qquad f'(1) = -1 < 0,$$

where $'$ denotes the derivative with respect to n, implying that the trivial steady state $n = 0$ is unstable while the healthy tissue steady state is stable.

2.2 Competition model for healthy-mutated interactions

To explore the impact of a mutated population on the normal tissue, we adapt model (2.1) by including an additional mutated population $p(t)$. Fundamentally we assume that the mutated population differs with respect to the underlying parameters that characterise its dynamics, such as its growth rates and its capacity to "compete" for nutrients (see Section "Hallmarks of cancer", Chapter 1). However, since both the healthy and mutant cell populations will be competing with each other for the same resources, such as oxygen and nutrient, we extend to a standard competition-type model as follows:

$$\begin{aligned} \frac{dn}{dt} &= r_1 n \left(1 - \frac{n}{k_1} - a_1 \frac{p}{k_2}\right); \\ \frac{dp}{dt} &= r_2 p \left(1 - \frac{p}{k_2} - a_2 \frac{n}{k_1}\right). \end{aligned} \tag{2.3}$$

The theory of competition for the same limited food source has been widely used in nature [4]. Lotka [71] and Volterra [124] first proposed a similar model subsequently coined the *Lotka-Volterra model* which has subsequently been extensively applied to ecological population dynamics [112]. In the specific context of tumour dynamics, Gatenby [36, 34] used the model (2.3) to investigate tumour-host interactions and treatment strategies. Gatenby analysed the model under conditions which simulate tumour development. The model parameters identify the stage of tumour growth which can be translated into clinical factors, that predict the success of treatment strategy. The model showed that tumour survival solely depended on host-generated effects. The model has been extended to investigate many further biological behaviors, for example: acid-mediated tumor invasion, where the acidic environment increases normal cell death and facilitates tumour invasion [37, 38, 74, 79], and wavefront propagation under a competing cancer cells concept [103, 41].

In the above model r_1 and r_2 are the proliferation rates of healthy and mutant cells respectively. The parameter k_1 describes the carrying capacity of normal cells in the absence of mutant cells, while k_2 describes the carrying capacity of mutant cells in the absence of normal cells: effectively, these parameters describe "self-competition":

if $n = k_1$ and in the absence of mutant cells, then competition between normal cells reduces their net growth rate to zero; correspondingly, if $p = k_2$ and in the absence of normal cells, then competition between mutant cells reduces their net growth rate to zero. In the above formulation the parameters a_1 and a_2 are nondimensional parameters representing the negative impact on growth due to competition, respectively, for the mutant cells on the growth of normal cells and the normal cells on the growth of mutant cells.

2.2.1 Parameter discussion

We provide a brief discussion of potential parameter values, ranges and ratios. Due to the variability in different regions of the brain, or the variability between different mutant population types, parameters have the potential to vary enormously. For example, supposing our timescale be in weeks, then doubling times for gliomas have been found to vary between 1 week and 48 weeks [5] according to the grade and type of gliomas: a value of $r_2 \sim 0.087$/week would correspond to a maximum doubling time for the mutated population of 8 weeks, but clearly r_2 could vary considerably. Similarly, based on the earlier reported value for the normal glial cell density we would take $k_1 = 8.5 \times 10^5$ cells/mm^3 to generate (in the absence of the mutated population) a typical healthy tissue, however k_1 could vary significantly in different tissues (e.g. gray or white matter) or different brain regions.

For the purposes of our study we are less interested in absolute values and more interested in the *differences* between the healthy and mutated subpopulations: e.g. the ratio between mutated and healthy cell growth rates (r_2/r_1), the ratio between mutated and healthy cell carrying capacities (k_2/k_1). For these we take into account the following considerations:

- Mutated tumorous populations are often characterised by their greater proliferative capacity over the normal cells. Therefore, we generally expect $r_2 \geq r_1$.
- Mutated tumorous populations typically grow to higher densities than normal cells, for example due to the capacity to avoid apoptosis at low oxygen levels.

Consequently, we would often expect $k_2 > k_1$. Note that this higher density achievable by tumour cells is often a key factor in their detectability: for a glioma to be detectable via medical imaging, a threshold of some $40,000$ $cells/cm^2$ [115] is required.

- Competitive interactions will be a result of various factors: for example tumorous cells may have an upregulated molecular profile that allows them to capture more of the nutrient at the expense of normal cells, or be more resistant to the poisonous environment created via higher metabolism. Overall, we would expect "successful" mutant populations to be better at competing, such that $a_1 \geq 1$ and/or $a_2 \leq 1$.

2.2.2 Nondimensionalisation

Bearing in mind the above considerations regarding potential parameter values, in order to reduce the total number of free parameters we rescale as follows:

$$n^* = \frac{n}{k_1}; \qquad p^* = \frac{p}{k_2}; \qquad t^* = r_1 t; \qquad b = \frac{r_2}{r_1}.$$

The dimensionless form of model (2.3) (after dropping the stars) is then:

$$\begin{aligned} \frac{dn}{dt} &= n\left(1 - n - a_1 p\right); \\ \frac{dp}{dt} &= bp\left(1 - p - a_2 n\right). \end{aligned} \tag{2.4}$$

We note that each of the cross-competition parameters a_1 and a_2 are unchanged as a result of the nondimensionalisation. For example, at $a_1 = 1$ the presence of mutant cells reduces growth of both the normal cells and mutant cells at the same rate; for values $a_1 > 1$ the mutant cells negatively impact normal cells more than themselves; for values $a_1 < 1$ the mutant cells negatively effect themselves more than the normal cells.

2.2.3 "In vivo" and "in vitro" simulations

From our above discussion, parameters clearly can vary hugely according to the factors such as the nature of the mutated population and the location where the mutation takes place. To understand the growth dynamics capable from model (2.4) we start with a broad numerical study across a range of parameter values for two scenarios:

- A simulated "*in vivo*" situation, in which we initiate the two populations with the healthy population at its carrying capacity and introduce a small number of mutated cells as follows:

$$n(0) = 1 - \epsilon \quad \text{and} \quad p(0) = \epsilon. \tag{2.5}$$

  The above could either describe the dynamics beginning from an initially small tumour, or the beginning condition in an experiment where a cluster of mutated cells have been implanted into a normal brain environment.

- A hypothetical "*in vitro*" situation, simulating a situation in which two small and equal populations of healthy and mutated cells are co-cultured in an *in vitro* environment replicating a tissue environment.

$$n(0) = \epsilon \quad \text{and} \quad p(0) = \epsilon. \tag{2.6}$$

For each case we consider nondimensional parameters over the following ranges:

- For b we consider values $b \in [0.5, 2]$: i.e. the mutated population divides at a rate of half to 2 times that of the normal population:

- For a_1 and a_2 we consider values $a_{1,2} \in [0.25, 2]$: i.e. the cross-competition parameters allow the impact of the mutant (healthy) population on the healthy (mutant) to range from less to more competitive.

Note that in the above we have allowed parameters outside the ranges suggested by our intuition above: this is to allow us to also evaluate the impact of cases where the

mutant cells may have dual parameter changes: for example, a mutant population could be more resistant (and hence more competitive), but at the expense of a slightly reduced growth rate.

2.2.3.1 Simulation study 1: "In vivo" case

For the "in vivo" scenario our investigation will focus on addressing the following question:

- Does the mutant population come to dominate and, if so, how quickly?

To investigate this, we numerically solve equations (2.4) across the parameter ranges specified in the above section and for the "in vivo" initial conditions (2.5): note that here we set $\epsilon = 0.0001$. We stop all of our simulations at $t = 100$, regardless of whether the system has reached a steady state: while somewhat arbitrary, we note that based on our earlier time rescaling and assuming normal glial cell turnover is somewhat slow (e.g. the order of months), then $t = 100$ would represent years to decades of potential growth. As a suitable measure for the above question for each simulation we plot T_p: defined as the time taken for the mutant population to overcome the normal population, i.e the first time t^* such that $p(t^*) \geq n(t^*)$. If this does not happen by $t = 100$, we set $T_p = \infty$.

Figure 2.2 shows the time evaluation of the model (2.4) with initial conditions (2.5) for different values of proliferative ratio $b = [0.5, 1.0, 2.0]$, and mutant competition value $a_1 = [0.25, 0.5, 0.75]$. We fixed the healthy cells competitive value a_2 at 0.5. Numerical findings suggest for $a_2 < 1$: the tumour grows for all sets of values. Even when $b < 1$, the tumour eventually overtakes the normal cells. The time rate of tumour growth is associated with b, such that the minimum time required for tumour cells to exceed normal cells decreases as the proliferative ratio b increases. The final density of tumour cells correlates with the competitive rate of tumour cells a_1, such that the tumour density increases as the competitive rate of tumour cells a_1 increases. Moreover, the time for tumour cells to reach the coexistent steady state depends on the proliferative ratio b and the tumour cells exceed the amount of normal cells more quickly when b is higher.

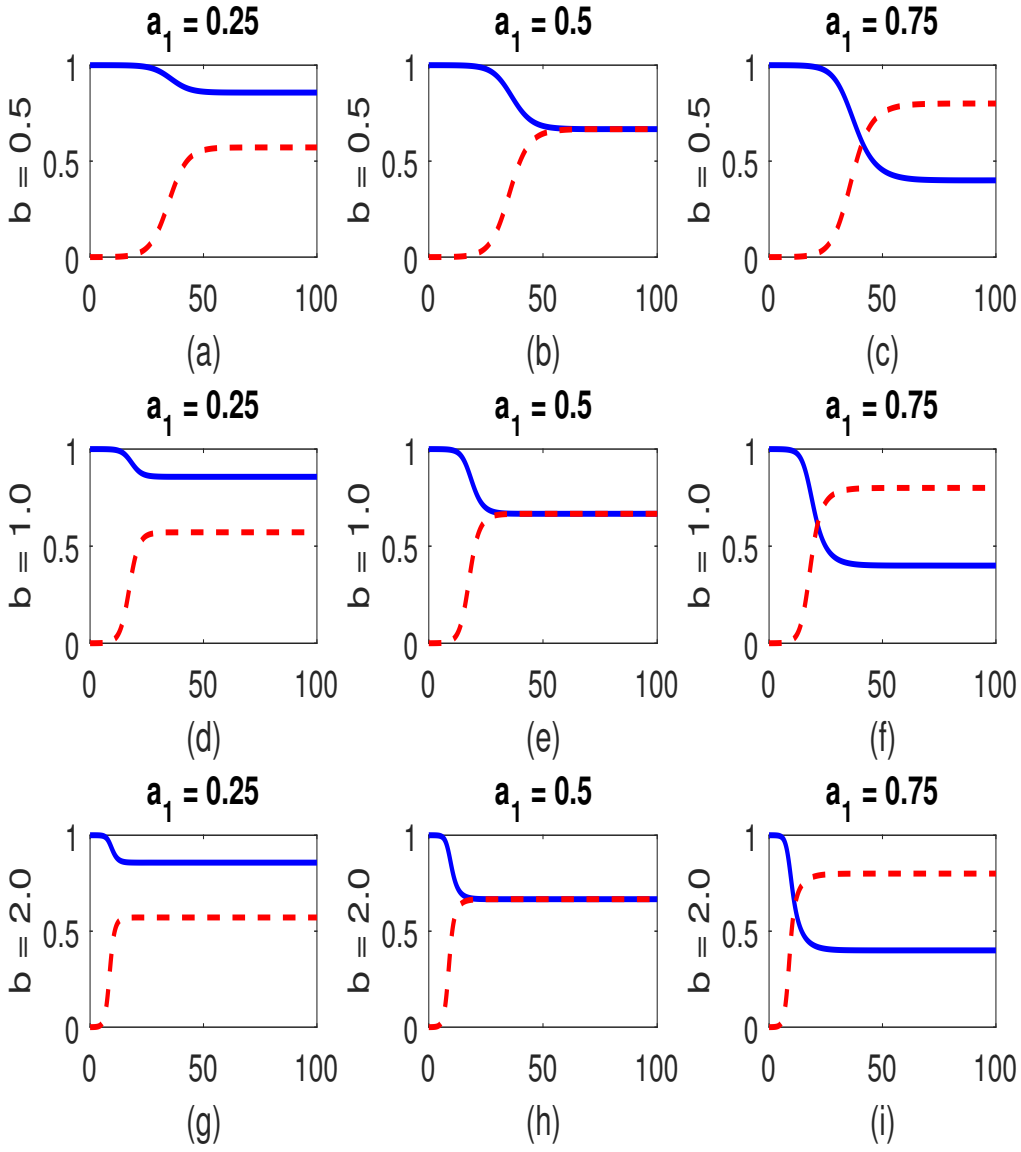

Figure 2.2: Numerical simulations of model (2.4) with initial conditions (2.5) for different values of b, a_1 and fixed $a_2 = 0.5$. We plot normal cells (blue solid) and mutant cells (red dashed) as functions of time $0 \leq t \leq 100$. (a) $b = 0.5, a_1 = 0.25$. (b) $b = 0.5, a_1 = 0.5$. (c) $b = 0.5, a_1 = 0.75$. (d) $b = 1.0, a_1 = 0.25$. (e) $b = 1.0, a_1 = 0.5$. (f) $b = 1.0, a_1 = 0.75$.(g) $b = 2.0, a_1 = 0.25$. (h) $b = 2.0, a_1 = 0.5$. (i) $b = 2.0, a_1 = 0.75$. The equations were solved numerically using the ODE solver "ode15s" in Matlab, with relative tolerance 10^{-6} and absolute tolerance 10^{-9}.

Since the tumour parameters are important for the rate of taking over the normal cells, we plot the minimum time that the tumour needs to exceed the normal cells for a_1 vs b in Figure 2.3. We find that a longer time is required when b is low, i.e when the proliferative rate of tumour cells is half that of the normal cells. While b significantly impacts on the time for takeover, there is relatively slight variation in the time required of tumour cells to take over normal cells as we vary the competitive rate a_1.

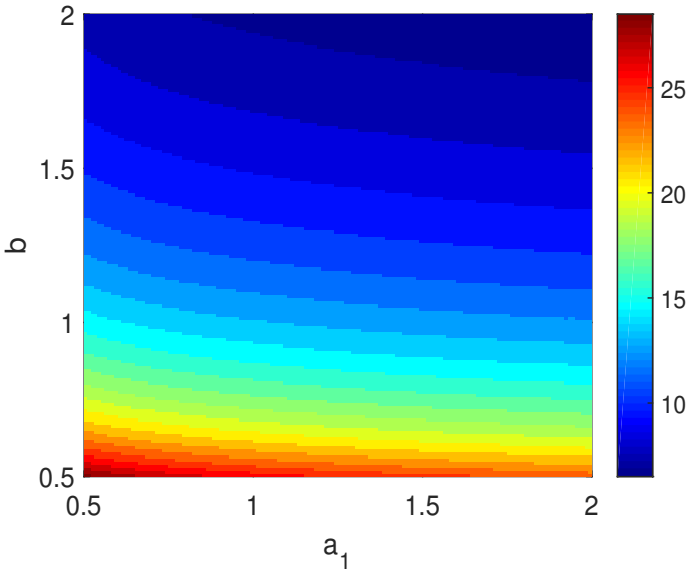

Figure 2.3: Plot of the minimum time T_p that the tumour needs to exceed the normal cells for a_1 vs b. Here, we set $a_2 = 0.25$. Numerics performed as in Figure 2.2.

To investigate the impact of the competition rates a_1 and a_2 on the growth of tumour cells, we calculate the final ratio of the two cell populations $p(t)/n(t)$ and the time taken for the mutant population to overcome the normal population, T_p, of the model (2.4) with initial conditions (2.5) on time interval $t \in [0, 100]$. At different values of the proliferative ratio $b = [0.5, 1, 2]$, we plot T_p in the first row and in the second row we plot $\log_{10}(p(100)/n(100))$ for a_1 vs a_2, see Figure 2.4. Moving right through the columns in the first row ((a), (b), and (c)), we observe a decrease in the time taken for mutant cells to exceed the normal cells T_p. We note that if $a_2 > a_1$ the number of mutant cells remain below the number of normal cells, while increasing b allows the mutant cells to exceed the normal cells in less time when $a_1 > a_2$. Moving right through the columns in the second row ((d), (e), and (f)), we

observe a slight increase in the number of mutant cells.

2.2.3.2 Simulation study 2: "In vitro" case

For the "in vitro" scenario our investigation will focus on the following question:

- What is the final ratio of the two cell populations?

To investigate this, we numerically solve equations (2.4) across the parameter ranges specified in the above section and for the "in vitro" initial conditions (2.6): note that here we set $\epsilon = 0.0001$. We stop all of our simulations at $t = 100$, regardless of whether the system has reached a steady state: while somewhat arbitrary, we note that based on our earlier time rescaling and assuming normal glial cell turnover is somewhat slow (e.g. the order of months), then $t = 100$ would represent years to decades of potential growth. As a suitable measure for the above question, for each simulation we calculate the ratio of mutant to healthy cells, $p(t)/n(t)$ at two times $t = 10$ and $t = 100$. Values of this $\to 0$ would correspond to healthy population winning, while values of this $\to \infty$ would correspond to mutant population winning. In Figure 2.5 we present $\log_{10}(p(10)/n(10))$ in the first row, and $\log_{10}(p(100)/n(100))$ in the second row. Moving right through the columns in the first row ((a), (b), and (c)), we observe an increase in the number of mutant cells as we increase the growth ratio b. Moving right through the columns in the second row ((c), (d), and (e)), we do not observe a notable difference in the number of mutant cells as we increase the growth ratio b. Moving down through the rows, we observe a difference in mutant cells number between early and later times. When the growth rate of mutant cells is twice that as normal cells, the number of mutant cells exceeds the normal cells in earlier time, and then drops with time, see Figure 2.5 (c) and (f).

Remark: we observe that in vivo case, the proliferative ratio b has a minimal impact on increasing the number of tumour cells. However, for the in vitro case, the tumour density is increased as the proliferative ratio b increases, especially at earlier times. In Figure 2.6 we plot the tumour density number at times $t = 10$ and $t = 100$ for different values of proliferative ratio $b = [0.5, 2]$. For the in vitro case we observe greater variation in tumour density as b increases. Furthermore, the tumour

cell density drops at later time when $b \leq 1$ (i.e the proliferative rate of tumour cells is higher than for normal cells).

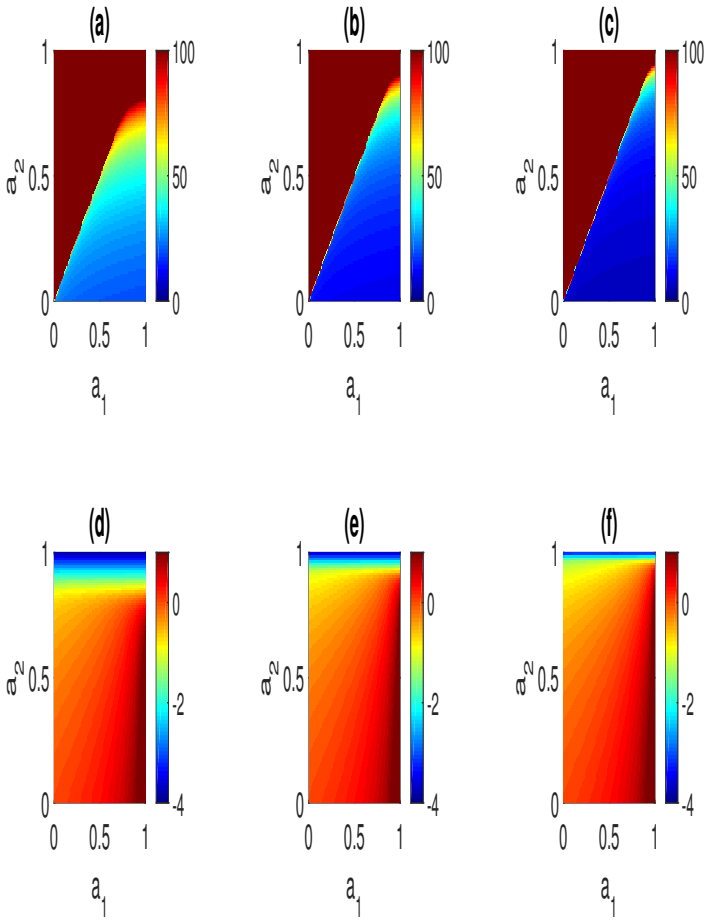

Figure 2.4: Simulations of model (2.4) with initial conditions (2.5). First row ((*a*), (*b*) and (*c*)) is an illustration of the time taken for the mutant population to overcome the normal population T_p for a_1 vs a_2 at different values of b (a) $b = 0.5$, (b) $b = 1$, (c) $b = 2$. Second row ((*d*), (*e*) and (*f*)) is an illustration of the $\log_{10}$ ratio of mutant to healthy cells, $p(100)/n(100)$ for a_1 vs a_2 at different values of b (d) $b = 0.5$, (e) $b = 1$, (f) $b = 2$. Numerics performed as in Figure 2.2.

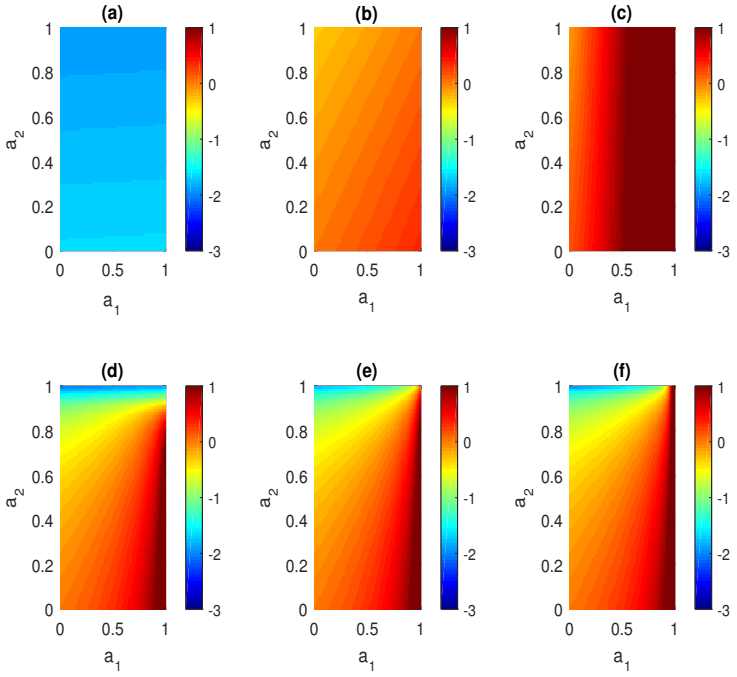

Figure 2.5: Simulations of model (2.4) with initial conditions (2.6). First row ($(a), (b)$ and (c)) is an illustration of the $\log_{10}$ ratio of mutant to healthy cells at time $t = 10$, $p(10)/n(10)$ for a_1 vs a_2 at different values of $b = 0.5, 1, 2$ respectively. Second row ($(d), (e)$ and (f)) is an illustration of the $\log_{10}$ ratio of mutant to healthy cells at time $t = 100$, $p(100)/n(100)$ for a_1 vs a_2 at different values of $b = 0.5, 1, 2$ respectively. Numerics performed as in Figure 2.2.

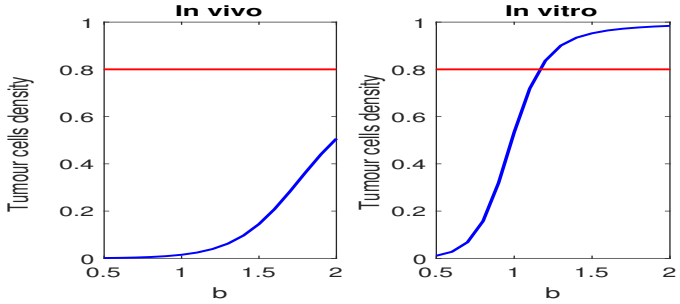

Figure 2.6: Simulations of model (2.4) with initial conditions (2.5) and (2.6). Blue line represents the tumour cell density at time $t = 10$, and red line represent the tumour cell density at time $t = 100$. For fixed $a_1 = 0.75$ and $a_2 = 0.5$. Numerics performed as in Figure 2.2.

2.2.4 Stability analysis

While simulations yield some insight into the types of parameters where the mutant population may infiltrate, a more formal approach is to use analysis such as linear stability analysis. Details of linear stability analysis for two-species ODE systems are provided in Appendix A.2. In the context of equations (2.4), we first set the left hand side terms to zero and solve for n and m to yield four steady states:

(SS1) $(0,0)$. (trivial - no cells)

(SS2) $(1,0)$. (healthy tissue)

(SS3) $(0,1)$. (fully mutated tissue)

(SS4) $\left(\frac{1-a_1}{1-a_1a_2}, \frac{1-a_2}{1-a_1a_2}\right)$. (partially-mutated coexistence)

The Jacobian matrix of equations (2.4) is given by

$$J = \begin{bmatrix} 1-2n^*-a_1p^* & -a_1n^* \\ -ba_2p^* & b-2bp^*-ba_2n^* \end{bmatrix}.$$

Substituting in the steady state values and evaluating the eigenvalues of J yields the following observations:

- The trivial steady state (SS1) $(0,0)$ is unstable, with positive eigenvalues $\lambda_1 = 1 > 0$ and $\lambda_2 = b > 0$.
- The healthy tissue steady state (SS2) $(1,0)$ has eigenvalues $\lambda_1 = -1$ and $\lambda_2 = b(1-a_2)$. For the latter to be negative, and hence for the healthy steady state to be stable, we require
$$a_2 > 1.$$
- For the fully-mutated tissue steady state (SS3) $(0,1)$ the eigenvalues are: $\lambda_1 = -b$ and $\lambda_2 = (1-a_1)$. Thus, the mutated tissue steady state is stable when $a_1 > 1$.

- For the partially-mutated tissue steady state (SS4) $\left(\frac{1-a_1}{1-a_1a_2}, \frac{1-a_2}{1-a_1a_2}\right)$, eigenvalues are given by

$$\lambda_{1,2} = [2(1-a_1a_2)]^{-1}[-[(1-a_1)+b(1-a_2)]\pm$$

$$\{[(1-a_1)+b(1-a_2)]^2 - 4b(1-a_1)(1-a_2)(1-a_1a_2)^2\}^{\frac{1}{2}}].$$

  The stability requires $\lambda_{1,2} < 0$, and this depends on the size of b, a_1 and a_2. Determining the stability of this last condition is clearly more intricate, although we note two special cases that yield some insight:

  - For $a_1 = 0$, we have $\lambda_1 = -1$ and $\lambda_2 = b(a_2 - 1)$. For the healthy-mutated tissue coexistance steady state to be stable we therefore need $a_2 < 1$.
  - For $a_2 = 0$, $\lambda_1 = -b$ and $\lambda_2 = (a_1 - 1)$. For the healthy-mutated tissue coexistence steady state to be stable we therefore need $a_1 < 1$.

The stability of (SS2) is of particular significance for the "in vivo" scenario: for initial conditions consisting of a small mutation that perturbs the healthy tissue steady state, only when $a_2 > 1$ do we expect a return to a completely healthy steady state tissue and for the mutated population to die out. On the other hand, for $a_2 < 1$ we have instability of the healthy tissue and can expect some form of growth of the mutant population: somewhat counter intuitively, this is regardless of parameters such as the mutant/healthy growth rate ratio b, i.e. a mutant population can still invade and infiltrate a healthy tissue even with a lower growth rate, due to its competitive advantage.

The progression of tumours proceeds through different phases, the first phase arising promptly after initiation and the survival of the mutation population depends just on the host (normal population) effect. In tumours generally the interaction between normal population and mutations is very complicated, because this interaction can lead to two different mechanisms: growth inhibition and stimulation. The inhibitors of growth include contact inhibition, programmed death (apoptosis) and immunological responses (although that is not considered a major factor for gliomas). Also, normal populations can stimulate the growth of mutated popula-

tions as a responce to signals from the mutated population [18]. We can express the effect of the normal population on the mutated population a_2 as:

$$a_2 = a_{2i} - a_{2s}$$

where a_{2i} represents the growth inhibitors and a_{2s} represents the growth stimulators. To examine a very early tumour, the normal population is placed at its carrying capacity $\frac{n}{k_1} \approx 1$ with the tumour very small, $\frac{p}{k_2} \approx 0$. Then (2.3) becomes

$$\begin{aligned} \frac{dn}{dt} &= 0; \\ \frac{dp}{dt} &= r_2 p \left(1 - a_2\right). \end{aligned} \tag{2.7}$$

The small mutation will grow if

$$\frac{dp}{dt} > 0 \Longrightarrow 1 - a_2 > 0,$$

or

$$a_{2s} > a_{2i} - 1.$$

Effectively, the small population of mutated cells increases in size if these transformed cells defeat the growth inhibitors produced from the healthy surrounding cells, such as contact inhibitors and terminal differentiation. Even if the proliferating rate of the tumour is less than that of the normal cells, the mutant cells can dominate if the competition rate is higher than 1 (see Figure 2.7).

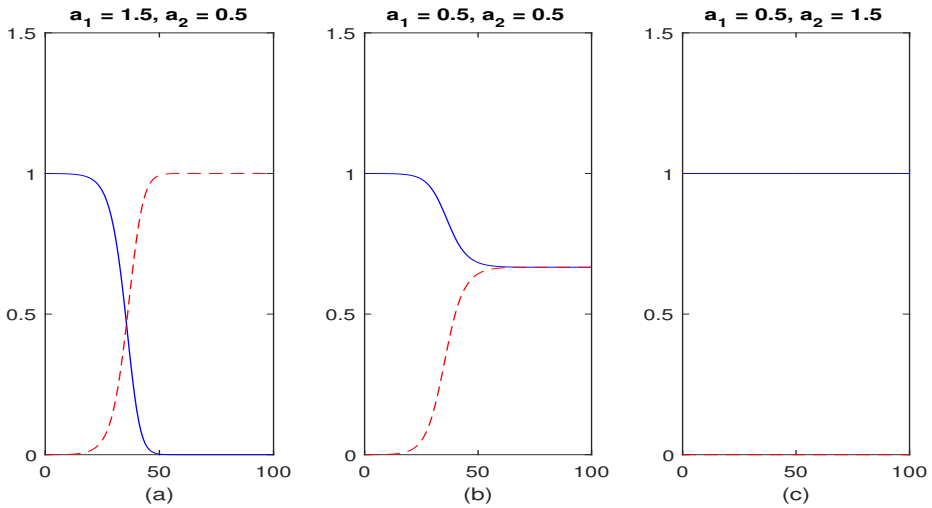

Figure 2.7: Simulations of model (2.4) with initial conditions (2.6), normal (blue solid) and mutant (red dashed) as function of time for proliferative rate ratio $b = 0.5$. (a) $a_1 = 1.5, a_2 = 0.5$. (b) $a_1 = 0.5, a_2 = 0.5$, (c) $a_1 = 0.5, a_2 = 1.5$. Numerics performed as in Figure 2.2.

2.3 Spatial modelling

2.3.1 Introduction to spatial modelling

The impact of spatial movement is an important consideration for many biological problems, from the movement of biological organisms to individual cells. In the context of modelling glioma growth, spatial invasion is clearly a point of significant concern: the rate and pattern of invasion is of key interest to clinicians wishing to determine the future spatio-temporal growth of the tumour and an appropriate treatment strategy.

Modelling spatial movement depends on the spatial and temporal scales of interest and must be considered carefully. For a large scale problem such as a growing brain tumour, where the tumour is of the order of centimetres and involves billions of cells, a sensible approach is to use continuum level modelling, such as partial differential equations, where the population is considered in terms of a continuous cell density equation. Such approaches benefit from the wide range of analytical tools

and methodologies, such as linear stability and travelling wave analysis, along with efficient numerical methodologies. Yet their disadvantages lie in their disconnection from the individual nature of cell movement: i.e. the manner in which an individual cell moves through its environment,

An alternative approach, therefore, is to propose a discrete or individual-based model, in which each cell is modelled as a separate entity. Such models are far more amenable to the individual-level data we usually have available and are very suitable for small scale problems, or those involving relatively few cells. Yet the fact that they allow for relatively little analysis demands heavy computation, which becomes increasingly problematic as the population size increases. Indeed, for the billions of cells involved in a large tumour, they become almost intractable.

A final approach is to start with a discrete/individual level model and then attempt to derive a continuous/macroscopic model via various scaling arguments. In the following section we extend our basic glioma model to incorporate spatial terms. We start with a brief review of spatial modelling techniques, first using classic continuum modelling techniques and then building continuous models from an underlying discrete random walk. We proceed to illustrate standard analyses: in particular, the analysis of travelling wave solutions which will be used in our studies here. Finally, we apply these methods to extend our basic model for glioma growth to account for cell movement.

2.3.2 Macroscopic model from the principle of conservation of matter

In the conservation approach, we define $c(x,t)$ to be the cell/organism density or chemical concentration at position $x \in \mathbf{R}^n$ and time t located within an arbitrary volume $V \subset \mathbf{R}^n$ enclosed by a surface $S \subset \mathbf{R}^{n-1}$, where n is the number of space dimensions. Then, the rate of change of c within V will be determined by the rate of creation/loss of c in V, along with the the flow of c across the surface S (see Figure 2.8). Note that we define dS to be the outer unit normal to S. Expressed in

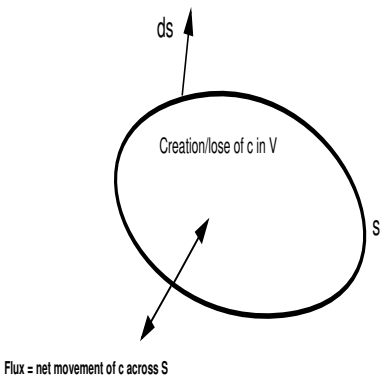

Figure 2.8: Illustration of conservation of matter. The change in the mass enclosed by the volume V will result from creation or loss in V and the transport/movement of matter across its surface S.

mathematical terms, this conservation law gives

$$\frac{\partial}{\partial t}\int_V c(x,t)\,dV = -\int_S J\cdot dS + \int_V f(\cdot)\,dV \tag{2.8}$$

where $J(x,t)\in\mathbf{R}^n$ is called the *flux*: it defines the local net movement of c. The function $f(.)$ describe the creation/loss of c: this could depend on space, time and the density of c itself, along with any other variables that are being modelled.

Applying the divergence theorem,

$$\int_S J\cdot dS = \int_V \nabla\cdot\mathbf{J}\,dV$$

in the above equation (2.8), we condense the integral terms into the single volume integral:

$$\int_V (\frac{\partial c}{\partial t} + \nabla\cdot\mathbf{J} - f(\cdot))\,dV = 0.$$

For an arbitrary V the integrand must be zero, and the conservation equation for c is

$$\frac{\partial c}{\partial t} + \nabla\cdot\mathbf{J} = f(\cdot). \tag{2.9}$$

The above holds for general fluxes and its choice varies with respect to movement processes. Diffusion is often considered in modelling: in the context of a cell population it would represent a (more or less) random movement. Movement is effectively assumed to be undirected and, at the population level, there is a net flux down

population density gradients. The classical choice of Fickian diffusion assumes

$$\mathbf{J} = -D\nabla c,$$

where D is the diffusion coefficient. As an example, adding the logistic population growth form $f(.) = rc(1-c/k)$ as earlier, and Fickian diffusion gives the well known Fisher equation:

$$\frac{\partial c}{\partial t} = D\nabla^2 c + rc(1 - c/k). \tag{2.10}$$

2.3.3 Macroscopic model from a biased random walk

The above conservation of mass based approach gives an example of phenomenological continuum-level modelling: the fluxes are chosen phenomenologically, and describe behaviour at a population-level. While such approaches have been widely exploited, a difficulty lies in of how to relate the macroscopic level parameters (such as the diffusion coefficients) in terms of behaviour and parameters at an individual level (for example, cell speeds).

Consequently, a significant amount of attention has focused on motivating continuous models from the starting point of some discrete/individual based process (see for examples [111, 85, 87, 7, 23]). Here we illustrate this by considering a discrete random walk: we assume each individual in our population moves as a "random walker" on a one-dimensional uniform lattice (a line split into discrete points, with adjacent points equally-spaced by distance Δx). We assume a walker jumps a distance Δx left or right with equal probability in each time step Δt, conditioned on being at position $x = 0$ at $t = 0$:

1. After one time step, the walker is at either $x = \pm\Delta x$ with probabilities 1/2.

2. After two time steps, the walker is at either $x = \pm 2\Delta x$ with probabilities 1/4, or will have returned to the origin with probabilities 1/2.

3. After some even (odd) number of time steps, the walker will be an even (odd) number of steps away from the origin. The maximum distance from the origin after j steps will be $j\Delta x$.

Overall, the probability $p_d(i,j)$ of a walker lies at distance i to the right or left of the origin after j time steps for even i, j and $i \leq j$ is given by the binomial distribution:

$$p_d(i,j) = \frac{1}{2^j}\binom{j}{(j-1)/2} = \frac{j!}{2^j((j+i)/2)!((j-i)/2)!},$$

with zero mean and variance $= j$. Defining the time $t = j\Delta t$ and position $x = i\Delta x$, then it is well known that as $j \longrightarrow \infty$ the binomial distribution converges to a normal distribution with zero mean and variance $= t(\Delta x)^2/\Delta t$:

$$p(x,t) = \frac{1}{\sqrt{4\pi Dt}} \exp(-\frac{x^2}{4Dt}), \tag{2.11}$$

where the diffusion coefficient $D = (\Delta x)^2/2\Delta t$. We note that the above equation is in fact the fundamental solution to the $1D$ diffusion equation. Notably, the diffusion coefficient D now relates to the step size and frequency of turns for a discrete random walk.

Macroscopic models from random walks

Next we explicitly derive the diffusion equation from an underlying discrete model. We define $p(x,t)$ as the time-dependent probability density function for the position of a random walker on the one-dimensional lattice above. We assume a walker jumps either one site to the left $(-)$ or to the right $(+)$ according to some probability in each time step Δt: we use the notation $\tau_x^{\pm}$ to define the probability that a walker at position x moves to position $x \pm \Delta x$, see Figure 2.9. Based on this description, we can write down a discrete-time, discrete-space master equation for the evolution of $p(x,t)$ as follows:

$$p(x, t+\Delta t) = \tau^+_{x-\Delta x} p(x-\Delta x, t) + \tau^-_{x+\Delta x} p(x+\Delta x, t) + (1 - \tau^+_x - \tau^-_x) p(x,t). \tag{2.12}$$

Note that we must have $0 \leq \tau_x^+, \tau_x^- \leq 1$ and $0 \leq \tau_x^+ + \tau_x^- \leq 1$.

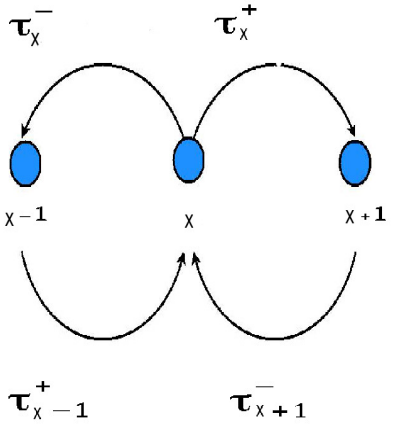

Figure 2.9: Illustration of a random walk on a discrete lattice. In each time step a walker at x can jump to the left or right according to transitional probabilities $\tau_x^{\pm}$, or stay at its current position with probability $1 - \tau_x^+ - \tau_x^-$. Similarly a walker at $x \pm \Delta x$ can jump to x according to transitional probabilities $\tau_{x\pm\Delta x}^{\mp}$

Unbiased random walk

In an unbiased random walk we assume the probabilities of moving left/right are equal and set $\tau^{\pm} = \alpha$ (constant) throughout space x. Consequently, we obtain

$$p(x, t + \Delta t) = \alpha(p(x - \Delta x, t) + p(x + \Delta x, t) - 2p(x, t)) + p(x, t).$$

Expanding via Taylor series, we generate:

$$p(x, t + \Delta t) = p(x, t) + \Delta t \frac{\partial p}{\partial t}(x, t) + O((\Delta t)^2);$$

and

$$p(x \pm \Delta x, t) = p(x, t) \pm \Delta x \frac{\partial p}{\partial t}(x, t) + \frac{(\Delta x)^2}{2} \frac{\partial^2 p}{\partial x^2}(x, t) + O((\Delta x)^3).$$

Substituting these expansions into equation (2.12) we have

$$p(x, t) + \Delta t \frac{\partial p}{\partial t}(x, t) + O((\Delta t)^2) = \alpha(\Delta x)^2 \frac{\partial^2 p}{\partial x^2}(x, t) + p(x, t) + O((\Delta t)^3).$$

Noting that the $p(x, t)$'s cancel, we consider the diffusion limit. Specifically, we

assume Δt, $\Delta x \to 0$ such that

$$\lim_{\Delta t, \Delta x \to 0} \frac{\alpha(\Delta x)^2}{\Delta t} = D,$$

for some constant parameter D. Applied to the above, we derive the 1D diffusion equation with constant diffusion coefficient D:

$$\frac{\partial p(x,t)}{\partial t} = D \frac{\partial^2 p}{\partial x^2}(x,t). \tag{2.13}$$

Biased random walks

This approach can be adapted to include additional assumptions. For example, let us assume there is a bias in the directional choice by setting $\tau^+(x) = \alpha + \varepsilon/2$ and $\tau^-(x) = \alpha - \varepsilon/2$. Again we substitute into equation (2.12) to obtain:

$$\begin{aligned} p(x, t+\Delta t) = \alpha(p(x-\Delta x, t) + p(x+\Delta x, t) - 2p(x,t)) + p(x,t)) \\ + \frac{\varepsilon}{2}(p(x-\Delta x, t) - p(x+\Delta x, t)) - p(x,t). \end{aligned} \tag{2.14}$$

After expanding as before via Taylor expansion and considering limits as Δt, $\Delta x \to 0$ such that:

$$\lim_{\Delta t, \Delta x \to 0} \frac{\alpha(\Delta x)^2}{\Delta t} = D,$$

and

$$\lim_{\Delta t, \Delta x \to 0} \varepsilon \frac{\Delta x}{\Delta t} = a.$$

This yield the 1D diffusion-advection equation with diffusion coefficient D and drift velocity a:

$$\frac{\partial p(x,t)}{\partial t} = D \frac{\partial^2 p}{\partial x^2}(x,t) - a \frac{\partial p}{\partial x}(x,t). \tag{2.15}$$

2.4 Spatial extension of the basic model for glioma growth

Gliomas have proven to be highly difficult to treat, with many experimental and theoretical works attempting to understand the difficulty of their treatment. One cause of their resistance to treatment stems from their highly invasive nature, with significant infiltration into the surrounding tissue from the main tumour mass: experimental studies [106] have shown that within a week of tumour implantation into a rat brain, not only a dense mass of glioma cells can be seen located to the initiated area, but solitary glioma cells are observed deep across the central nervous system (CNS). This implies a reason for treatment failure: glioma treatment focuses on the dense mass of glioma, while invasion and glioma growth is more diffuse. Subsequently, distant cells that have moved far away from the focus of treatment may subsequently result in regrowth.

Mathematical modelling can play an important role in understanding and analysing the growth dynamics of glioma. Amongst the first modelling attempts were by Tracqui et al. [120], Woodward et al. [127] and Burgess et al. [14]. These models captured two main feature of the tumour, proliferation and diffusion, and showed that diffusion is more important than proliferation in determining the survival rate. A further complicating aspect to this diffusive type spread of gliomas lies in the heterogeneity of the brain tumour: in particular, invasion is believed to be higher in the white matter than the grey matter. In vivo studies [106] suggest that malignant glioma cells predominantly invade the brain tissue via the long, directional white matter tracts leading to rapid invasion along specific pathways.

The basic spatio-temporal equation developed in Murray's group simplified glioma growth into an uncontrolled proliferation of tumour cells coupled to an ability to invade the surrounding tissue. In word form:

$$\begin{matrix}\textbf{Rate of change} \\ \textbf{of glioma cells}\end{matrix} = \begin{matrix}\textbf{Net diffusion} \\ \textbf{of glioma cells}\end{matrix} + \begin{matrix}\textbf{Net proliferation} \\ \textbf{of glioma cells}\end{matrix}.$$

Letting $n(x,t)$ be the density of glioma cells at position x and time t, a partial differential equation based on a simple reaction-diffusion equation with Fickian diffusion and exponential growth takes the form:

$$\frac{\partial n}{\partial t} = \nabla \cdot (D \nabla n) + \rho n.$$

In the above, D (distance^2/time) is the diffusion coefficient of cells in brain tissue and ρ (time^{-1}) represents the net rate of growth of cells. Subsequent modelling has extended these basic models to investigate a wide range of aspects, such as the heterogeneous structure of the brain [115, 128, 58, 86], different forms of treatment [120, 28, 61, 96, 114] and the phenotypic switching of cells according to the go-or-grow hypothesis. In this section we extended to consider a mathematical model for the spatio temporal dynamics of tumour growth within the normal healthy tissue.

2.4.1 Spatial competition model

We let $n(x,t)$ be the density of glial healthy cells at a position x and time t and $p(x,t)$ be the density of glioma cells at a position x and time t. For the current purposes we restrict to a single space dimension, assuming $x \in [0, L]$. We consider a reaction-diffusion equation with Fickian diffusion and logistic growth as follows

$$\begin{aligned} \frac{dn}{dt} &= D_1 \frac{\partial^2 n}{\partial x^2} + r_1 n \left(1 - \frac{n}{k_1} - a_1 \frac{p}{k_2}\right); \\ \frac{dp}{dt} &= D_2 \frac{\partial^2 p}{\partial x^2} + r_2 p \left(1 - \frac{p}{k_2} - a_2 \frac{n}{k_1}\right). \end{aligned} \tag{2.16}$$

In the above model, D_1 and D_2 are the diffusion coefficients of healthy and mutant cells respectively, while parameters for the competition-type kinetic terms are as previously defined in Section (2.2.1). As previously, we will be mainly focussed on the role of the ratios between critical parameters. In addition to our earlier discussions

on growth rates, carrying capacities *etc.* we note that the above equations include diffusion coefficients D_1 and D_2 to describe random movement of normal and mutant glial cells. The former is assumed to be relatively small (although not necessarily zero): we do not expect healthy glial cells to undergo significant movement, with their primary role being in support of the neural architecture and possibly only stimulated to move following tissue disruption. Mutant cells, however, are expected to have a greater invasive capacity: we note moreover that studies suggest that the diffusion coefficient for glioma cells in the white matter is five times larger than that in grey matter [19, 115]. We take the standard assumption of zero flux boundary conditions, setting

$$n_x(0,t) = n_x(L,t) = p_x(0,t) = p_x(L,t) = 0\,.$$

For initial conditions we assume $n(x,0) = n_0(x)$ and $p(x,0) = p_0(x)$, where $n_0(x)$ and $p_0(x)$ are nonnegative functions: these are defined below for two investigated scenarios.

2.4.2 Numerical simulations

As before, we first perform a non-dimensionalisation by setting

$$D = \frac{D_1}{D_2}, \qquad \text{and rescale} \quad x^* = x(\frac{r_1}{D_2})^{\frac{1}{2}}$$

along with the previous scalings:

$$n^* = \frac{n}{k_1}; \qquad p^* = \frac{p}{k_2}; \qquad t^* = r_1 t; \qquad b = \frac{r_2}{r_1}\,.$$

Substituting these into equations (2.16), we obtain the dimensionless model as follows:

$$\begin{aligned} \frac{\partial n}{\partial t} &= D\frac{\partial^2 n}{\partial x^2} + n\,(1 - n - a_1 p)\,; \\ \frac{\partial p}{\partial t} &= \frac{\partial^2 p}{\partial x^2} + bp\,(1 - p - a_2 n)\,. \end{aligned} \tag{2.17}$$

Note that following the considerations above, healthy cells are expected to diffuse less freely than mutant cells and hence $0 \leq D \leq 1$. The above system has the same four uniform steady state solutions described in Section (2.2.4). Our earlier analysis focused on two scenarios: a simulated "in vivo" case, where we considered the growth (or otherwise) of a small population of mutated cells within a healthy tissue environment, and an "in vitro" case, where the growth (or otherwise) of co-cultured mutant and healthy cells was considered within some *in vitro* set-up. To model these we consider the following initial conditions:

$$\text{(In vivo) } n_0(x) = \begin{cases} 1-\epsilon & \text{if } x \leq \delta \\ 1 & \text{otherwise} \end{cases}; \qquad p_0(x) = \begin{cases} \epsilon & \text{if } x \leq \delta \\ 0 & \text{otherwise} \end{cases}. \tag{2.18}$$

$$\text{(In vitro) } n_0(x) = \begin{cases} \epsilon & \text{if } x \leq \delta \\ 0 & \text{otherwise} \end{cases}; \qquad p_0(x) = \begin{cases} \epsilon & \text{if } x \leq \delta \\ 0 & \text{otherwise} \end{cases}. \tag{2.19}$$

2.4.2.1 In vivo scenario

In Figure 2.10 we plot the dynamics of mutant and normal cells on a domain of length 200 at successive times. We fix $D = a_2 = 0.5$ and vary $a_1 = 0.25$, 0.5 & 0.75, and $b = 0.5$, 1.0 & 2.0. Moving down through the rows we observe a faster rate of invasion/infiltration as the growth rate ratio increases. Although we note that the mutant population will still infiltrate and take over even when $b < 1$ (i.e tumour cells are less proliferative than normal cells). Moving right through the columns we observe an increase in the amount of mutant cells as the competition rate a_1 increases. A faster rate of invasion of mutant cells occurs when their proliferative rate is much greater than the proliferative rate of normal cells. On the other hand we do not notice any difference as we vary D (see Figure 2.11). In Figure 2.12 we investigate whether the competition rates a_1 and a_2 have any impact on the invasion of mutant cells. We fix the diffusion parameter $D = 1$ and vary the proliferative rate $b = 0.5$, 1.0 & 2. To measure the invasion of mutant population we keep track of the invasive front of mutant cells over time. For example, based on the initial density of mutant cells, we measure the depth reached at specific times: mathematically,

we define the invasive depth x^* at time t^* as the largest x^* for which $p(x^*, t^*) \leq \varepsilon$, where $t^* \in (0, T)$, and ε is the initial amount of mutant cells, equal to 0.0001. We plot the invasion depth at the final time of simulation $T = 100$. We find that the competition rate of mutant cells on normal cells a_1 has no impact on the invasion of the mutant population. Increasing the competition rate of normal cells on mutant cells a_2 can decrease the invasion of mutant population. Moving right through the columns we observe an increase in the invasion of mutant population as the growth rate difference b increase while, on the other hand, no change in the invasion depth occurs when D is altered (see Figure 2.13).

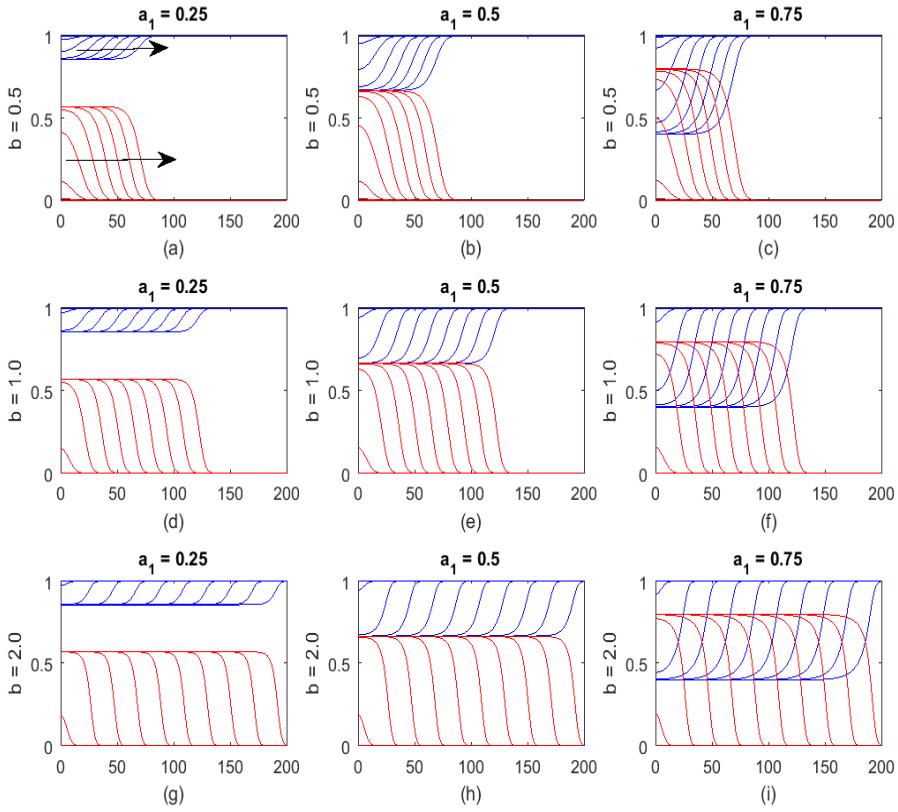

Figure 2.10: Simulations of model (2.17) with initial conditions (2.18) for different values of b, a_1 and fixed $D = a_2 = 0.5$. We plot normal (blue) and mutant (red) populations as functions of time and space. (a) $b = 0.5, a_1 = 0.25$. (b) $b = 0.5, a_1 = 0.5$. (c) $b = 0.5, a_1 = 0.75$. (d) $b = 1.0, a_1 = 0.25$. (e) $b = 1.0, a_1 = 0.5$. (f) $b = 1.0, a_1 = 0.75$.(g) $b = 2.0, a_1 = 0.25$. (h) $b = 2.0, a_1 = 0.5$. (i) $b = 2.0, a_1 = 0.75$. The equations were solved numerically in time interval $0 \leq t \leq 100$, using "pdepe" solver in Matlab, with a relative tolerance $= 10^{-9}$, absolute tolerance $= 10^{-12}$ and grid spacing of 0.5. We solved on the spatial domain $0 \leq x \leq 200$, with zero flux conditions ($n_x = m_x = 0$) at both boundaries.

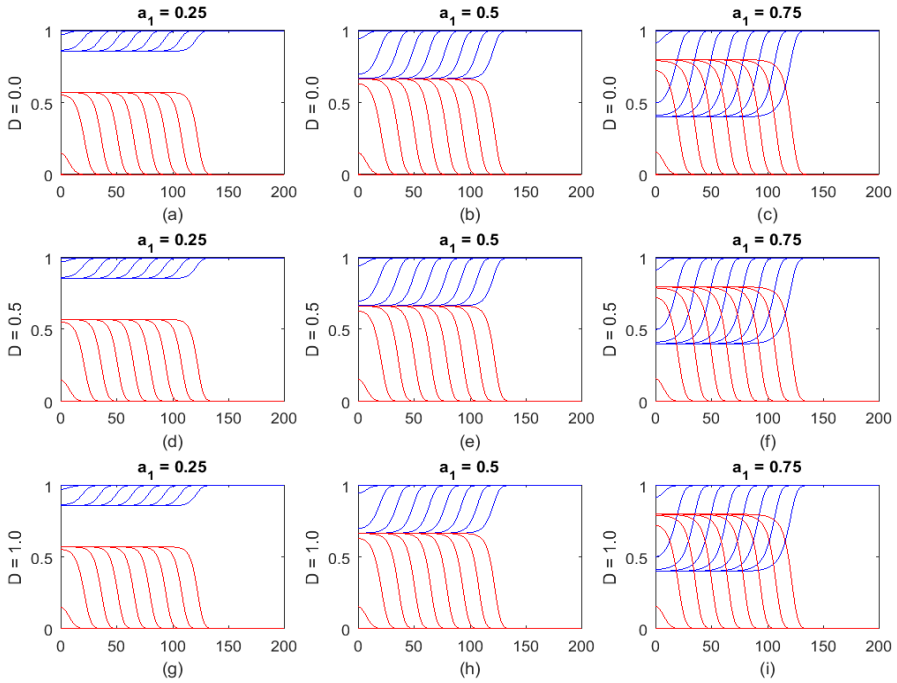

Figure 2.11: Simulations of model (2.17) with initial conditions (2.18) for different values of D, a_1 and fixed $a_2 = 0.5$ and $b = 1.0$. We plot normal (blue) and mutant (red) populations as functions of time and space. (a) $D = 0.0, a_1 = 0.25$. (b) $D = 0.0, a_1 = 0.5$. (c) $D = 0.0, a_1 = 0.75$. (d) $D = 0.5, a_1 = 0.25$. (e) $D = 0.5, a_1 = 0.5$. (f) $D = 0.5, a_1 = 0.75$.(g) $D = 1.0, a_1 = 0.25$. (h) $D = 1.0, a_1 = 0.5$. (i) $D = 1.0, a_1 = 0.75$. The numerical method was as in Figure 2.10.

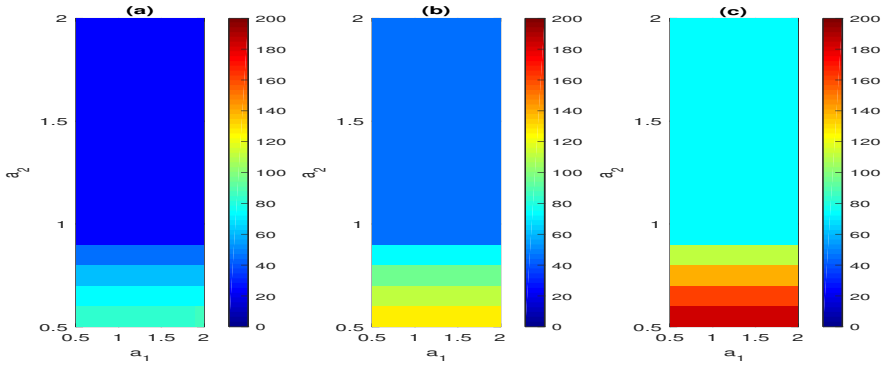

Figure 2.12: Plot of invasion depth at time $t = 100$ for a_1 vs a_2. With fixed $D = 1$ and: (a) $b = 0.5$; (b) $b = 1$; (c) $b = 2$. The numerical method was as in Figure 2.10.

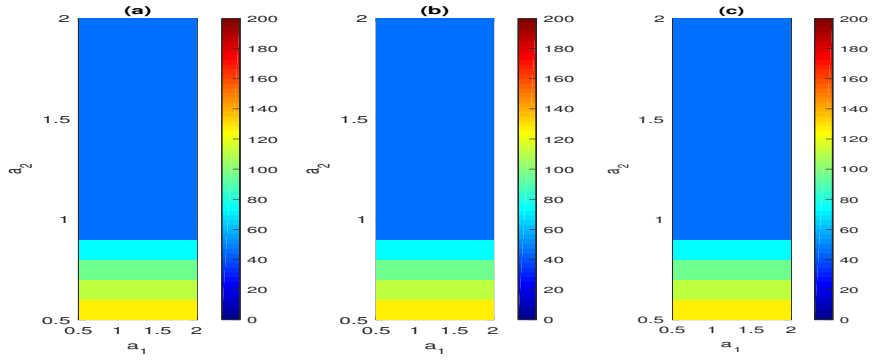

Figure 2.13: Plot of invasion depth at time $t = 100$ for a_1 vs a_2. With fixed $b = 1$ and (a) $D = 0.0$, (b) $D = 0.5$, (c) $D = 1$. The numerical method was as in Figure 2.10.

2.4.3 Travelling wave analysis of extended model

The numerical simulations above indicate travelling-wave type solutions to our model, and we perform a travelling wave analysis to obtain insight into invasion speeds. We note that in Appendix A.3 we provide a brief review of travelling wave analysis for the simple Fisher equation (2.10): the analysis here follows the same principles. To start with, we make the standard travelling wave ansatz and look for solutions of the form:

$$n(x,t) = N(z), \quad p(x,t) = P(z), \quad z = x - ct,$$

where z define the travelling wave coordinate. If solutions of above form exist, they represent travelling waves that move to the right in the $z-$plane with wavespeed c. Substitution into equations (2.17) gives a system of second order ordinary differential equations as follows:

$$\begin{aligned} DN'' + cN' + N(1 - N - a_1 P) &= 0; \\ P'' + cP' + bP(1 - P - a_2 N) &= 0. \end{aligned} \tag{2.20}$$

Where the "prime" denotes differentiation with respect to z. An analysis of the above equation would require the study of a four-dimensional phase space, however

we shall consider a simpler case where the diffusion coefficient, D_1, of the normal cell population is considerably smaller than that of cancer cells, D_2. Consequently, we assume $D(=\frac{D_1}{D_2}) \approx 0$ in our nondimensional equations, introduce $W = P'$ and obtain a three variable system of first order ordinary equations as follows:

$$\begin{aligned} N' &= -\frac{1}{c}[N(1 - N - a_1 P)]; \\ P' &= W; \\ W' &= -cW - bP(1 - P - a_2 N). \end{aligned} \tag{2.21}$$

This system possesses four steady states:

- $(0, 0, 0)$ (trivial - no cells);
- $(1, 0, 0)$ (healthy tissue);
- $(0, 1, 0)$ (fully mutated tissue);
- $(\frac{1-a_1}{1-a_1a_2}, \frac{1-a_2}{1-a_1a_2}, 0)$ (partially-mutated coexistence).

2.4.3.1 In vivo scenario

For the in vivo scenario we can identify two relevant forms for travelling wave solution: from the Figures 2.14, there are various possibilities of travelling wave front solution:

1. a wave connecting the healthy steady state $(1, 0, 0)$ and the fully-mutated steady state $(0, 1, 0)$;
2. a wave connecting the healthy steady state $(1, 0, 0)$ to the partially-mutated steady state $(\frac{1-a_1}{1-a_1a_2}, \frac{1-a_2}{1-a_1a_2}, 0)$.

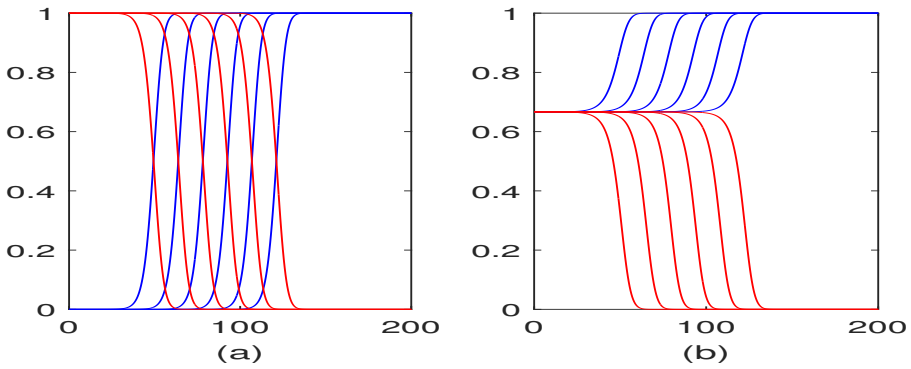

Figure 2.14: Simulations of model (2.17) with initial conditions (2.18). We plot normal (blue) and mutant (red) as functions of time and space with fixed $D = 0.0$ and $b = 1$. (a) connecting the healthy steady state $(1, 0, 0)$ and the fully-mutated steady state $(0, 1, 0)$, where $a_1 = 1.5$ and $a_2 = 0.5$. (b) connecting the healthy steady state $(1, 0, 0)$ to the partially-mutated steady state $(\frac{1-a_1}{1-a_1a_2}, \frac{1-a_2}{1-a_1a_2}, 0)$, where $a_1 = 0.5$ and $a_2 = 0.5$. The numerical method was as in Figure 2.10.

We start by considering travelling wave solutions connecting $(1, 0, 0)$ and $(0, 1, 0)$, assuming the infinite line with boundary conditions:

$$N(-\infty) = 0, \quad P(-\infty) = 1, \quad W(-\infty) = 0 \quad N(\infty) = 1, \quad P(\infty) = 0, \quad W(\infty) = 0.$$

By analogy with the analysis of travelling wave equations for Fisher's equation, we linearise system (2.21) ahead of the wavefront (i.e. about the steady state of healthy cells $(1, 0, 0)$) and determine the nature of the eigenvalues λ of the subsequent stability matrix, i.e. the solutions of

$$\begin{vmatrix} \frac{1}{c} - \lambda & \frac{a_1}{c} & 0 \\ 0 & -\lambda & 1 \\ 0 & -b(1-a_2) & -c-\lambda \end{vmatrix} = 0\,.$$

Hence,

$$\lambda_1 = \frac{1}{c};$$
$$\lambda_2 = \frac{1}{2}\{-c + \sqrt[2]{c^2 - 4b(1-a_2)}\};$$
$$\lambda_3 = \frac{1}{2}\{-c - \sqrt[2]{c^2 - 4b(1-a_2)}\}.$$

For the travelling wave solutions to remain non-negative, we require the eigenvalues to be real and hence

$$c \geq 2\sqrt{b(1-a_2)}\,.$$

Note that in the case $D \neq 0$, similar analysis generates four eigenvalues

$$\lambda_{1,2} = \frac{1}{2}\{-c \pm \sqrt[2]{c^2 - 4b(1-a_2)}\}, \qquad \lambda_{3,4} = \frac{1}{2D}\{-c \pm \sqrt[2]{c^2 + 4D)}\}$$

Again, for the above eigenvalues to remain real, we also require

$$c \geq 2\sqrt{b(1-a_2)}\,.$$

Under compact initial conditions we assume travelling waves move at this minimum speed, in line with the simpler Fisher equation. This confirms our earlier finding that there is no dependence on D or a_1. We have plotted in Figure 2.15 the analytical and numerical minimum wave speed of the tumour for different values of parameters a_1, a_2, D and b. Note that the minimum speed accurately tracks the numerically calculated value. When the competition of normal healthy cells increase the speed of the wavefront of tumor decreases to zero. Whereas the wave speed of tumour increases with increasing growth rate of tumour.

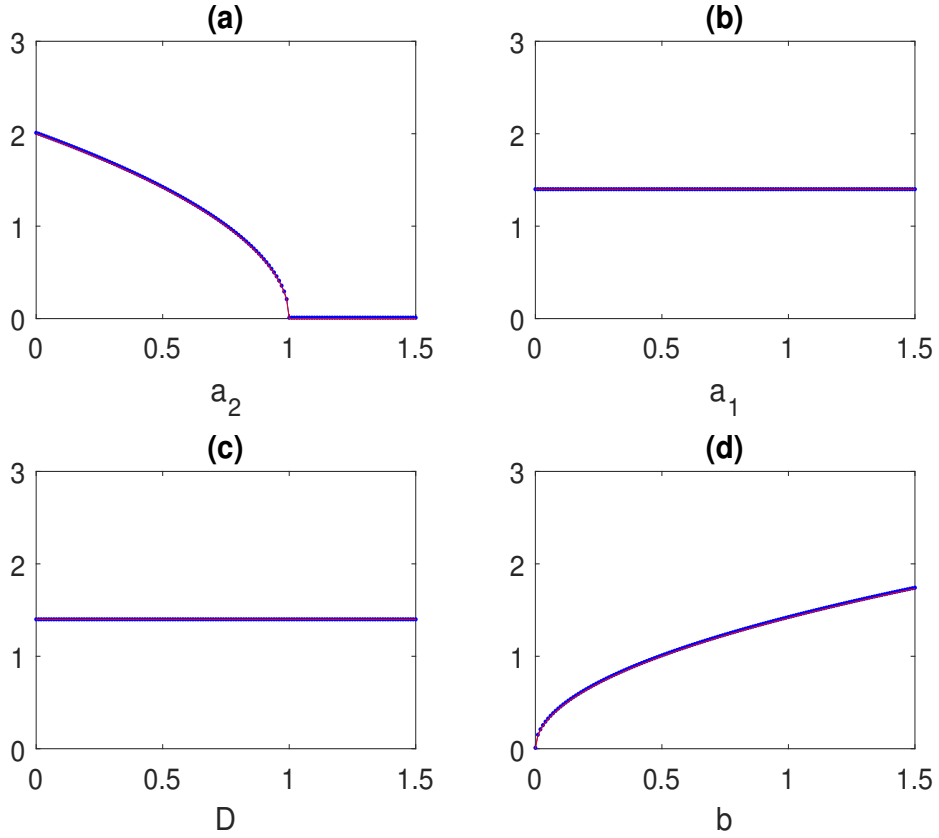

Figure 2.15: The analytical (red) and simulated (blue) wave speed for different values of model parameters. The numerical method was as in Figure 2.10.

However, it is remarked that these analyses were for a nondimensional form of the model, and it is perhaps more illustrative to consider the original dimensional form, i.e Equations 2.16a - 2.16b. In this case we find that

$$c \geq 2\sqrt{r_2(1-a_2)D_2}. \tag{2.22}$$

Therefore, the wave speed depends on the diffusion of mutant cells, but not healthy cells.

Overall, this suggests that invasion is facilitated by

1. fast growing mutant cells;

2. low competition a_2;

3. fast random movement of mutant cells.

2.4.3.2 In vitro scenario

For the in vitro scenario we can identify two relevant forms for travelling wave solution: As demonstrated in Figure 2.16, there are different possibilities to demonstrate travelling wave front solution:

1. a wave connecting the fully-mutated steady state $(0, 1, 0)$ and the trivial steady state $(0, 0, 0)$;

2. a wave connecting the partially-mutated steady state $(\frac{1-a_1}{1-a_1a_2}, \frac{1-a_2}{1-a_1a_2}, 0)$ and the trivial steady state $(0, 0, 0)$.

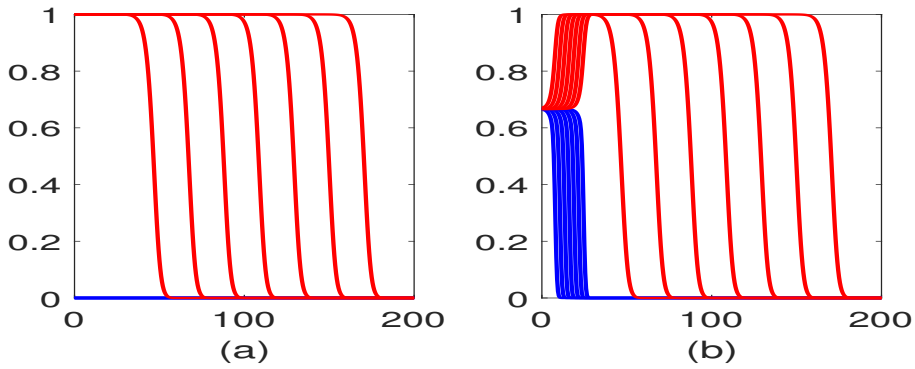

Figure 2.16: Simulations of model (2.17) with initial conditions (2.19). We plot normal (blue) and mutant (red) populations as functions of time and space with fixed $D = 0.0$ and $b = 1$. (a) connecting the healthy steady state $(0, 1, 0)$ and the trivial steady state $(0, 0, 0)$, where $a_1 = 1.5$ and $a_2 = 0.5$. (b) connecting the partially-mutated steady state $(\frac{1-a_1}{1-a_1a_2}, \frac{1-a_2}{1-a_1a_2}, 0)$, to the trivial steady state $(0, 0, 0)$ where $a_1 = 0.5$ and $a_2 = 0.5$. The numerical method was as in Figure 2.10.

We start by considering travelling wave solutions connecting $(0, 1, 0)$ and $(0, 0, 0)$, assuming the infinite line with boundary conditions:

$$N(-\infty) = 0, \quad P(-\infty) = 1, \quad W(-\infty) = 0 \quad N(\infty) = 0, \quad P(\infty) = 0, \quad W(\infty) = 0.$$

By analogy with the analysis of travelling wave equations for Fisher's equation, we linearise the system (2.21) ahead of the wavefront (i.e. about the steady state of

healthy cells $(0,0,0)$) and determine the nature of the eigenvalues λ of the subsequent stability matrix, i.e. the solutions of

$$\begin{vmatrix} \frac{-1}{c} - \lambda & 0 & 0 \\ 0 & -\lambda & 1 \\ 0 & -b & -c-\lambda \end{vmatrix} = 0\,.$$

Hence,

$$\begin{aligned} \lambda_1 &= \frac{-1}{c}; \\ \lambda_2 &= \frac{1}{2}\{-c + \sqrt[2]{c^2 - 4b}\}; \\ \lambda_3 &= \frac{1}{2}\{-c - \sqrt[2]{c^2 - 4b}\}. \end{aligned}$$

For the solutions to remain non-negative, we require the above eigenvalues to be real and hence

$$c \geq 2\sqrt{b}\,.$$

In terms of the original dimensional equation (2.16), the range of wave speeds satisfies

$$c \geq 2\sqrt{r_2 D_2}. \tag{2.23}$$

We note that in the in vitro case the wave-speed does not depend on the competition parameters. In other words, certain in vitro settings will not give the full picture or the speed at which invasion takes place.

2.5 Summary

We have reviewed some basic mathematical analysis and applied it to a simple competition model of healthy tumour cells. We have studied the competition of healthy-mutant cells under ODE and PDE forms, for in vivo and in vitro scenarios. For the in vivo case increasing the competitive parameter of glioma cells on normal cells leads to an increase in the number of glioma cells compared to normal cells. Increasing the growth ratio leads to a decrease in the time required for glioma to

dominate. For the in vitro case, when the growth rate of glioma cells is low, the number of glioma cells compared to normal cells is low in early stages of glioma development. While at later times of glioma progression, the number of glioma cells is reduced compared to the normal cells.

The stability analysis showed that the normal cells can recover if the competition rate of normal cells on glioma cells satisfies $a_2 > 1$. For the in vivo case of the spatial competition model, invasion of glioma increases as the growth ratio b increases. However, the competitive rate of glioma cells has no impact on the invasion, yet it does increase the number of glioma cells. Travelling wave analysis of the in vivo scenario showed that the minimum wave speed of glioma cells depends on the competitive parameter of normal cells and the diffusion parameter and the growth rate of glioma cells. On the other hand, a similar analysis for the in vitro case showed that the minimum wave speed of glioma cells depends on the growth rate and the diffusion parameter of glioma cells.

In this Chapter we have reviewed the study of Gatenby [36, 34]. The study has been extended to investigate many further biological behaviors, for instance [37, 38, 39]. We here only studied the dynamic of healthy-mutated competition in spatial-temporal form. Nevertheless, the mutant cells of glial cells are more sophisticated cells. Research by Giese et al. [44, 42] suggests that gliomas can be subdivided into proliferating cells and migrating cells. Proliferating cells rarely migrate, while migrating cells rarely proliferate. The switch between these two phases, i.e a moving phase and growing phase, is known as the "go or grow" hypothesis. In the next Chapter we will discuss the mechanism of go or grow gliomas under competition from healthy cells.

Chapter 3

Go-or-Grow glioma mathematical model

In this chapter we propose a simple mathematical model based on the go or grow hypothesis for brain tumours (gliomas). The model describes the competition between healthy glial cells and malignant cells, with the latter subdivided into invasive and proliferating subpopulations. We begin with a brief review of the go-or-grow hypothesis, and summarise the various modelling efforts that have attempted to understand this phenomenon. We subsequently build on a model developed by Pham and others [91] to incorporate an additional "healthy" population, which is assumed to compete with the mutant subpopulations. Our investigations suggest that increasing the probability of entering a migratory state may delay the rate at which a tumour overcomes the normal cells. In addition, the wave speed of the tumour increases as the probability of migratory cells increase until the probabilities of migratory state is equal to stationary state, then the wave speed starts to decrease.

3.1 Introduction and previous modelling

As we have previously described, gliomas form an invasive and heterogeneous class of primary brain tumour. Malignant gliomas are often lethal, evading therapeutic strategies such as excision, chemotherapy and radiation therapy in part due to their capacity to invade the surrounding brain. A leading hypothesis by Giese et al. [44, 42] suggests that malignant cells switch between proliferating and migrating phenotypes, a mechanism known as the "go or grow" hypothesis (see Figure 3.1). Although the molecular mechanisms that control this switching are uncertain, it is generally assumed to depend on microenvironmental factors: e.g. hypoxia, low glucose, extracellular matrix components, cellular densities etc can potentially lead to this dichotomy [44]

Treatment of malignant brain tumours is therefore complicated not only due to their critical location, but also by the difficulty of eliminating the malignant cells that enter a migratory phenotype. These cells have the capacity to infiltrate and invade the brain along myelinated fiber tracts in the white matter [43], allowing them to move far beyond the tumour core. Simple excision of the tumour will generally fail to eliminate all of these invading cells and, while subsequent chemotherapy and/or radiotherapy can be applied to reduce their number, it is believed that migratory cells are less sensitive to therapy than those in the proliferative phase [72]. Consequently, malignant tumours are generally found to recur following the original treatment phase.

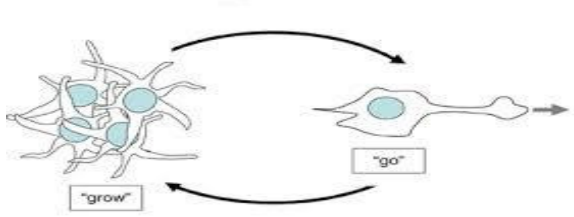

Figure 3.1: Illustration of go-or-grow hypothesis.

A number of mathematical models have been developed to study this dichotomy between proliferation and migration, both at cellular and molecular levels, e.g. see

[63]. For example, [31] used stochastic/probabilistic models to investigate the migration/proliferation switching phenotype. Gliomas cells are believed to switch between proliferative and invasive phenotypes according to the oxygen concentrations in their local environment: in vitro motility assays indicate accelerated invasion in low ambient oxygen. Hatzikirou et al explored such properties, focussing their work on a particularly aggressive and invasive tumour, glioblastoma multiforme (GBM), and developed a lattice-gas cellular automaton. A lattice-gas cellular automaton model was developed to investigate how different cell migration strategies depend on cell density, considering whether cell motility increases with local cell density or decreases with local cell density [52, 117].

Investigation of the go-or-grow mechanism on avascular glioma invasion shows that knowledge of the individual cell phenotype is not enough to extrapolate the macroscopic tumour colony [12]. Saut et al. also proposed a mathematical model that takes into account the ability of proliferative cells to become invasive under hypoxic conditions. The effects of the go-or-grow mechanism on glioma invasion and anti-angiogenesis growth showed that accelerated growth can lead to a lack of long-term efficacy of anti-angiogenesis drugs in the treatment.

Mathematically, Zhigun et al. proved the global existence of weak solutions of cancer model under the go-or-grow hypothesis [130]. Gerlee et al. proposed a stochastic reaction-diffusion equation for the go-or-grow phenotype, which was shown to exhibit travelling wave type solutions.

In the context of the present chapter, Pham et al. [91] presented a mathematical model (see (3.1)) of the go-or-grow hypothesis, based on a coupled system of ordinary and partial differential equations for migratory and proliferative phenotypes. In this model, phenotypic switching was assumed to be dependent on the cell density, and the model was shown to generate complex dynamics similar to that associated with tumour heterogeneity and invasion. The model considered a migrating population $\rho_1(x,t)$ that does not proliferate and a proliferating population $\rho_2(x,t)$ that does not move, and hence total population density $\rho(x,t) = \rho_1 + \rho_2$. Under simple assumptions of linear diffusion for movement and logistic growth for proliferation,

the main focus of the model was the exchange between the two sub-populations:

$$\begin{aligned} \frac{\partial \rho_1}{\partial t} &= D\triangle m + \mu[\Gamma(\rho)\rho_2 - (1-\Gamma(\rho))\rho_1]; \\ \frac{\partial \rho_2}{\partial t} &= -\mu[\Gamma(\rho)\rho_2 - (1-\Gamma(\rho))\rho_1] + r\rho_2(1-\rho/\rho_m)). \end{aligned} \tag{3.1}$$

In the above, D is the diffusion coefficient of migrating cells, μ is the rate at which cells change their phenotype, $\Gamma(\rho)$ is the probability that a proliferating cell becomes migrating, r is the proliferating rate and ρ_m is the carrying capacity of the cells. Pham et al.[91] consider two complementary mechanisms for the phenotypic switch, modelled by the sigmoidal functions:

$$(M_1) \quad \Gamma(\rho) = \frac{1}{2}(1 + \tanh(\alpha[\rho^* - \rho])); $$

and

$$(M_2) \quad \Gamma(\rho) = \frac{1}{2}(1 - \tanh(\alpha[\rho^* - \rho])).$$

Under mechanism M_1 the cells become more migratory at low local cell densities, and less migratory when the density is high, and conversely under M_2. The parameter α describes the sharpness in the switch phenotype, and ρ^* is the density threshold at which the probabilities of being proliferating or migrating are equal. The model dynamics were shown to have the potential to generate spatial patterns under mechanism M_1, leading to irregular oscillatory dynamics. The model also indicated that glioma tumours can grow fast, but homogeneously, or slow and heterogeneously.

While the above model provides a useful basis for incorporating the go-or-grow hypothesis into simple continuous-level models for glioma growth, inevitably a number of potentially important factors are omitted. For example, the model ignores the growth of the tumour within the normal brain environment, and the potential impact from competition between the healthy cells and the malignant sub-populations. Second, augmenting the model with treatment may provide insights into how certain tumours may prove more or less amenable to treatment. Third, the model does not explicitly incorporate hypotheses for the molecular basis for switching or the potential complexity due to the heterogeneous structure of the brain.

3.2 Extension to include healthy-mutated competition

We build on the above model of Pham et al. [91] by including a normal/healthy population that competes with the mutant subpopulations. Specifically, we let $n(x,t)$ define the normal/healthy population and define two mutant subtypes: $p(x,t)$ the proliferating sub-population and $m(x,t)$ the migrating sub-population; we let $s(x,t) = n(x,t) + p(x,t) + m(x,t)$ represent the sum of all populations. Here, $x \in \Omega$ defines the position and t is time. Generally, Ω would define the spatial extent of the central nervous system, although for this more theoretical treatment we will simply consider the evolution a one-dimensional line $[0, L]$ (for example, representing a transect through the tumour front), where L is measured in millimetres. Note that the diffusion rate of glioblastoma cells is significantly higher than in normal cells (for example see [20]): our basic model therefore assumes that the migratory capacities of normal cells and the proliferative subpopulation is negligible, while the migratory subtype migrates but in an essentially random (i.e. diffusive) manner. Currently we assume that the region of the brain in which invasion is taking place is (effectively) homogeneous, and we take a spatially constant diffusion coefficient D_m (mm^2/day) to measure the degree of migration. The model is given by:

$$\begin{aligned} \frac{\partial n}{\partial t} &= h_n(n,p,m); \\ \frac{\partial p}{\partial t} &= h_v(n,p,m) - f(n,p,m)p + g(n,p,m)m; \\ \frac{\partial m}{\partial t} &= D_m \triangle m + f(n,p,m)p - g(n,p,m)m. \end{aligned} \tag{3.2}$$

In the above, h_n and h_v are functions that describe the growth of normal and malignant cells: growth is assumed to be limited by competition between the various populations (e.g. for space, for nutrient *etc.*). The function f is the "switching function" from proliferating mutant cells to migrating mutant cells, and vice versa for g.

Functions for h_n, h_v, f and g are chosen as follows:

$$\begin{aligned} \frac{\partial n}{\partial t} &= r_1 n(1 - \frac{n}{k_1} - a_1 \frac{p+m}{k_2}); \\ \frac{\partial p}{\partial t} &= r_2 p(1 - \frac{p+m}{k_2} - a_2 \frac{n}{k_1}) - \phi[\alpha(s)p - (1-\alpha(s))m]; \\ \frac{\partial m}{\partial t} &= D_m \frac{\partial^2 m}{\partial x^2} + \phi[\alpha(s)p - (1-\alpha(s))m]. \end{aligned} \tag{3.3}$$

In the above $r_{1,2}$, $k_{1,2}$, $a_{1,2}$, D_m and ϕ are positive constants. Parameters r_1 and r_2 (typical units of day^{-1}) define the growth rates: we would often expect this to be higher for the mutant population. Population growth is assumed to be limited due to competition between the various populations, with k_1 and k_2 ($cells/mm^3$) defining the carrying capacities induced from self-competition (normal on normal or mutant on mutant) parameters, and a_1 and a_2 (dimensionless) measuring the cross-competition effects (mutant on normal and normal on mutant). We note that the population growth terms are a straightforward extension of the forms chosen in Chapter 2, with the competitive impact of malignant cells represented by the sum of the migratory and proliferative subtypes. As described in the previous chapter, "competition" could arise from many factors, such as an increased absorption of nutrients by mutant cells to a greater resilience against adverse environmental conditions. We note that we have assumed the mutant subpopulations exert identical competitive effects: distinct effects could be introduced, yet this would further increase the dimensionality of an already large parameter space.

To model the switching between migratory and proliferative phenotypes we introduce two concepts: a rate function ϕ (typical units days^{-1}) that measures the (maximum) rate at which switches can occur, and a probability function $\alpha \in [0,1]$ that denotes the probability of a switch into a migratory phenotype; conversely $1-\alpha \in [0,1]$ denotes the probability of a switch into a proliferative phenotype. Both ϕ and α can depend on local properties of their environment: obviously, there is a large range of potential dependencies, and here we will restrict to the case where ϕ is a constant, while α depends on the total density of cells, i.e. $\alpha(s)$.

For initial conditions, we consider a small and spatially-confined population of the proliferative mutated cells immersed in a generally healthy tissue: this could

correspond either to the early stages of a developing tumour, or mimicking an artificial experiment in which tumorous cells have been implanted within a healthy tissue environment. Specifically, we consider

$$\begin{aligned} n(x,0) &= k_1 - p(x,0); \\ p(x,0) &= \begin{cases} p_0 & \text{when } 0 \le x \le x^*, \\ 0 & \text{otherwise.} \end{cases} \\ m(x,0) &= 0. \end{aligned} \tag{3.4}$$

where we note that k_1 marks the healthy tissue steady state. Boundary conditions only need to be specified for the migratory population, where we assume no-loss (zero-flux) conditions:

$$m_x(0,t) = m_x(L,t) = 0. \tag{3.5}$$

3.2.1 Parameters

The kinetic terms that describe competition-impacted growth are essentially the same as those in Chapter 2, and we refer there for a discussion into the relation between expected normal and malignant growth. The new terms introduced stem from α and ϕ. α is a probability function $\alpha \in [0,1]$, while a study results of transplanted glioma cells into neonatal rat forebrain suggest that the time scale of cell division r_2 is typically lower than the phenotypic switch rate ϕ [30]. Thus, we vary ϕ to be $\phi >$ or $< r_2$ say $\phi \in [0,10]$.

3.2.2 Non-dimensionalisation

The precise details of the non-dimensionalisation will vary according to the precise form of the function $\alpha(s)$. Here we illustrate via the non-dimensionalisation for $\alpha(s) = \alpha$, constant, where $\alpha \in [0,1]$. Specifically, we choose the scalings

$$n^* = \frac{n}{k_1}, \qquad m^* = \frac{m}{k_2}, \qquad p^* = \frac{p}{k_2}, \qquad t^* = r_1 t, \qquad x^* = \sqrt{r_1/D_m}x,$$

and set

$$b = \frac{r_2}{r_1}, \qquad \phi^* = \frac{\phi}{r_1}.$$

Substituting the above into equations (3.3) and dropping the *'s (for notational simplicity) we obtain:

$$\begin{aligned} \frac{\partial n}{\partial t} &= n(1 - n - a_1(p + m)); \\ \frac{\partial p}{\partial t} &= bp(1 - (p + m) - a_2 n) - \phi[\alpha p - (1 - \alpha)m]; \\ \frac{\partial m}{\partial t} &= \frac{\partial^2 m}{\partial x^2} + \phi[\alpha p - (1 - \alpha)m]. \end{aligned} \tag{3.6}$$

We note that the dimensionless parameters a_1, a_2 and α are unchanged as a result of the non-dimensionalisation.

3.3 Analysis of the non-spatially uniform case

3.3.1 Constant switching forms

To obtain some initial insight we begin with an analysis of the simplest scenario: the non-spatial problem setting ($\frac{\partial^2 m}{\partial x^2} = 0$) and assume a constant α. Specifically, we explore the steady states and determine the stability of the non-dimensionalised equations

$$\begin{aligned} \frac{dn}{dt} &= n(1 - n - a_1(p + m)); \\ \frac{dp}{dt} &= bp(1 - (p + m) - a_2 n) - \phi[\alpha p - (1 - \alpha)m]; \\ \frac{dm}{dt} &= \phi[\alpha p - (1 - \alpha)m]. \end{aligned} \tag{3.7}$$

It is logical to start our analysis by finding the steady states of the model.

3.3.2 Steady States

Setting the RHS terms in equations (3.7) to zero and solving for n, p and m gives the following steady states. The steady states of the model are determined as follows:

1. $(0, 0, 0)$. (trivial)

2. $(1, 0, 0)$. (healthy tissue)

3. $(0, 1-\alpha, \alpha)$. (fully-mutated tissue)

4. $\left(\frac{1-a_1}{1-a_1a_2}, (1-\alpha)\frac{1-a_2}{1-a_1a_2}, \alpha\frac{1-a_2}{1-a_1a_2}\right)$. (partially-mutated tissue)

In comparison to the simpler model of the previous chapter, we note that the above generates the same basic four steady state types, only the mutated component is divided into proliferative and migratory sub-types according to the parameter α.

3.3.3 Linear stability analysis

Stability of the steady state is determined by the community matrix of the system (3.7), which is given by

$$J = \begin{bmatrix} 1-2n^*-a_1(p^*+m^*) & -a_1n^* & -a_1n^* \\ -ba_2p^* & b-b(2p^*+m^*)-ba_2n^*-\phi\alpha & -bp^*+\phi(1-\alpha) \\ 0 & \phi\alpha & -\phi(1-\alpha) \end{bmatrix}.$$

Given the initial conditions, the relevant case of interest is a generally healthy tissue perturbed through the introduction of a small mutated population: hence we are interested in the stability of the healthy tissue. We therefore determine the eigenvalues λ of the community matrix at the steady state $(1, 0, 0)$, i.e.:

$$|J-\lambda I| = \begin{vmatrix} -1-\lambda & -a_1 & -a_1 \\ 0 & (b-ba_2-\phi\alpha)-\lambda & \phi(1-\alpha) \\ 0 & \phi\alpha & -[\phi(1-\alpha)]-\lambda \end{vmatrix} = 0.$$

This gives characteristic equation

$$(-1-\lambda)\begin{vmatrix} (b-ba_2-\phi\alpha)-\lambda & \phi(1-\alpha) \\ \phi\alpha & -[\phi(1-\alpha)]-\lambda \end{vmatrix} = 0.$$

Clearly, from the above we have at least one negative eigenvalue given by $\lambda_1 = -1$. For the other eigenvalues we consider separately the cases $\alpha = 0$, $0 < \alpha < 1$ and $\alpha = 1$:

Case 1: $\alpha = 0$

Here we obtain $\lambda_2 = b(1 - a_2)$ and $\lambda_3 = -\phi$. Consequently we will have instability of the healthy tissue steady state for

$$a_2 < 1\,. \tag{3.8}$$

In other words, we expect the healthy tissue to be destabilised (potentially implying growth in the mutated population) when the competition of normal cells on mutant cells is weak. This is exactly the condition in the simpler two-species model of Chapter 2: intuitively, for this situation the cells remain trapped in the proliferative phenotype and the model is effectively reduced to the simpler classical competition model of Chapter 2.

Case 2: $0 < \alpha < 1$

Here, $\lambda_{2,3}$ are determined from the roots of the quadratic equation:

$$\lambda^2 - (b(1 - a_2) - \phi)\lambda - \phi(1 - \alpha)b(1 - a_2) = 0\,, \tag{3.9}$$

i.e.

$$\lambda_{2,3} = 1/2\{(b(1 - a_2) - \phi) \pm \sqrt{(b(1 - a_2) - \phi)^2 + 4\phi(1 - \alpha)b(1 - a_2)}\}.$$

Here, instability of the healthy tissue steady state again occurs for

$$a_2 < 1\,. \tag{3.10}$$

Case 3: $\alpha = 1$

Here, $\lambda_{2,3}$ are determined by $\lambda_2 = b(1-a_2)-\phi$ and $\lambda_3 = 0$. One eigenvalue is always zero and the steady state is unstable for

$$b(1 - a_2) - \phi > 0. \tag{3.11}$$

The size of the largest positive value of λ of equation (3.9) indicates the rate at which solutions diverge from the steady state and, to some degree, can be used as a predictor of the "aggressiveness" of the tumour, i.e. the rate at which the tumour will grow and begin to replace the normal population.

In Figure 3.2 we plot the size of the largest positive eigenvalue in the parameter space $\phi - \alpha$. For ϕ we choose a range between 0 and 10, while α between 0 and 1. We consider two fixed combinations for (a_1, a_2, b): (a) $(1, 0.5, 2)$, representing a "slowly growing tumour", defined as one in which the proliferation rate of tumour cells is only twice that of the normal population; (b) $(1, 0.5, 5)$, representing a "rapidly growing tumour", where the tumour cells divide an order of magnitude faster than the normal population. For both cases, the most aggressive tumours occurs when ϕ and α are small. Intuitively, this is due to much less frequent switching from proliferating to migrating cells, hence allowing the tumour population to proliferate quickly and rapidly replace the normal population.

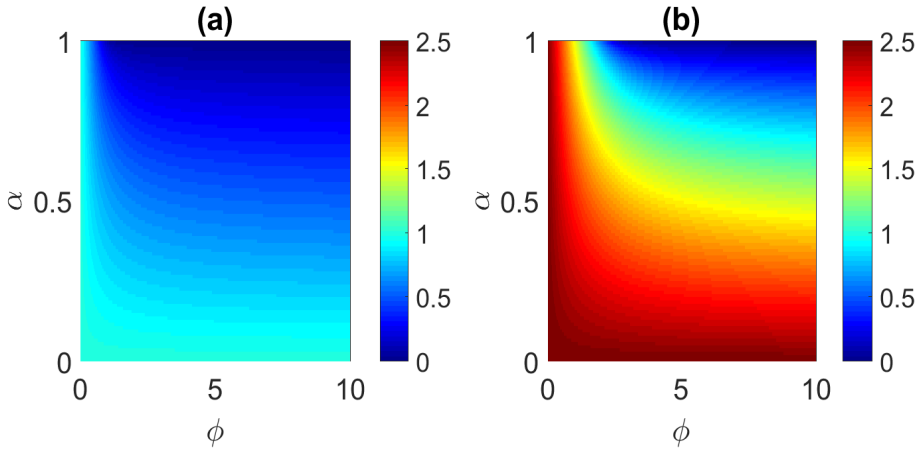

Figure 3.2: Plot of the size of the largest positive eigenvalue of equation (3.9) for ϕ vs α and fixed (a_1, a_2, b). (a) $(1, 0.5, 2)$, (b) $(1, 0.5, 5)$.

3.3.4 Numerical simulations

The linear stability analysis indicates behaviour near the steady state, but for an understanding of the nonlinear dynamics we perform a numerical simulation study. We consider the same two fixed combinations for (a_1, a_2, b) and measure the first time at which the sum of mutant cells $(m + p)$ exceeds the normal population (n) of model (3.7) i.e the first time $t^* \geq 0$ for which $p(t^*) + m(t^*) \geq n(t^*)$. Figure

3.3 shows simulation time courses at different (α, ϕ) combinations for the "slowly growing tumour" $(a_1 = 1, a_2 = 0.5, b = 2)$ case defined above. When $\alpha = 0$ no migrating cells are noted, and the model reduces to the competition model (2.4). When $\alpha = 0.5$, cells spend a greater proportion of time migrating over proliferating, with this transition becoming much more rapid at large values of ϕ. As a result, the time when the total tumour cell population exceeds the normal cells is increasing with ϕ. For the largest α, $\alpha = 1$, proliferating tumor cells switch and become blocked in the migratory phase. Whether the tumour population overcomes the normal tissue now critically depends on the size of ϕ. If ϕ is small, the tumour cells make this switch relatively slowly: there is sufficient time for the proliferating cell population to outcompete the normal cell population before becoming trapped as migrating cells. For larger ϕ, however, proliferating cells rapidly switch into the migratory phenotype and we do not observe any tumour takeover inside the timeframe of the simulation.

Figure 3.4 shows a similar set of results for our "fast growing tumour" scenario $(a_1 = 1, a_2 = 0.5, b = 10)$. We observe similar behavior to Figure 3.3, yet the overall growth rate is much higher for all ϕ and α cases considered: this leads to the fastest growing tumours. For the special case $\alpha = 1$, the stability of the normal cells depends on condition (3.11).

In Figure 3.5 we measure the tumour aggressiveness in terms of the numerically calculated time at which the sum of mutant cells $(m + p)$ exceeds the normal population (n) for the same two scenarios, (a) $a_1 = 1, a_2 = 0.5, b = 2$, (b) $a_1 = 1, a_2 = 0.5, b = 10$. The relationship between (α, ϕ) and aggressiveness correlates with our earlier predictions based on the magnitude of the largest positive eigenvalue: for small α and small ϕ we have the most aggressive scenario, with the tumour rapidly overcoming the normal population. Conversely, for large α and large ϕ, the rapid switch and "blocking" into a migratory phenotype reduces the size of the proliferating population and the tumour needs relatively long to overcome the normal population. Of course, this "benefit" naturally comes at an increased population of circulating migratory cells, and we will therefore later to expand to a

partial-differential equation model to explore the impact on invasiveness/spread.

For the "slowly growing tumour" ($a_1 = 1, a_2 = 0.5, b = 2$) case we plot the percentage difference in the amount of time that the glioma needs to exceed the normal cells, based on $\alpha = 0.5$ as the reference case (see Figure 3.6), we observe that for a fixed $\phi = 0.5$, increasing the probability of switching to migratory type increases the time taken for tumour cells to surpass the normal cell density increases as the number of proliferating cells decreases. A lower value of ϕ has the same effect, yet the percentage differences are relatively small, see Figure 3.7.

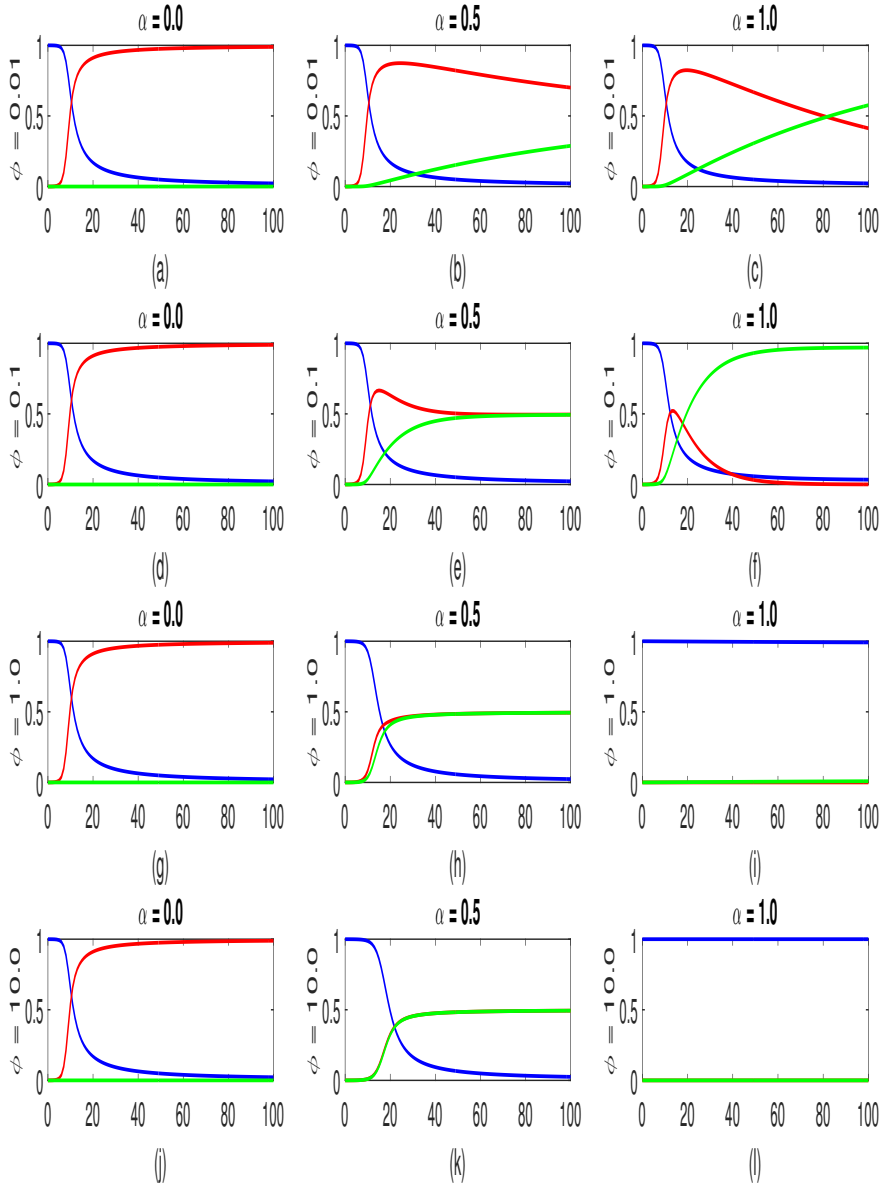

Figure 3.3: Simulations of model (3.7) with initial conditions (3.4) for different values of α and ϕ and fixed $b = 2$, $a_1 = 1.0$ and $a_2 = 0.5$. We plot normal (blue), proliferative mutant (red) and migrating mutant (green) population densities as functions of time. (a) $\alpha = 0.0$ $\phi = 0.01$, (b) $\alpha = 0.5$ $\phi = 0.01$, (c) $\alpha = 1.0$ $\phi = 0.01$, (d) $\alpha = 0.0$ $\phi = 0.1$, (e) $\alpha = 0.5$ $\phi = 0.1$, (f) $\alpha = 1.0$ $\phi = 0.1$, (g) $\alpha = 0.0$ $\phi = 1.0$, (h) $\alpha = 0.5$ $\phi = 1.0$, (i) $\alpha = 1.0$ $\phi = 1.0$, (j) $\alpha = 0.0$ $\phi = 10.0$, (k) $\alpha = 0.5$ $\phi = 10.0$, (l) $\alpha = 1.0$ $\phi = 10.0$. These simulation were solved in Matlab using the ODE solver "ode15s", with a relative tolerance $= 10^{-9}$ and absolute tolerance $= 10^{-12}$.

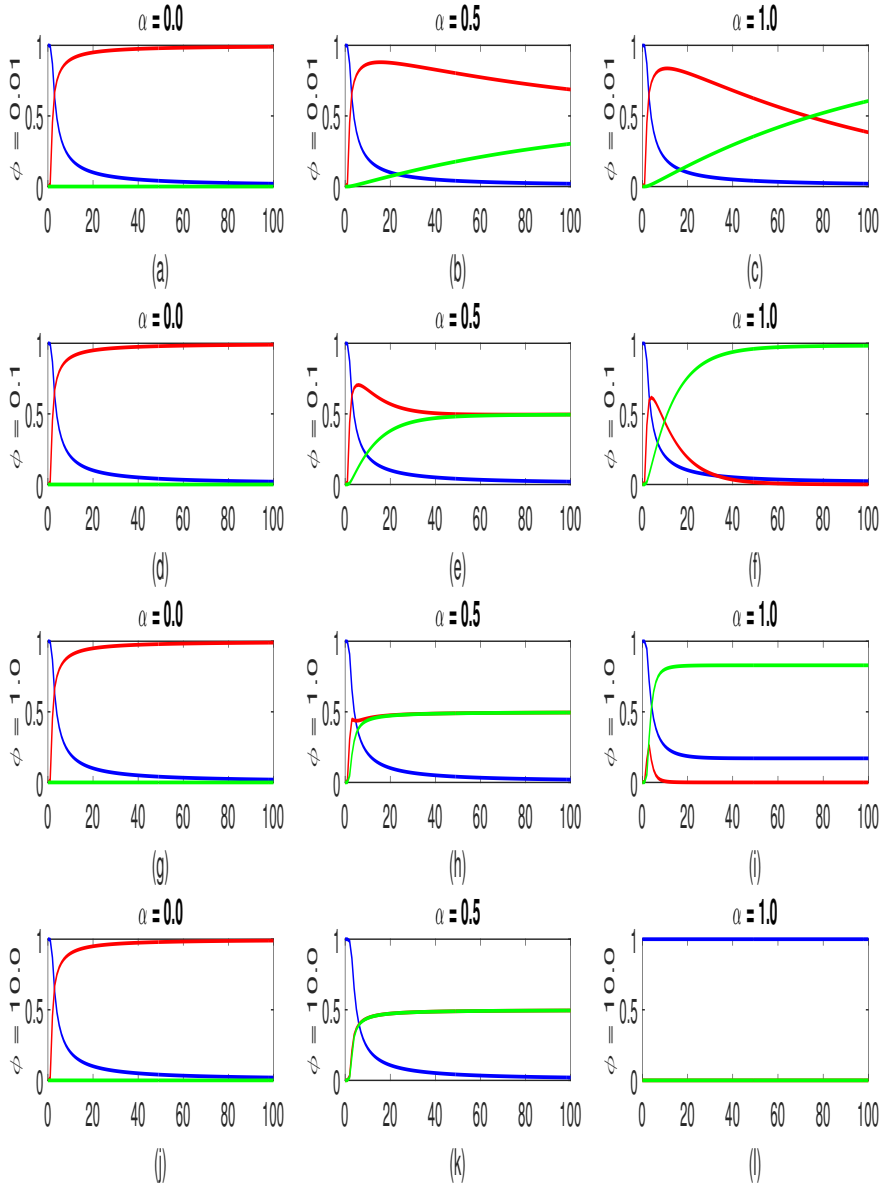

Figure 3.4: Simulations of model (3.7) with initial conditions (3.4) for different values of α and ϕ and fixed $b = 10$, $a_1 = 1.0$ and $a_2 = 0.5$. We plot normal (blue), proliferative mutant (red) and migrating mutant (green) population densities as functions of time. (a) $\alpha = 0.0$ $\phi = 0.01$, (b) $\alpha = 0.5$ $\phi = 0.01$, (c) $\alpha = 1.0$ $\phi = 0.01$, (d) $\alpha = 0.0$ $\phi = 0.1$, (e) $\alpha = 0.5$ $\phi = 0.1$, (f) $\alpha = 1.0$ $\phi = 0.1$, (g) $\alpha = 0.0$ $\phi = 1.0$, (h) $\alpha = 0.5$ $\phi = 1.0$, (i) $\alpha = 1.0$ $\phi = 1.0$, (j) $\alpha = 0.0$ $\phi = 10.0$, (k) $\alpha = 0.5$ $\phi = 10.0$, (l) $\alpha = 1.0$ $\phi = 10.0$. Numerics performed as in Figure 3.3.

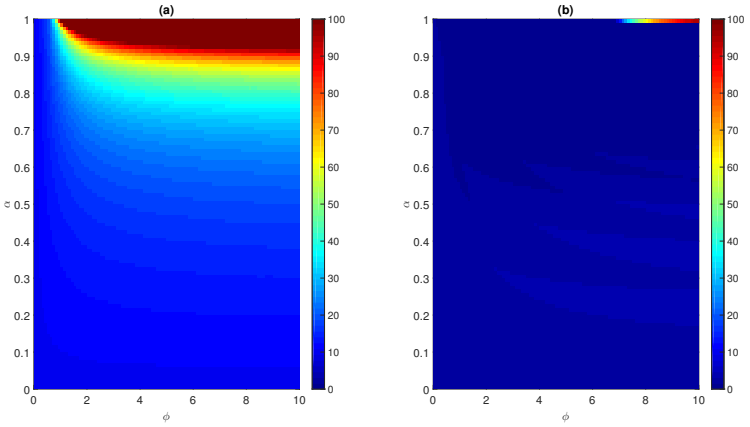

Figure 3.5: Simulations of model (3.7) with initial conditions (3.4) for different values of α and ϕ and fixed b, a_1 and a_2. We plot the time at which the sum of mutant cells $(m+p)$ exceeds the normal population (n). (a) $a_1 = 1, a_2 = 0.5, b = 2$, (b) $a_1 = 1, a_2 = 0.5, b = 10$. Numerics performed as in Figure 3.3.

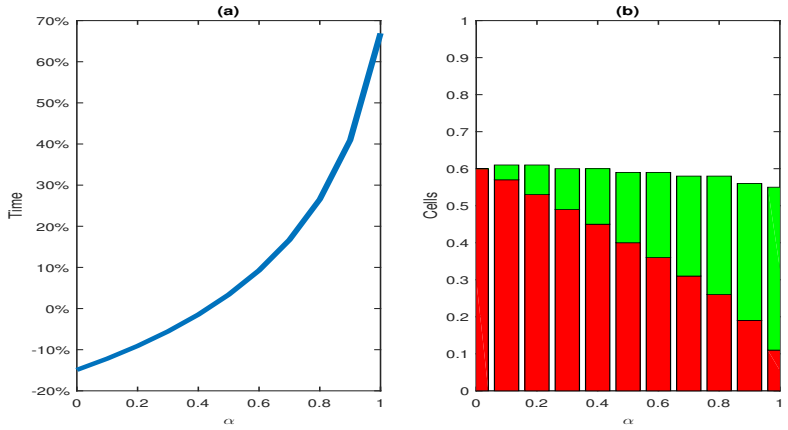

Figure 3.6: Simulations of model (3.7) with initial conditions (3.4). (a) We plot the minimum time for exceeding the normal cells by the tumour cells for different values of α. (b) We plot the number of proliferating (red)/migrating (green) tumour cells at that time. $\phi = 0.5, b = 2, a_1 = 1$ and $a_2 = 0.5$. Numerics performed as in Figure 3.3.

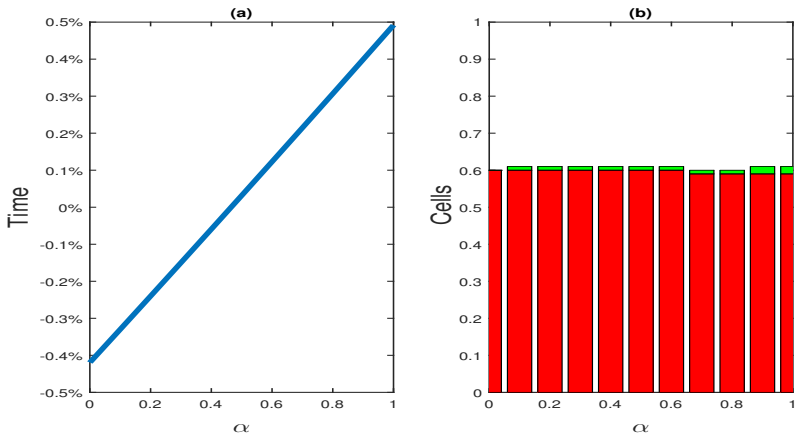

Figure 3.7: Simulations of model (3.7) with initial conditions (3.4). (a) We plot the minimum time for exceeding the normal cells by the tumour cells for different values of α. (b) We plot the number of proliferating (red)/migrating (green) tumour cells at that time. $\phi = 0.01, b = 2, a_1 = 1$ and $a_2 = 0.5$. Numerics performed as in Figure 3.3.

3.3.5 Density-dependent switching forms

Having analysed the constant α case, we next consider the impact of the local environment on switching in the form of density-dependent switching functions. Specifically, we consider α to be a function of the total cell density $S = n + p + m$ via two scenarios:

1. Decreasing α as the density S increases.

2. Increasing α as the density S increases.

In order to properly frame our functional forms for α we consider the expected range of variation in density as a normal tissue gradually becomes mutated. Returning to the nondimensional form of the equations (3.6), in a healthy tissue we have $S = k_1$ while for a fully-mutated tissue we have $S = k_2$, where we (typically) expect $k_2 > k_1$. The function α defines the probability of switching, and hence $\alpha(S) \in [0, 1]$. For ease of analysis, we assume a piecewise linear functional form that is constant for $S < k_1$ or $S > k_2$ and increasing/decreasing linearly for $k_1 \leq S \leq k_2$.

Specifically, we choose:

$$\alpha(S) = \begin{cases} \frac{1-\gamma}{2} & \text{if } S < k_1 \\ \frac{1}{k_2-k_1}\left(\gamma S + \frac{k_2-k_1-\gamma(k_1+k_2)}{2}\right) & \text{if } k_1 \leq S \leq k_2 \\ \frac{1+\gamma}{2} & \text{if } S > k_2 \end{cases}, \tag{3.12}$$

where the parameter $\gamma \in [-1, 1]$ controls the gradient of α as S increases between k_1 and k_2 while ensuring that α remains properly bounded within $[0, 1]$, see Figure 3.8.

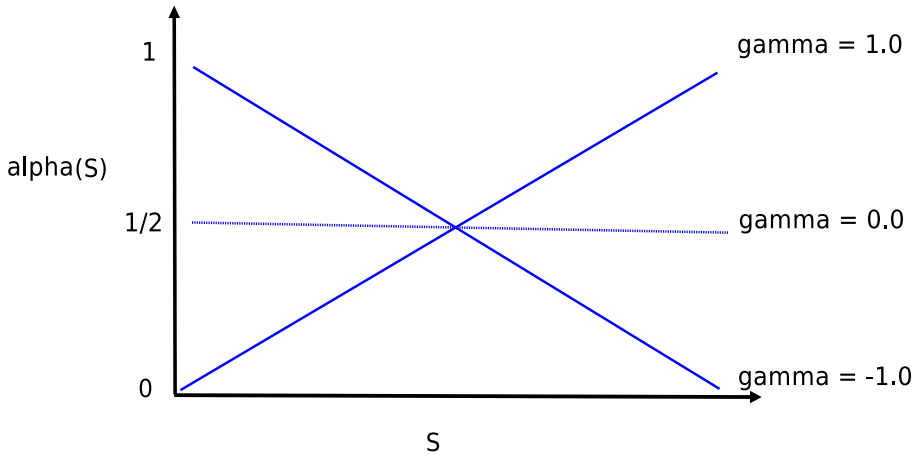

Figure 3.8: Sketch of the probability of switching α for different values of γ.

3.3.5.1 Nondimensionalisation, steady states and linear stability analysis

We apply the same scalings as for the constant α case (see Section 3.2.2) to obtain (after dropping the stars):

$$\begin{aligned} \frac{dn}{dt} &= n(1 - n - a_1(p + m)); \\ \frac{dp}{dt} &= bp(1 - (p + m) - a_2 n) - \phi[\alpha(S^*)p - (1 - \alpha(S^*))m]; \\ \frac{dm}{dt} &= \phi[\alpha(S^*)p - (1 - \alpha(S^*))m]. \end{aligned} \tag{3.13}$$

In the above, $S^* = k_1 n + k_2(m + p)$ with α as above. We remark that the nondimensionalisation is not quite so "useful" in this case, since we are unable to eliminate the

$k's$ from the function α. Nevertheless, performing the same nondimensionalisation aids the comparison between this and the simpler form. Steady states take the same basic forms:

- $(n, p, m) = (0, 0, 0)$ (trivial);
- $(n, p, m) = (1, 0, 0)$ (healthy);
- $(n, p, m) = (0, p_s, m_s)$, where $p_s + m_s = 1$ (fully-mutated);
- $(n, p, m) = (n_s, p_s, m_s)$ (partially-mutated).

As previously, our primary focus of interest is on the stability of the healthy tissue steady state. In particular, we explore the impact of α on the stability of the healthy tissue steady state. Stability of the steady state is determined by the community matrix of the system (3.13). We therefore determine the eigenvalues λ of the community matrix at the steady state $(1, 0, 0)$, which turns out to be the same as when α is constant, i.e.:

$$|J - \lambda I| = \begin{vmatrix} -1-\lambda & -a_1 & -a_1 \\ 0 & (b - ba_2 - \phi\alpha(S^*)) - \lambda & \phi(1-\alpha(S^*)) \\ 0 & \phi\alpha(S^*) & -[\phi(1-\alpha(S^*))] - \lambda \end{vmatrix} = 0.$$

This gives characteristic equation

$$(-1-\lambda)\begin{vmatrix} (b - ba_2 - \phi\alpha(S^*)) - \lambda & \phi(1-\alpha(S^*)) \\ \phi\alpha(S^*) & -[\phi(1-\alpha(S^*))] - \lambda \end{vmatrix} = 0\,,$$

where $\lambda_1 = -1$ and

$$\lambda_{2,3} = 1/2\{(b(1-a_2) - \phi) \pm \sqrt{(b(1-a_2)-\phi)^2 + 4\phi(1-\alpha(S^*)b(1-a_2)}\}.$$

These have the same stability conditions as when α is constant, since $\alpha(S^*) \in [0, 1]$. Thus:

- The normal cells remain stable when $a_2 > 1$ for $\alpha(S^*) < 1$.

- The condition for normal cells to be stable is $(b(1-a_2)-\phi) < 0$ for $\alpha(S^*) = 1$

.

3.3.5.2 Numerical simulations

We turn to a numerical simulation study, exploring how the system dynamics change as we systematically change the function α. Specifically, we will change γ between -1 and 1:

- When $\gamma = -1.0$ the slope of $\alpha(S^*)$ is negative and at its steepest. Therefore, $\alpha(S^*)$ is a decreasing function of S^* and if the total number of cells increases then the probability of proliferating tumour cells switching to a migratory type decreases.

- When $\gamma = 0.0$ the slope of $\alpha(S^*)$ is zero. Thus $\alpha(S^*) = 0.5$ for all time.

- When $\gamma = 1.0$ the slope of α is positive. Thus the function $\alpha(S^*)$ increases as the total number of cells increases: i.e. if the total number of cells increases then the probability of a proliferating tumour cell switching to a migratory type increases.

For the above three values of γ we consider the same two fixed combinations for (a_1, a_2, b) considered previously and again measure the time at which the total mutant population $(m + p)$ exceeds the normal population (n) of model (3.13). Figure 3.9 shows simulations of the ODE model for our slowly-growing tumour $(a_1 = 1, a_2 = 0.5, b = 2)$, while Figure 3.10 shows the result for our quickly-growing tumour $(a_1 = 1, a_2 = 0.5, b = 10)$. From Figure 3.9 we see that as fewer proliferating tumour cells switch to a migrating type, the time needed to exceed the normal cell population is increased: these results echo our observations under constant switching rates, α. Increasing ϕ acts to extend the time before takeover, as cells switch more quickly into the migratory phenotype. The results are similar for the fast-growing tumour scenario, although the time before takeover is greatly shortened (as expected).

Much more subtle is the dependence on γ, which alters the density-dependent effect on switching. Here the time to takeover increases as the rate of switching (ϕ) increases. If the probability of switching between the two tumour subpopulations is constant with density (i.e $\gamma = 0$) the number of proliferating tumour cells declines towards the level of migratory cells with increased ϕ. For an increasing α with $S*$, we observe more migrating cells as we increase ϕ, and the time to exceed the normal cell population drops.

Increasing the rate of tumour cell proliferation accelerates these results: we observe the takeover in faster times if we have fast growing tumours. Regardless of the balance between proliferating or migrating cells, the tumour dominates quickly if b is increased, so that we observe negligible impact with ϕ (see Figure 3.10).

We examine how the minimum time for exceeding the normal cells by glioma cells alters with regard to γ and the competition parameters. We choose three different values of the competitive parameter of glioma cells on normal cells a_1, $(0.6, 1.0$ & $2.0)$ and plot the minimum time and the number of proliferating and migrating glioma cells for these three different values with fixed $\phi = 0.5, b = 2, a_2 = 0.5$, for each a_1, we vary γ between -1 and 1 and plot how the minimum time for the tumour population to exceed the normal population changes, expressing the results as the % change from the $\gamma = 0$ case (Figure 3.11). Moving through rows in the first column, we observe an increase in the percentage of time required as a_1 increases with $\gamma = -1$, and a decrease with $\gamma = 1$. Moving through rows in the second column, reflect the number of proliferating cells, showing a decrease when $\gamma = -1$ and as we increase a_1 and an increase when $\gamma = 1$.

We next perform the same study but with three different values of the competitive parameter of normal cells on glioma cells a_2, $(0.1, 0.4$ & $0.7)$. We plot the minimum time and the number of proliferating and migrating glioma cells for these three different values of a_2 with fixed $\phi = 0.5, b = 2, a_1 = 1.0$ see Figure 3.12. Moving through rows in the first column, we observe a huge increase in the percentage in the time as a_2 increase with $\gamma = -1$ and decrease with $\gamma = 1$. Moving through rows in the second column, the number of proliferating cells decrease almost for all values

of γ.

For the three different values of ϕ, $(0.01, 0.1$ & $1.0)$ with fixed $a_2 = 0.5, b = 2, a_1 = 1.0$ see Figure 3.13. Moving through rows in the first column, we observe a huge increase in the percentage in the time as ϕ increases with $\gamma = -1$ and decreases with $\gamma = 1$. Moving through rows in the second column, the number of proliferating cells decrease for almost all values of γ.

To summarise, for all sets of parameters a large impact on the time required to exceed the normal cells occurs when α is an increasing function with S^* (i.e $\gamma > 0$). In other words, less time is required for tumour to dominate if the switch to migratory state is increasing with the total density.

3.3.6 Summary

Summarising, under a constant switch form we find that increasing α increases the proportion of migrating tumor cells in the system, hence reduces the number of proliferating cells and lowers the time for the cancerous tissue to dominate. Decreasing ϕ decreases the migrating tumour cells in the system and decreases the time for cancerous tissue to form. The value of ϕ is crucial in the special case $\alpha = 1$, since the instability of normal cells depends on the condition $b(1-a_2)-\phi > 0$. Increasing the proliferating ratio b decreases the time taken for cancerous tissue to dominate. Under the density-dependent switching forms we find that a negative slope ($\gamma = -1$), i.e a decreasing switch function with S^*, results in more proliferating cells than migrating cells in the system, while positive slope results in more migrating cells. For a constant slope $\gamma = 0$, the number of proliferating cells decreases as ϕ increases. Summarising, the form and rate of switching will have an impact on how quickly a tumour can form.

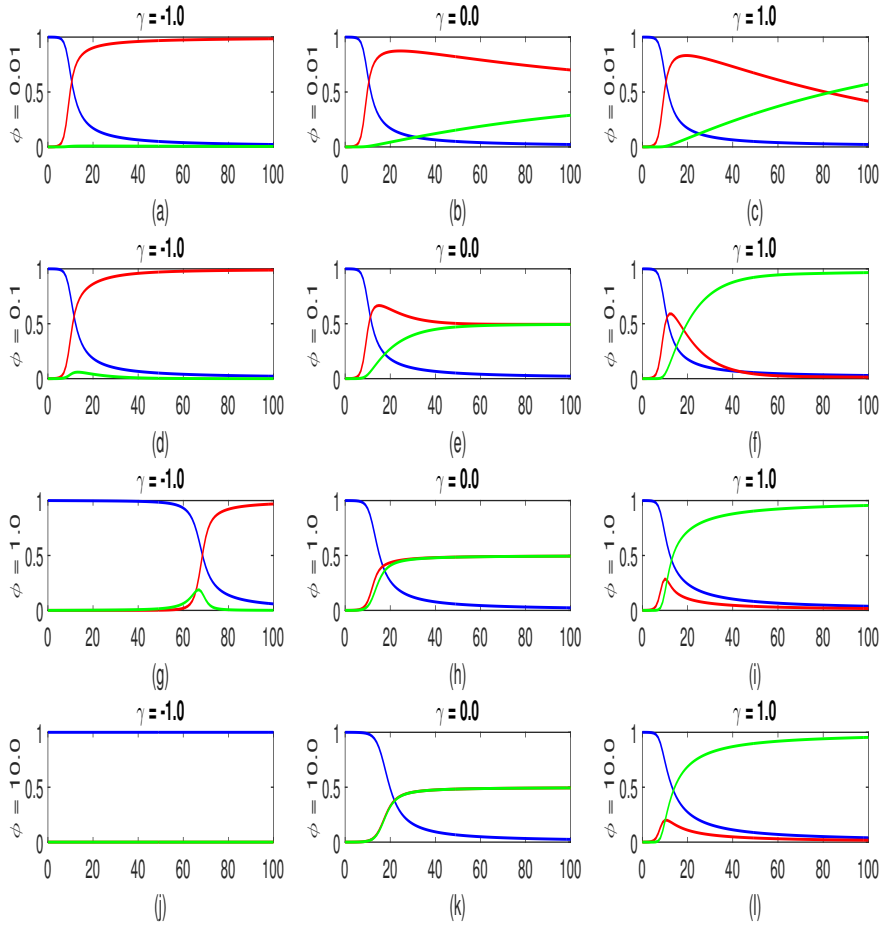

Figure 3.9: Simulations of model (3.13) with initial conditions (3.4) for different values of γ and ϕ and fixed $b = 2$, $a_1 = 1.0$ and $a_2 = 0.5$. We plot normal (blue), proliferative mutant (red) and migrating mutant (green) population densities as functions of time. (a) $\gamma = -1.0$ $\phi = 0.01$, (b) $\gamma = 0.0$ $\phi = 0.01$, (c) $\gamma = 1.0$ $\phi = 0.01$, (d) $\gamma = -1.0$ $\phi = 0.1$, (e) $\gamma = 0.0$ $\phi = 0.1$, (f) $\gamma = 1.0$ $\phi = 0.1$, (g) $\gamma = -1.0$ $\phi = 1.0$, (h) $\gamma = 0.0$ $\phi = 1.0$, (i) $\gamma = 1.0$ $\phi = 1.0$, (j) $\gamma = -1.0$ $\phi = 10.0$, (k) $\gamma = 0.0$ $\phi = 10.0$, (l) $\gamma = 1.0$ $\phi = 10.0$. Numerics performed as in Figure 3.3.

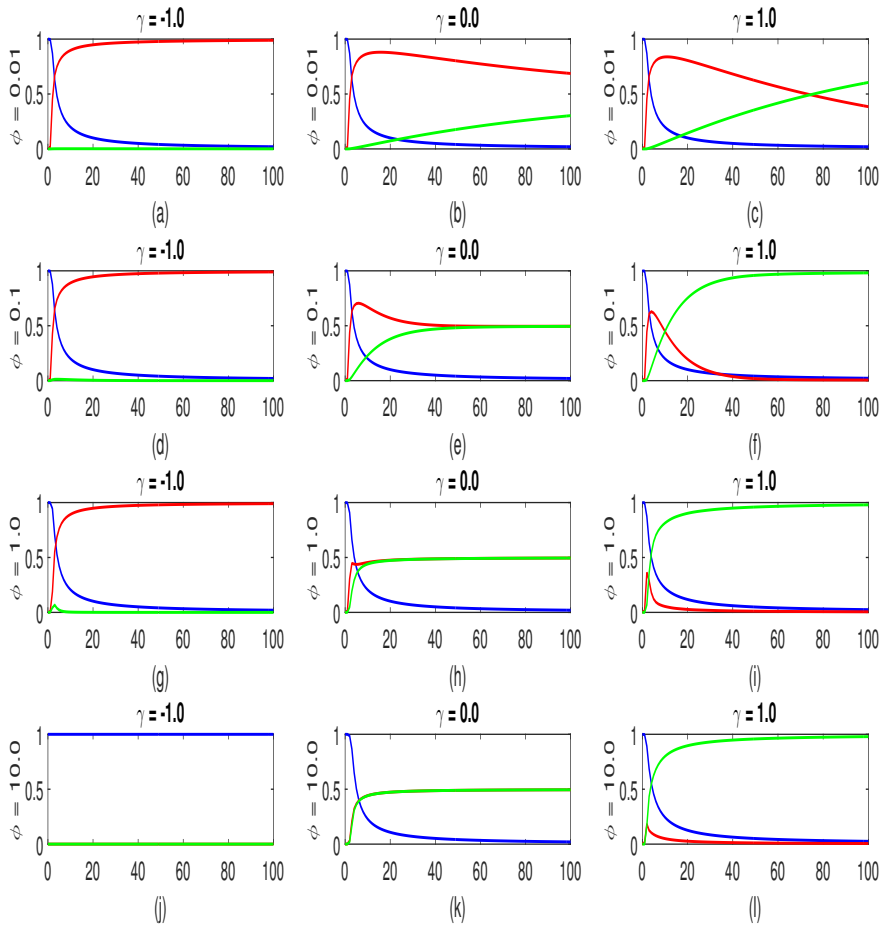

Figure 3.10: Simulations of model (3.13) with initial conditions (3.4) for different values of γ and ϕ and fixed $b = 10$, $a_1 = 1.0$ and $a_2 = 0.5$. We plot normal (blue), proliverative mutant (red) and migrating mutant (green) population densities as functions of time. (a) $\gamma = -1.0$ $\phi = 0.01$, (b) $\gamma = 0.0$ $\phi = 0.01$, (c) $\gamma = 1.0$ $\phi = 0.01$, (d) $\gamma = -1.0$ $\phi = 0.1$, (e) $\gamma = 0.0$ $\phi = 0.1$, (f) $\gamma = 1.0$ $\phi = 0.1$, (g) $\gamma = -1.0$ $\phi = 1.0$, (h) $\gamma = 0.0$ $\phi = 1.0$, (i) $\gamma = 1.0$ $\phi = 1.0$, (j) $\gamma = -1.0$ $\phi = 10.0$, (k) $\gamma = 0.0$ $\phi = 10.0$, (l) $\gamma = 1.0$ $\phi = 10.0$. Numerics performed as in Figure 3.3.

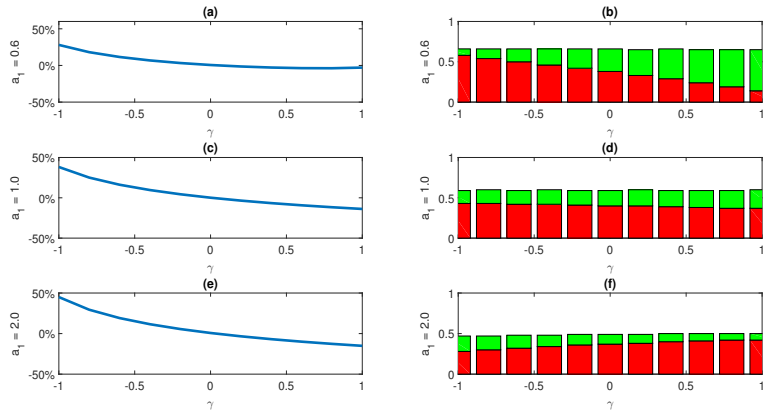

Figure 3.11: Simulations of model (3.13) with initial conditions (3.4). (a) Plot of the minimum time for exceeding the normal cells by the tumour cells for different values of γ. (b) Plot of the amount of proliferating (red)/migrating (green) tumour cells at that time. Other parameters fixed at $\phi = 0.5, b = 2$ and $a_2 = 0.5$. Numerics performed as in Figure 3.3.

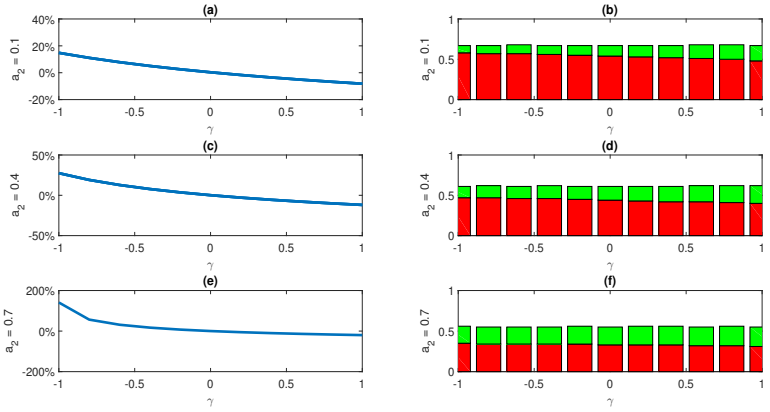

Figure 3.12: Simulations of model (3.13). (a) Plot of the minimum time for exceeding the normal cells by the tumour cells for different values of γ. (b) Plot of the amount of proliferating (red)/migrating (green) tumour cells at that time. Other parameters fixed at $\phi = 0.5, b = 2, a_1 = 1$. Numerics performed as in Figure 3.3.

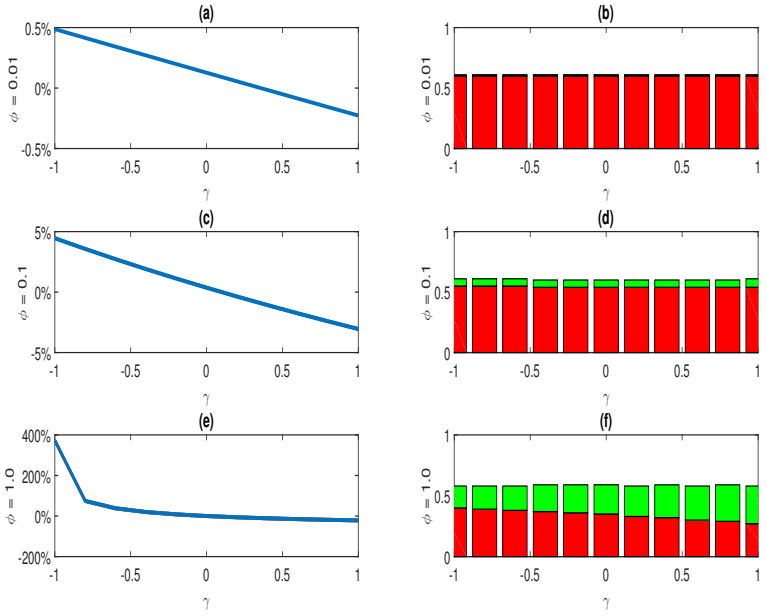

Figure 3.13: Simulations of model (3.13). (a) Plot of the minimum time for exceeding the normal cells by the tumour cells for different values of γ. (b) Plot of the amount of proliferating (red)/migrating (green) tumour cells at that time. Other parameters fixed at $b = 2, a_1 = 1$ and $a_2 = 0.5$. Numerics performed as in Figure 3.3.

3.4 Analysis of the spatial case

The results above suggest that switching between migratory and proliferative phenotype can act to accelerate/slow the rate at which a mutant population replaces a healthy population: lowering the pool of proliferative cells will slow down the rate of takeover. Of course, the natural downside of this is a larger population of migrating cells. We therefore extend our study to investigate the consequence on tumour invasion through extension to a partial-differential equation model. Specifically, we now study the full go-or-grow competition model (3.6) with initial condition (3.4) and boundary condition (3.5).

3.4.1 Numerical analysis under constant switching forms

To investigate how the dynamics of the tumour change over space and time, we begin our exploration for a constant switching form for α. We run simulations on the domain $x = [0, 300]$ and $t = [0, 200]$ and, in Figure 3.14, plot the two subpopulations of tumour cells under different values of α and ϕ while fixing the rest of the parameters. Specifically, we consider $\alpha = 0.25, 0.5, 0.75$, $\phi = 0.01, 0.1, 1.0, 10.0$ and our slowly-growing tumour case, $a_1 = 1.0, a_2 = 0.5, b = 2$.

The size of α determines the proportion of migrating to proliferating cells: therefore, for small α we expect to see lower numbers of migrating cells and for large α we expect a higher proportion. However, the size of ϕ also determines the rate at which the transition takes place, so that when ϕ is small (e.g. $\phi = 0.01$) migrating tumour cells will only form a small fraction near the wavefront, where proliferation dominates the replacement of healthy tissue with tumour cells, but will gradually increase towards the back of the wave. When $\alpha = 0.5$ the wave fronts of the two subpopulations are almost identical when $\phi \geq 1$ (see Figure 3.14 (h) and (k)). The wavefront of migrating tumour cells is higher than of that the proliferating tumour cells when $\alpha > 0.5$, and lower when $\alpha < 0.5$. This does not appear the case when ϕ is small i.e < 0.1. However, the total tumour cell population behaves almost the same for all ϕ and α, see Figure 3.15, except at the critical values of $\alpha = \phi = 0.0$ and $\alpha = 1.0$. Figure 3.16 shows the two subpopulations along with the normal of the system. These simulations strongly suggest the formation of travelling waves, and we therefore begin a travelling wave analysis.

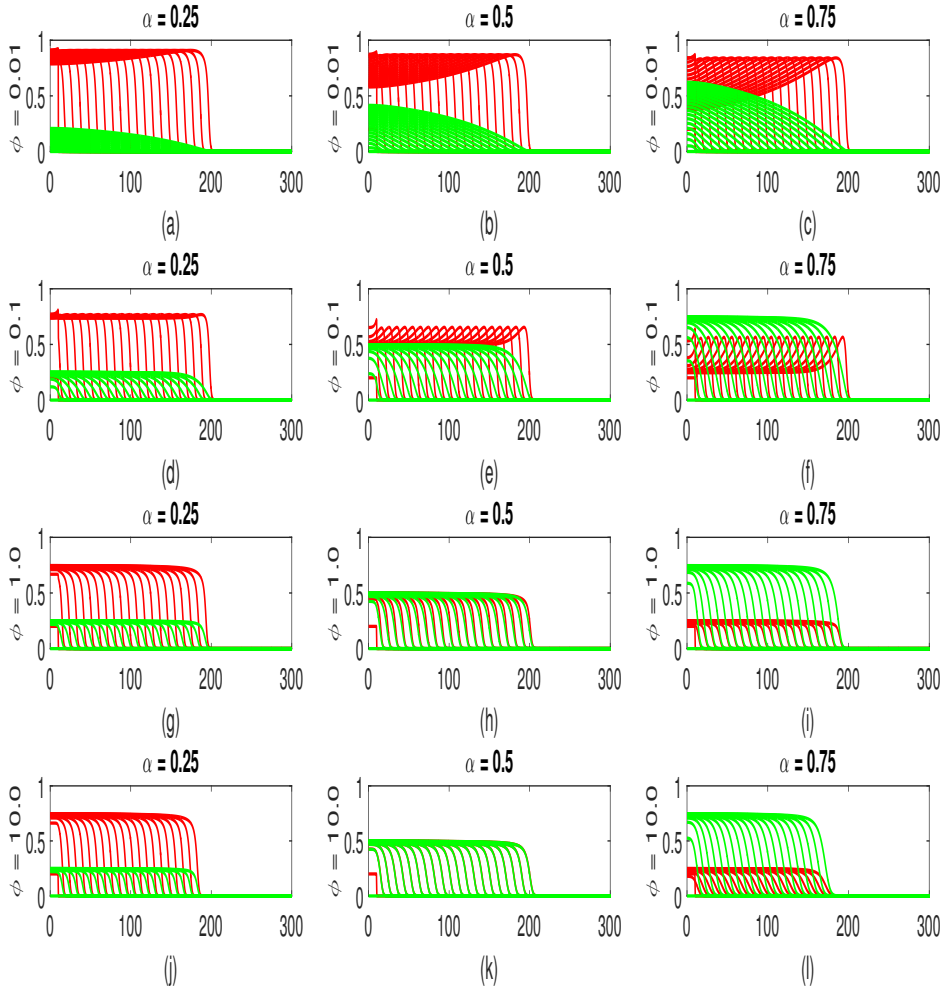

Figure 3.14: Simulations of model (3.6) with initial condition (3.4) and boundary condition (3.5) for different values of α, ϕ and fixed $a_1 = 1.0, a_2 = 0.5$ and $b = 2$. We plot mutant proliferating (red) and mutant migrating (green) populations as functions of time and space. (a) $\phi = 0.01, \alpha = 0.25$. (b) $\phi = 0.01, \alpha = 0.5$. (c) $\phi = 0.01, \alpha = 0.75$. (d) $\phi = 0.1, \alpha = 0.25$. (e) $\phi = 0.1, \alpha = 0.5$. (f) $\phi = 0.1, \alpha = 0.75$.(g) $\phi = 1.0, \alpha = 0.25$. (h) $\phi = 1.0, \alpha = 0.5$.(i) $\phi = 1.0, \alpha = 0.75$.(j) $\phi = 1.0, \alpha = 0.25$. (k) $\phi = 1.0, \alpha = 0.5$.(l) $\phi = 1.0, \alpha = 0.75$. The equations were solved numerically for time interval $0 \leq t \leq 200$, and on a length interval $0 \leq x \leq 300$, using Pdepe solver in Matlab, with a relative tolerance $= 10^{-9}$, absolute tolerance $= 10^{-12}$ and grid spacing of 0.25.

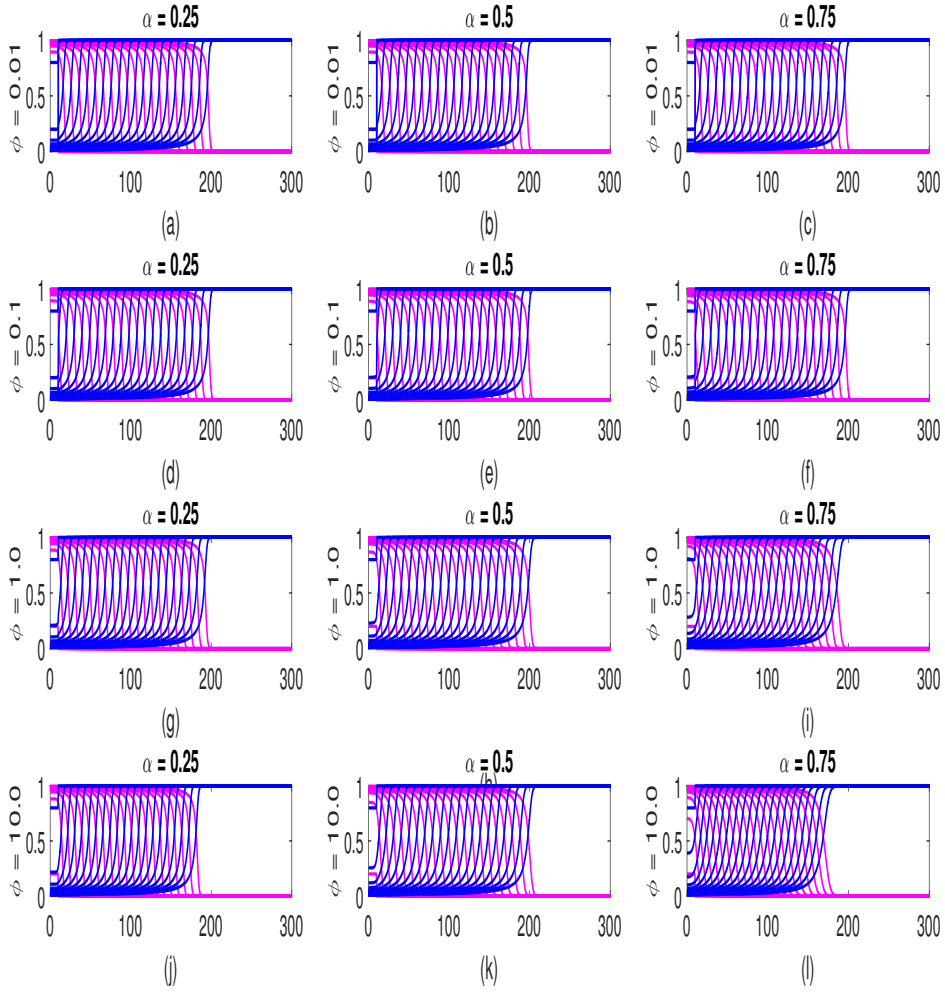

Figure 3.15: Simulations of model (3.6) with initial condition (3.4) and boundary condition (3.5) for different values of α, ϕ and fixed $a_1 = 1.0, a_2 = 0.5$ and $b = 2$. We plot normal (blue) and total mutant (magenta) populations as functions of time and space. (a) $\phi = 0.01, \alpha = 0.25$. (b) $\phi = 0.01, \alpha = 0.5$. (c) $\phi = 0.01, \alpha = 0.75$. (d) $\phi = 0.1, \alpha = 0.25$. (e) $\phi = 0.1, \alpha = 0.5$. (f) $\phi = 0.1, \alpha = 0.75$.(g) $\phi = 1.0, \alpha = 0.25$. (h) $\phi = 1.0, \alpha = 0.5$.(i) $\phi = 1.0, \alpha = 0.75$.(j) $\phi = 1.0, \alpha = 0.25$. (k) $\phi = 1.0, \alpha = 0.5$.(l) $\phi = 1.0, \alpha = 0.75$. The numerical method was as in Figure 3.14.

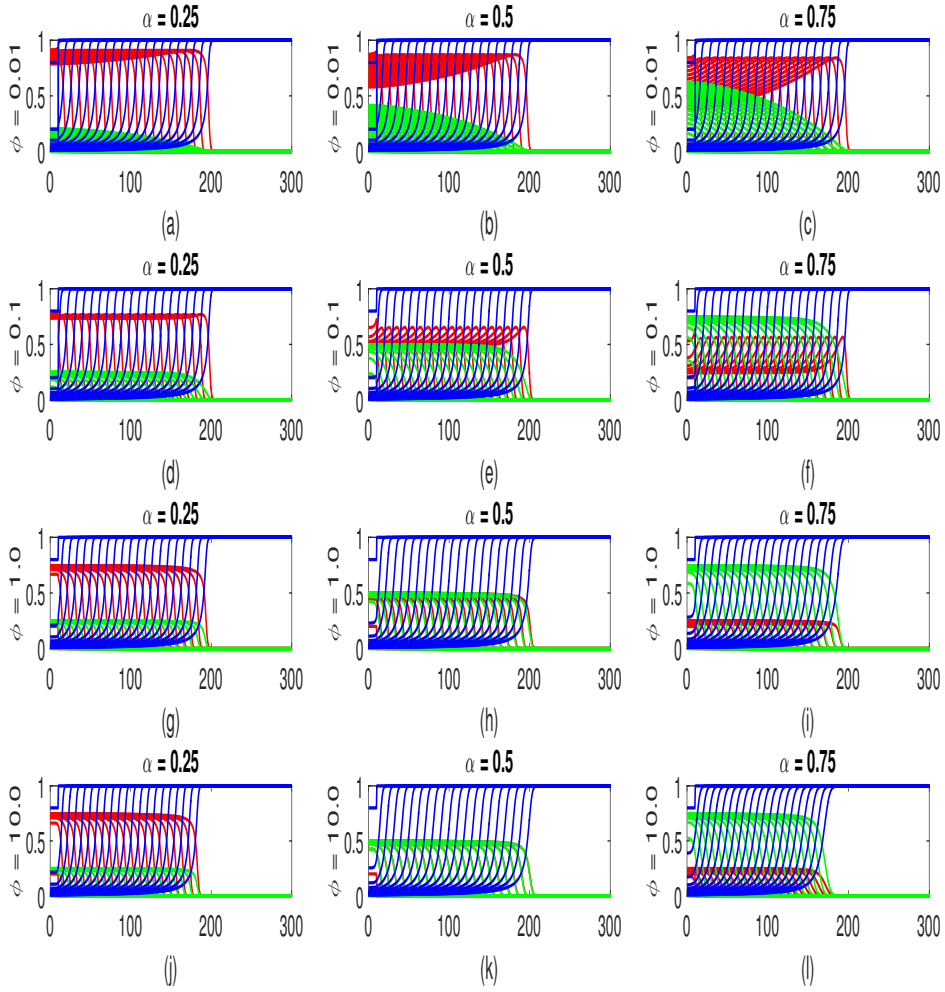

Figure 3.16: Simulations of model (3.6) with initial condition (3.4) and boundary condition (3.5) for different values of α, ϕ and fixed $a_1 = 1.0, a_2 = 0.5$ and $b = 2$. We plot normal (blue), mutant proliferating (red) and mutant migrating (green) populations as functions of time and space. (a) $\phi = 0.01, \alpha = 0.25$. (b) $\phi = 0.01, \alpha = 0.5$. (c) $\phi = 0.01, \alpha = 0.75$. (d) $\phi = 0.1, \alpha = 0.25$. (e) $\phi = 0.1, \alpha = 0.5$. (f) $\phi = 0.1, \alpha = 0.75$.(g) $\phi = 1.0, \alpha = 0.25$. (h) $\phi = 1.0, \alpha = 0.5$.(i) $\phi = 1.0, \alpha = 0.75$.(j) $\phi = 1.0, \alpha = 0.25$. (k) $\phi = 1.0, \alpha = 0.5$.(l) $\phi = 1.0, \alpha = 0.75$. The numerical method was as in Figure 3.14.

3.4.2 Travelling wave analysis

To perform a travelling wave analysis on equations (3.6) we make the standard travelling wave ansatz and look for solutions of the form:

$$N(z) = n(x,t), \quad P(z) = p(x,t), \quad M(z) = m(x,t), \qquad z = x - ct.$$

If solutions of above form exist, they represent travelling waves that move to the right with wavespeed c. Substituting the above into equations (3.6) and introducing the new variable $W = M'$ gives a system of first order ordinary differential equations as follows:

$$\begin{aligned} N' &= \frac{-1}{c}[N(1 - N - a_1(P + M)); \\ P' &= \frac{-1}{c}[bP(1 - (P + M) - a_2 N) - \phi\alpha P + \phi(1 - \alpha)M]; \\ M' &= W; \\ W' &= -cW - \phi\alpha P + \phi(1 - \alpha)M. \end{aligned} \tag{3.14}$$

In the above the "prime" denotes differentiation with respect to z. An analysis of the above equations requires the study of a four-dimensional phase space. The steady states (N^*, P^*, M^*, W^*) are:

1. $(0,0,0,0)$. (trivial)
2. $(1,0,0,0)$. (healthy tissue)
3. $(0, 1-\alpha, \alpha, 0)$. (fully-mutated tissue)
4. $\left(\frac{1-a_1}{1-a_1a_2}, (1-\alpha)\frac{1-a_2}{1-a_1a_2}, \alpha\frac{1-a_2}{1-a_1a_2}, 0\right)$. (partially-mutated tissue)

In the context of the relevant initial conditions, where we consider a perturbation of the healthy tissue via the introduction of a small and spatially restricted population of mutant cells, we can identify two relevant forms for travelling wave solution (see Figure 3.17):

1. a wave connecting the healthy steady state $(1,0,0,0)$ and the fully-mutated steady state $(0, 1-\alpha, \alpha, 0)$;

2. a wave connecting the healthy steady state $(1, 0, 0, 0)$ to the partially-mutated steady state $\left(\frac{1-a_1}{1-a_1a_2}, (1-\alpha)\frac{1-a_2}{1-a_1a_2}, \alpha\frac{1-a_2}{1-a_1a_2}, 0\right)$.

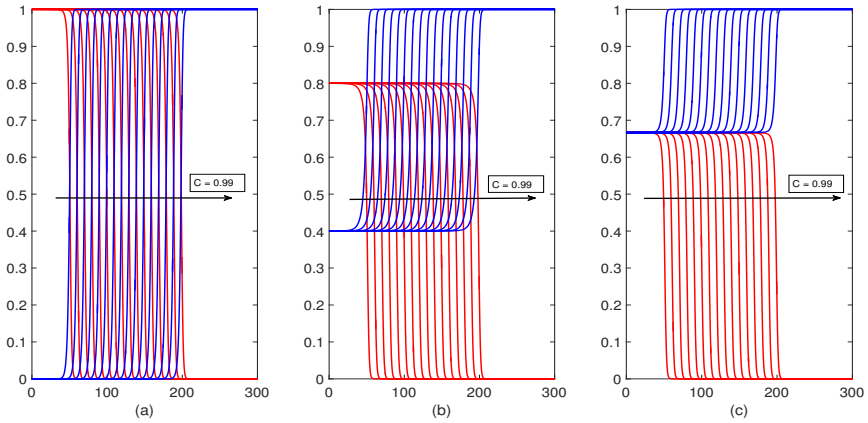

Figure 3.17: Simulations of model (3.6) with initial conditions (3.4). We plot normal (blue) and tumour cells (red) as functions of time and space with fixed $\alpha = 0.5, \phi = 0.1, a_2 = 0.5$ and $b = 2$. (a) $a_1 = 1.5$. (b) $a_1 = 0.75$. (c) $a_1 = 0.25$. The numerical method was as in Figure 3.14.

3.4.2.1 Waves connecting healthy tissue to fully mutated tissue

We start by considering travelling wave solutions that connect $(1, 0, 0, 0)$ and $(0, 1-\alpha, \alpha, 0)$, taking z to be the infinite line and applying boundary conditions:

$$N(-\infty) = 0, \quad P(-\infty) + M(-\infty) = 1, \quad W(-\infty) = 0$$

$$N(\infty) = 1, \quad P(\infty) = 0, \quad M(\infty) = 0, \quad W(\infty) = 0.$$

By analogy with the analysis of travelling wave equations for Fisher's equation, we linearise the system (3.14) ahead of the wavefront (i.e. about the steady state of healthy cells $(1, 0, 0, 0)$) and determine the nature of the eigenvalues λ of the

subsequent stability matrix, i.e. the solutions of

$$\begin{vmatrix} \frac{1}{c}-\lambda & \frac{a_1}{c} & \frac{a_1}{c} & 0 \\ 0 & \frac{-1}{c}(b(1-a_2)-\phi\alpha)-\lambda & \frac{-\phi(1-\alpha)}{c} & 0 \\ 0 & 0 & -\lambda & 1 \\ 0 & -\phi\alpha & \phi(1-\alpha) & -c-\lambda \end{vmatrix} = 0.$$

Hence,

$$\lambda_1 = \frac{1}{c},$$

and

$$\lambda^3 + (\frac{1}{c}(b(1-a_2)-\phi\alpha)+c)\lambda^2 + (b(1-a_2)-\phi)\lambda - \frac{1}{c}b(1-a_2)\phi(1-\alpha) = 0. \quad (3.15)$$

To guarantee the wavefront solutions approach the steady state in non-oscillatory manner (and hence allow for positivity of the variables), the roots of the characteristic polynomial must be real. While λ_1 is clearly real, determining the nature of $\lambda_{2,3,4}$ requires the roots of a cubic polynomial to be determined: analytical expressions do exist, yet they are typically algebraically too complex to be of much help.

We shall therefore resort to a numerical approach in order to gauge the minimum wave speed, and evaluate how it depends on the various model parameters. Specifically, we fix all model parameters except one and, as we discretely step across a range for the free parameter, we numerically determine the value of c above which equation (3.15) has only real eigenvalues. Figure 3.18 shows the result of this process as we vary the competition rate of normal cells a_2: for each a_2, we step through c and define $Im_\lambda = 1$ if equation (3.15) has imaginary eigenvalues and zero otherwise. The critical value of c above which there are solely real eigenvalues is subsequently proposed as our minimum wavespeed. A subsequent plot of this value compared against numerically calculated wavespeeds suggests that this method does indeed provide a good prediction of the wavespeed, see Figure 3.23 (a). Our studies for the other parameters yield a similar match, and are shown for a_1 in Figure 3.19, b in Figure 3.20, for ϕ in Figure 3.21, and for α in Figure 3.22.

Figures 3.23 and 3.24 summarise the full results from the above analysis, showing the relationship between the predicted wavespeed and each parameter, while others remain fixed. Figure 3.23 (a) shows the wave speed variation with a_2: we observe a steadily decreasing wave speed as a_2 increases, such that it decreases to zero if $a_2 \leq 1$: here the system moves into the stability region for the healthy tissue steady state and waves of tumour invasion are not expected. In stark contrast, altering the competition parameter for tumour cells on normal cells a_1 has no effect on the speed of tumour: no matter how strong the tumour competition is on normal cells, the tumour will stay at the same level of speed invasion as long as the competition rate of normal cells is less than 1, see Figure 3.23(b). Increasing the rate of proliferation of tumour cells, however, increases the tumour wave speed, Figure 3.23(c). Clearly, higher proliferation leads to higher numbers of tumour cells, both proliferating and migrating, and hence higher rates of invasion.

In Figure 3.24 we turn our attention to the rate and probability of switching between proliferative and migratory phenotypes. The probability of switching to the migratory tumour cell type (α) also has an impact on the speed of tumour. For $\alpha \neq 0, 1$ tumour wave speeds slightly increase as α increases towards an equal probability of switching into one of the two phenotypes, and thereafter the wave speed starts decreasing. In other words, the maximum speed of the tumour occurs when $\alpha \approx 0.5$. Figure 3.24 shows that, unsurprisingly, the lowest speed of the tumour occurs when no cells switch into migratory type ($\alpha = 0.0$) or when proliferating cells become fixed into migrating type ($\alpha = 1.0$). In these cases, respectively either no migration types place or proliferation becomes negligible and hence waves do not form.

We increase the proliferating rate of the tumour with respect to normal cells, parameter b, in Figure 3.25(a) as well as the switching rate ϕ in Figure 3.25(b). In both cases the highest wave speeds occur when $\alpha = 0.5$. However, when b is small we observe a drop in the speed, with the most aggressive behaviour of the tumour occurring when the switching rate ϕ is small.

One of the most important parameters in the model is the competitive rate of

normal cells on tumour cells, parameter a_2. In Figure 3.26 we plot the wave speed of tumour for α vs a_2, where $a_1 = 1.0, b = 2$ and $\phi = 0.1$. We observe a decrease of the wave speed as the competition rate from normal cells increases. This means that if the normal cells can produce a strong inhibition of growth, tumour aggressiveness can be significantly reduced.

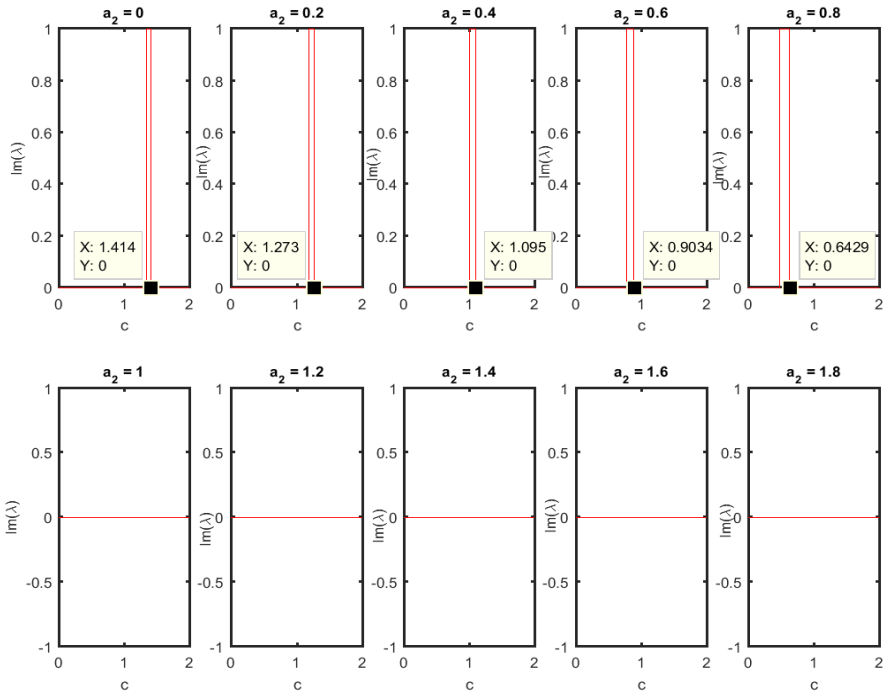

Figure 3.18: Plot showing the hybrid analytical-simulation method to determine the wave speed of tumour invasion. Each column shows the changing nature of eigenvalues as the speed c is shifted for a_2 and other parameters fixed. We take the minimum wave speed as the smallest c above which no further complex eigenvalues are found that highlighted in yellow. $a_1 = 1.0, b = 2.0, \phi = 0.1, \alpha = 0.5$.

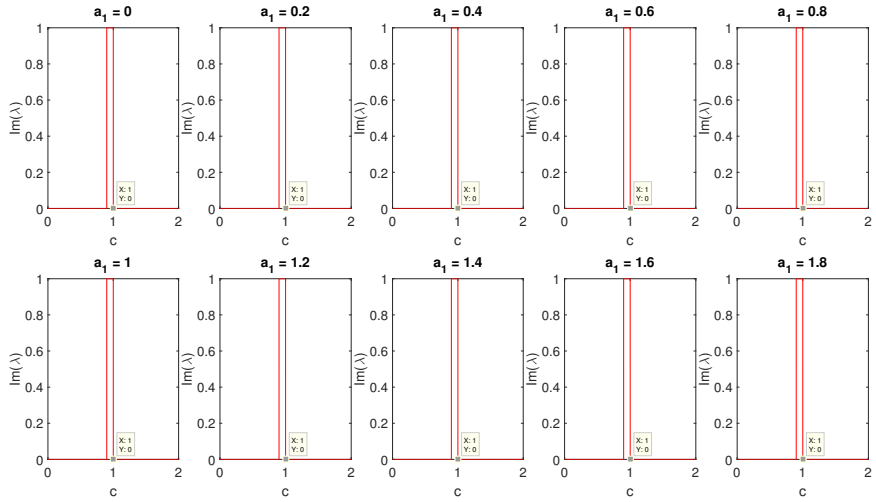

Figure 3.19: Plot showing the hybrid analytical-simulation method to determine the wave speed of tumour invasion. Each column shows the changing nature of eigenvalues as the speed c is shifted for a_1 and other parameters fixed as $a_2 = 0.5, b = 2.0, \phi = 0.1, \alpha = 0.5$. The numerical method was as in Figure 3.18.

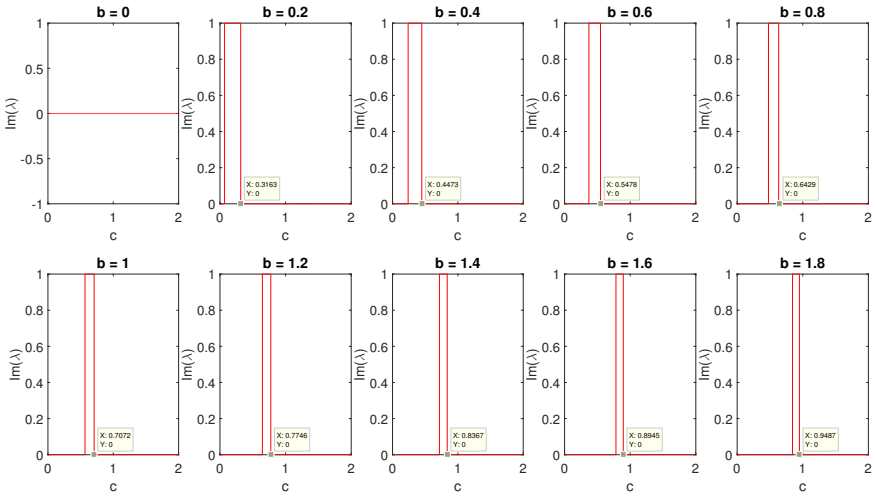

Figure 3.20: Plot showing the hybrid analytical-simulation method to determine the wave speed of tumour invasion. Each column shows the changing nature of eigenvalues as the speed c is shifted for b and other parameters fixed as $a_1 = 1.0, a_2 = 0.5, \phi = 0.1, \alpha = 0.5$.The numerical method was as in Figure 3.18.

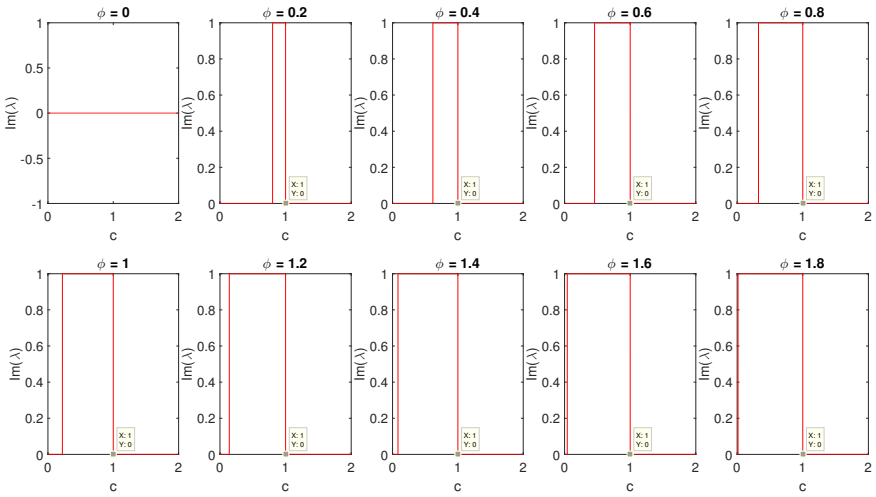

Figure 3.21: Plot showing the hybrid analytical-simulation method to determine the wave speed of tumour invasion. Each column shows the changing nature of eigenvalues as the speed c is shifted for ϕ and other parameters fixed as $a_1 = 1.0, b = 2.0, a_2 = 0.5, \alpha = 0.5$. The numerical method was as in Figure 3.18.

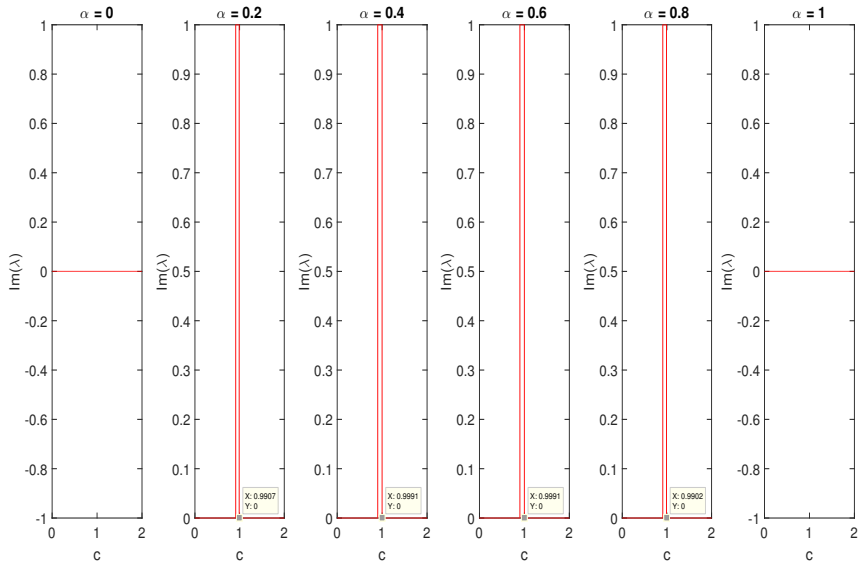

Figure 3.22: Plot showing the hybrid analytical-simulation method to determine the wave speed of tumour invasion. Each column shows the changing nature of eigenvalues as the speed c is shifted for α and other parameters fixed as $a_1 = 1.0, b = 2.0, \phi = 0.1, a_2 = 0.5$. The numerical method was as in Figure 3.18.

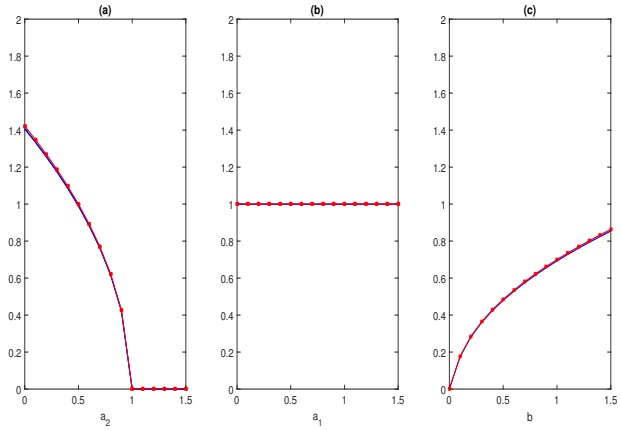

Figure 3.23: Plot of the analytical (red) and simulated (blue) average wave speed for three different values of model parameters; a_1, a_2 and b and other parameters fixed as (a) $a_1 = 1.0, b = 2.0, \phi = 0.1, \alpha = 0.5$. (b) $a_2 = 0.5, b = 2.0, \phi = 0.1, \alpha = 0.5$. (c) $a_1 = 1.0, a_2 = 0.5, \phi = 0.1, \alpha = 0.5$. The numerical method was as in Figure 3.14.

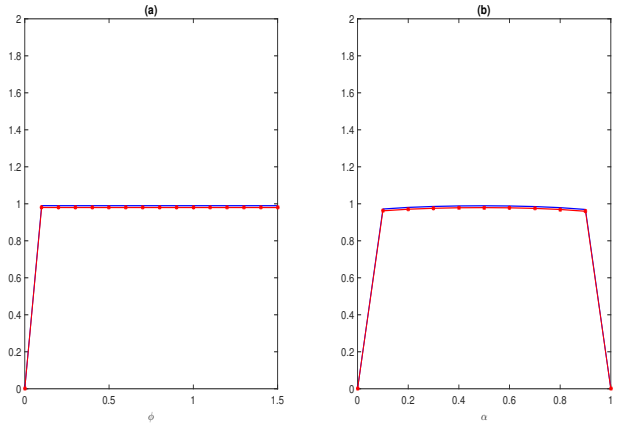

Figure 3.24: Plot of the analytical (red) and simulated (blue) average wave speed for three different values of model parameters; ϕ and α and other parameters fixed as (a) $a_1 = 1.0, a_2 = 0.5, b = 2.0, \alpha = 0.5$.(b) $a_1 = 1.0, a_2 = 0.5, b = 2.0, \phi = 0.1$. The numerical method was as in Figure 3.14.

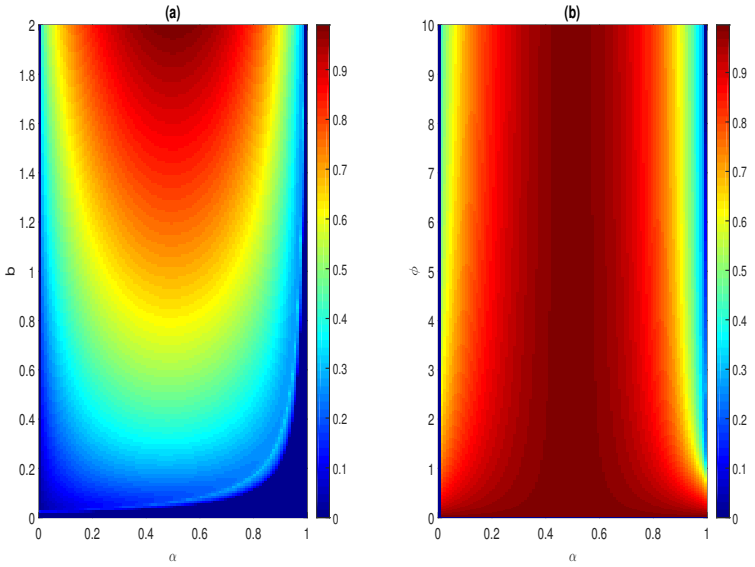

Figure 3.25: Plot of the simulated tumour wave speed; (a) α vs b and other parameters fixed as $a_1 = 1.0, a_2 = 0.5, \phi = 0.1$. (b) α vs ϕ and other parameters fixed as $a_1 = 1.0, a_2 = 0.5, b = 2$. The numerical method was as in Figure 3.14.

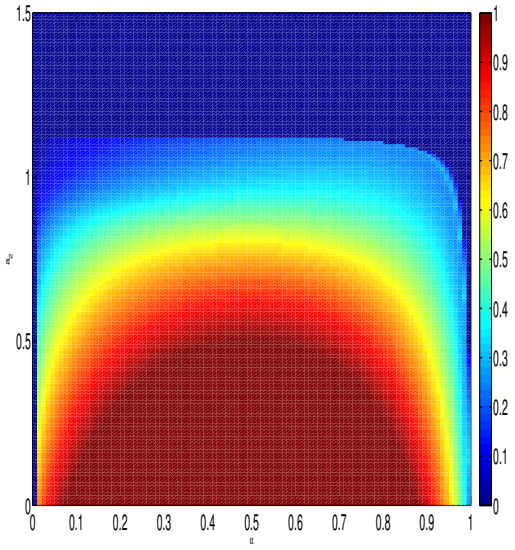

Figure 3.26: Plot of the simulating tumour wave speed for α vs a_2 and other parameters fixed as $a_1 = 1.0, b = 2$ and $\phi = 0.1$. The numerical method was as in Figure 3.14.

3.4.3 Travelling waves under density-dependent switching

We next investigate travelling wave-type invasion under the density-dependent switching function form studied earlier, i.e.

$$\alpha(S) = \begin{cases} \frac{1-\gamma}{2} & \text{if } S < k_1 \\ \frac{1}{k_2-k_1}\left(\gamma S + \frac{k_2-k_1-\gamma(k_1+k_2)}{2}\right) & \text{if } k_1 \leq S \leq k_2 \\ \frac{1+\gamma}{2} & \text{if } S > k_2 \end{cases} . \tag{3.16}$$

We plot the normal (blue) proliferating tumour (red) and migrating (green) (Figures 3.27, 3.28, 3.29) populations as functions of space and time. We choose different values of γ to describe decreasing ($\gamma = -1.0$,$\gamma = -0.5$), increasing ($\gamma = 0.5$, $\gamma = 1.0$) and constant ($\gamma = 0.0$) density dependent switching functions. When ϕ is small the waves of proliferating cells dominate over the migrating cells regardless of the form of gradient switch into migratory phenotype. For larger values of ϕ, however, the proliferating tumour waves are smaller than the migrating tumour waves for negative gradients, and higher when the gradient is positive. This suggests that the precise form of dependence of density-dependent switching can impact on the composition of the various phenotypic populations.

In Figure 3.30 we plot the wave speed under different gradients of the switching function and at different values of ϕ. We see the maximum of the wave speed occurs when the gradient is zero, i.e. when the switch to migratory phenotype is constant with density (and hence $\alpha = 0.5$). Increasing ϕ results in a more notable difference in the wave speed for different gradients. For greater detail we plot the gradient of the switch function γ against ϕ and b in Figure 3.31. We observe that the wave speed increases when b is increased, but there is a bimodal distribution with γ, with the highest wave speeds located at $\gamma = 0.0$. Therefore, density dependent switching forms act to lower the wave speed of invasion. Also increasing the competitive rate of normal cells on tumour cells can decrease the invasion of tumour (see Figure 3.32).

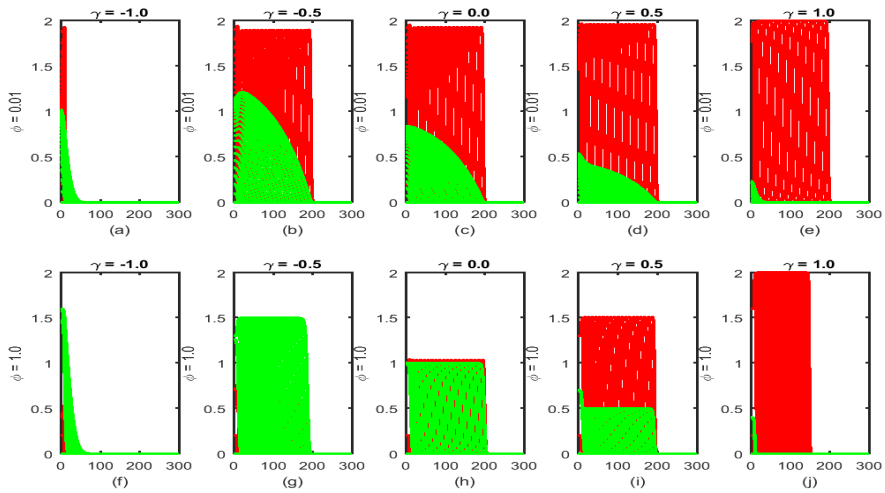

Figure 3.27: Plot of proliferating tumour (red) and migrating tumour (green) populations for different sets of parameters ϕ and γ. First row $\phi = 0.01$, second row $\phi = 1.0$. (a) and (f) $\gamma = -1.0$; (b) and (g) $\gamma = -0.5$; (c) and (h) $\gamma = 0.0$; (d) and (i) $\gamma = 0.5$; (e) and (j) $\gamma = 1.0$. Other parameters fixed as $a_1 = 1.0, a_2 = 0.5, b = 2$. The numerical method was as in Figure 3.14.

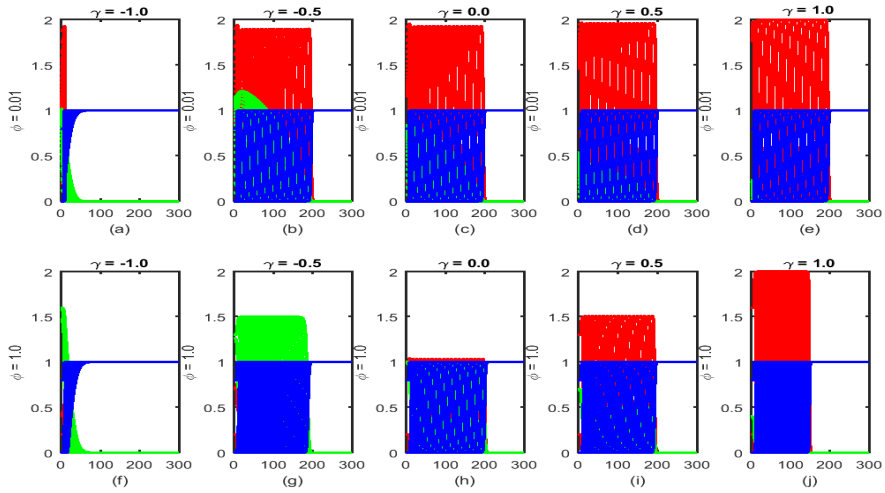

Figure 3.28: Plot of the normal (blue), proliferating tumour (red) and migrating tumour (green) populations for different sets of parameters ϕ and γ. First row $\phi = 0.01$, second row $\phi = 1.0$ (a) and (f) $\gamma = -1.0$; (b) and (g) $\gamma = -0.5$; (c) and (h) $\gamma = 0.0$; (d) and (i) $\gamma = 0.5$; (e) and (j) $\gamma = 1.0$. Other parameters fixed as $a_1 = 1.0, a_2 = 0.5, b = 2$. The numerical method was as in Figure 3.14.

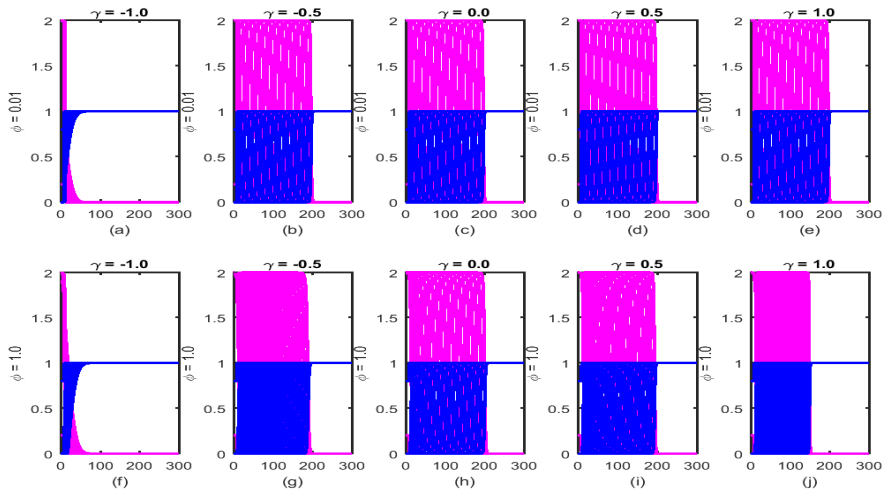

Figure 3.29: Plot of the normal (blue) and total tumour cell (magenta) population for different sets of parameters ϕ and γ. First row $\phi = 0.01$, second row $\phi = 1.0$.(a) and (f) $\gamma = -1.0$; (b) and (g) $\gamma = -0.5$; (c) and (h) $\gamma = 0.0$; (d) and (i) $\gamma = 0.5$; (e) and (j) $\gamma = 1.0$. Other parameters fixed as $a_1 = 1.0, a_2 = 0.5, b = 2$. The numerical method was as in Figure 3.14.

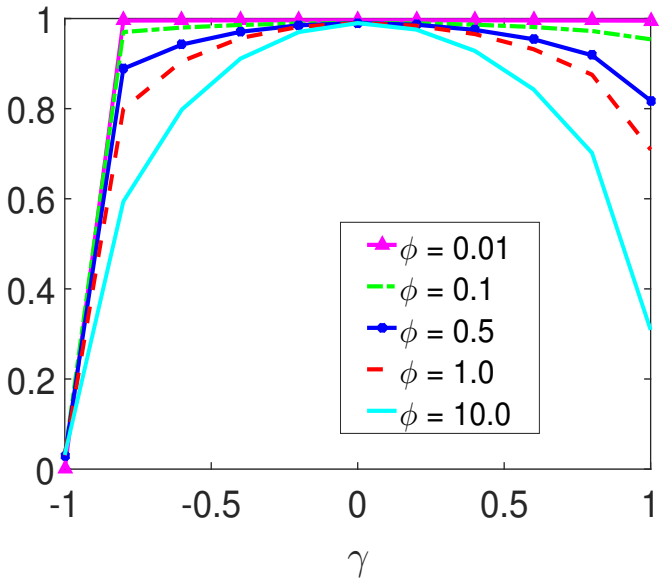

Figure 3.30: Plot of the tumour wave speed for different values of γ and ϕ and other parameters fixed as $a_1 = 1.0, a_2 = 0.5, b = 2$. The numerical method was as in Figure 3.14.

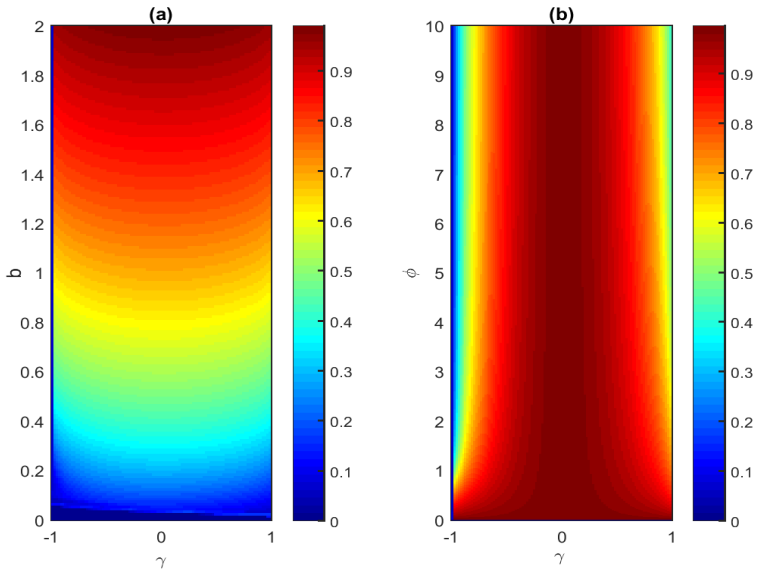

Figure 3.31: Plot of the tumour wave speed (a) γ vs b and other parameters fixed as $a_1 = 1.0$, $\phi = 0.1$. (b) γ vs ϕ and other parameters fixed as $a_1 = 1.0$ and $b = 2$. The numerical method was as in Figure 3.14.

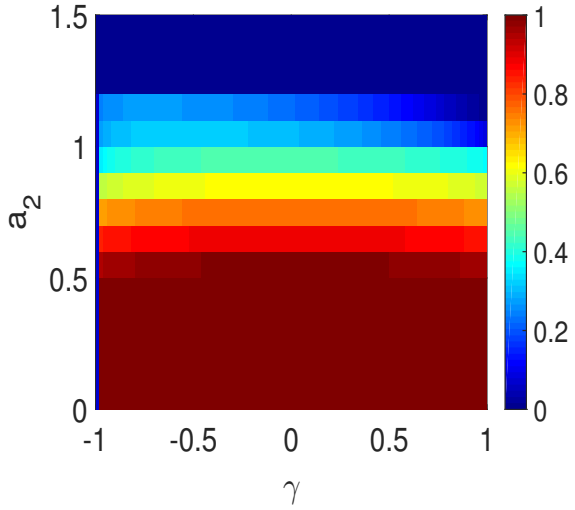

Figure 3.32: Plot of the tumour wave speed for γ vs a_2 and other parameters fixed as $a_1 = 1.0, b = 2.0, \phi = 0.1$. The numerical method was as in Figure 3.14.

3.5 Summary

We have expanded a simple go-or-grow model to include competitive interactions with normal cells. Our primary analysis showed that the stability of normal cells is guaranteed when the competition rate on tumour cells satisfies $a_2 > 1$. Under

constant α the minimum time for tumour cells to exceed the normal cells increases with the size of α. For density dependent switch forms, $\alpha(S^*)$, the lowest time for the tumour to exceed the normal cells occurs when α increases with the total number of cells S^*. On the other hand, a longer time is required when α decreases with the total number of cells S^*. The wave speed of invasion is maximised when the number of proliferating and migrating cells type is approximately equal, i.e when $\alpha \approx 0.5$. The competitive rate of normal cells on tumour cells a_2 has a significant role in reducing the aggressiveness of tumour. Similar to the previous chapter, we find that in the extended model the competition parameter of normal cells a_2 is the critical factor in reducing the number of tumour cells, while the competition parameter of tumour cells on normal cell a_1 has no effect on the speed of travelling waves of tumour cells. Furthermore, increasing the competition parameter of tumour cells on normal cell a_1 increases the number of proliferating tumour cells when γ is positive and decreases the number of proliferating cells when γ is negative. Increasing the proliferating ratio b results in a reduced time for cancerous tissue to emerge and an increase in the speed of tumour invasion. Our model emphasises the importance of normal cell parameters on tumour invasion. Nevertheless, the model has not considered the heterogeneity of brain tissue: since it is believed that the diffusion coefficient for glioma cells in the white matter is five times larger than that in grey matter [19, 115]. Moreover, observations suggest a tendency of glioma cells to infiltrate through both extracellular matrix as well as along oriented/linear structures of the brain, including the white matter tracts comprised of bundles of neuronal axons and blood vessel capillaries [42, 122, 11]. Therefore, in the next chapter we will propose a simple model methodology that allows us to explore the impact of different tissue environments.

Chapter 4

Multi-step jump models for movement

In this chapter we derive multi-jump-length random walk models for movement in response to multiple control species. Instead of allowing fixed jump lengths, we allow particles to perform distinct lengths of jump according to the environment information. We use scaling to obtain the corresponding PDE according to different hypotheses for movement based on local and nonlocal sensing strategies. Numerical simulations show the convergence between the stochastic and PDE forms for the strictly local model, albeit under certain caveats. We then investigate different strategies of movement with respect to some resource, and investigate which strategy would allow a population to most efficiently search out the best resources in the enviroment. Finally, we use the strictly local model to describe the movement of gliomas in heterogeneous brain tissue. The simulation outcomes suggest that brain tissue with a high density of axons can accelerate invasion, in correlation with other modelling studies.

4.1 Introduction

Many living objects have an ability to move through their environment in response to external stimuli. The environment itself will play a significant role in determining exactly what type of movement occurs. Motile cells in the skin, such as fibroblasts,

typically extend cellular protrusions that interact and pull on the surrounding extracellular environment, allowing the cell to propel itself forward [95, 69, 56, 78]. Under the presence of a strong directional signal, such as an extracellular gradient of some chemoattractant, the cell becomes polarised with a clear front and back, and movement can subsequently occur in a particular direction with a strong persistence: such long range directed movements allow cells to be summoned from distant regions, for example in the response during wound healing [75, 22]. As we will describe later, invasive glioma cells are capable of infiltrating along different substrates, ranging from extracellular matrix fibres [11, 56] to oriented structures such as blood vessel capillaries [27, 101, 80] and the long bundles of neuronal axons that characterise the white matter [8, 45, 10]. Consequently, these different routes for invasion can lead to a complex network of motorways, A-roads and B-roads which, when coupled to the great heterogeneity occurring across the brain, can give rise to a highly complex pattern of invasion.

At an organism level animals will also perform highly complex movements patterns according to their environment. Movement is inevitably an energetically demanding operation, and the potential benefits of making a movement must clearly be weighed against the effort expended. The characteristic searching patterns of insects such as bees and butterflies provides a case in point: an individual will typically move from flower to flower in a local patch, searching for suitable nutrient resources before flying away to a more distant patch and repeating the behaviour. Similar behaviours are observed by larger animals at much larger scales, with animals potentially performing continent scale migrations in search of suitable feeding grounds. Various recent datasets have shown that organism movements are often combined into localised random movements within the surrounding neighbourhood along with long-distance dispersal. This dispersal process is often referred to as "stratified diffusion" [54, 6].

All of the above examples reveal distinct forms of movement, from relatively short range movements to much longer leaps, where the form of movement taken is very much dependent on the environment in which the individual is moving. The question

we will address in this chapter will centre on how to derive appropriate continuous descriptions to characterise these movements. The derivation of macroscopic models to describe cellular or organism movement has typically followed two approaches. In a macroscopic phenomenological approach, a model (typically a continuous PDE) is proposed based on phenomenological reasoning. Based on principles of conservation of mass, a conservation equation is described in which movement is described at a continuous level via the population flux see Section 2.3.2 of Chapter 2 and the modelling question is centred on how to choose the flux. The other approach is to start with a random walk description for an individual's movement, and subsequently use scaling techniques to derive a continuous model under an appropriate limit, for example see [23].

A common and relatively straightforward example of the random walk based approach is to consider the continuous-time, discrete-space Master equation that results from an underlying space-jump random walk process [85]: i.e. one in which the individual makes instantaneous jumps in its position with some transition rate, which could depend on the nature of the environment in which it lies. A simple example of this process is shown in Section 2.3.3 of Chapter 2: in that example, it was shown how scaling a random walk in which individuals make jumps on a 1D lattice of a single fixed length in a manner that is constant in both space and time leads to the straightforward diffusion equation with constant diffusion coefficient.

Generalisations of this approach include the seminal work of Othmer and Stevens [111], who derived various classes of partial differential equations according to the local movement response of a random walker on a discrete lattice to the concentration of some modulating "control species" representing an environmental signal (e.g. a chemical). Significantly, subtle differences in the local sampling of the control species by the individual, for example whether the individual was only sampling at its current site or performing a comparison between the amount of substance at its site and some neighbouring site, could lead to significantly different equations in the continuous limit. In other words, the precise form of the local sampling can result in a significant impact on the macroscopic behaviour. Extensions of this work have

been performed for various others, for example Painter and Othmer started from the same master equation but under the assumption that the transition rate now depends on multiple signals [87], while Painter and Sherratt used a similar approach but in the context of multiple moving populations [89]. For a review of further extensions along this line, we refer to [23].

A limitation of these and many other similar models is that the individual is typically restricted to fixed length jumps: e.g. the individual remains on a fixed, discrete lattice and makes fixed-length jumps between adjacent sites. As such, there are clear limitations of this approach when it comes to describing the variable movement length paths exhibited by many cells and organisms and described above. An alternative formulation to the random walk description is the Levy walk, named after the French mathematician Paul Levy. In the Levy walk, the random walk combines frequent smaller steps, analogous to classical Brownian motion, with occasional longer trajectories. The Levy walk hence has the ability to generate faster diffusion than that dictated by Brownian diffusion [65, 129]. Levy walks have been found to provide a good description to capture the foraging characteristics of many animals: for example, studies of open-ocean predatory fish (sharks, tuna, billfish and ocean sunfish) suggest that some individuals switch between Levy and Brownian type motion to adapt their optimal movement to different environmental resource distributions [57]. A study of nature of human mobility showed that human walks have statistically similar features perceived in Levy walks [94]. For more details on the modelling of combined short and long distance dispersals, see [104, 67, 83, 70].

Summarising, individuals ranging from single cells to animals and humans perform various movements, from short range to long range according to their needs and the environment. Long-range movements will clearly be energetically demanding, yet could be crucial as a means of locating some region with greater nutrient resources. In the specific context of glioma growth, determining the extent to which invading cells perform localised movements or longer range movements along oriented structures (such as capillaries) or axons will clearly be important for assessing the manner and rate at which a tumour invades.

In this chapter we will develop a framework for incorporating movements of different lengths into a random walk model, and subsequently investigate the macroscopic model that is obtained in the continuous model. In particular, we will incorporate a dependence of the type of jump made according to a local control species, representing the local environment. We take the standard approach of postulating a continuous time, discrete space random walk for movement on a fixed lattice, but extend to allow for jumps of more than one grid step. An early example of such an approach has been considered by Aronson [7], who examined the scaling from discrete to continuous partial differential equations for individuals performing jumps of different lengths on a one-dimensional lattice: we extend this to consider how the resulting equation changes according to the way in which the individual samples the local environment: for example, whether the individual can only sense its immediate environment (i.e. the site on which it is sitting), or whether it can also somehow sense the information at the potential site of relocation. Following this derivation, we will subsequently show a theoretical application of the framework to understand whether undertaking distinct jump responses according to the information provided by the environment will allow a population to more efficiently locate and consume the resources available in their environment. Finally, we will take the modelling back to glioma invasion, by assessing the extent to which different tissue compositions will impact on the rate of invasion of a glioma.

4.2 Modeling multi-step jump response to multiple signals

We begin with a biased random walk to describe the movement of a "particle" (e.g. a cell) in response to some external (environmental) cue, on a one-dimensional lattice of spacing h. We define $p_x(t)$ to be the probability of a particle to be at node $x \in Z$ at time t, conditioned on starting at node $x = 0$ at $t = 0$. We assume a particle can perform multiple jumps of steps $i = 1, ..., m$, corresponding to lengths $h, 2h, ..., mh$ either to sites left $(-)$ or right $(+)$, according to some *transitional*

probability per unit time: thus, $\tau_x^{\pm i}$ define the transitional probability rates that a particle at node x moves to node $x \pm i$. To incorporate dependence of this movement on environmental information, we assume these jump probability rates are dependent on the concentration/density levels of potentially multiple "control species" (which could be nutrients, chemical, ECM density, vasculature density etc.). Specifically we define the control species on the same one-dimensional lattice, defining the infinite matrix

$$\mathbf{u} = \begin{pmatrix} \dots & u_{x-1}^1 & u_x^1 & u_{x+1}^1 & \dots \\ \vdots & \vdots & \vdots & \vdots & \vdots \\ \dots & u_{x-1}^k & u_x^k & u_{x+1}^k & \dots \end{pmatrix}.$$

In the above, the matrix element u_x^j defines the density of the j^{th} control species at node x, and k defines the total number of control species (see [87]). To introduce dependency of the jump on these control species, we take the transitional jump probabilities to be functions of this matrix, i.e. $\tau_x^{\pm i}(\mathbf{u})$. From this underlying biased random walk, we can postulate the corresponding discrete-space, continuous time for the evolution of p_x as

$$\frac{\partial p_x}{\partial t} = \sum_{i=1}^{m} [\overbrace{\tau_{x+i}^{-i}(\mathbf{u})p_{x+i}}^{(1)} + \overbrace{\tau_{x-i}^{+i}(\mathbf{u})p_{x-i}}^{(2)} - \overbrace{\tau_x^{-i}(\mathbf{u})p_x - \tau_x^{+i}(\mathbf{u})p_x}^{(3)}]. \tag{4.1}$$

Where the first term represents jumping from $x+i$ to x, the second term represents jumping from $x-i$ to x and the third terms represent jumping from x to $x \pm i$. We note that $(\sum_{i=1}^{m} \tau_x^{\mp i}(\mathbf{u}))^{-1}$ will measure the mean waiting time at the x^{th} site. We note that we could potentially make $m = \infty$ to describe jumps that occur to any point in an infinite lattice.

4.2.1 Sensing strategies

There are a variety of potential ways in which an individual at node x could sense the local control species. We specifically consider the following sensing strategies (see Figure 4.1):

1. Strictly local;
2. Local average & Nonlocal average;
3. Local neighbour & Nonlocal neighbour;
4. Local gradient & Nonlocal gradient.

Strictly local: This implies a "myopic"walker, i.e an individual that looks only at its current site. In other words, it performs a "leap into the unknown", moving to a site of which it does not know anything.

Local average/neighbour/gradient: These imply that the individual does a small amount of sampling both locally and close by, but then may still perform a leap into the relatively unknown.

Nonlocal average/neighbour/gradient: These imply that the individual has a capacity to detect the environment both at its current site and the location where it plans on moving to. For a cell this could occur through the extension of filopodia, while for animals it could represent good vision.

We will derive the PDE models from the underlying individual based models according to the four sensing strategies above. We begin with strictly local model, where particles jump left $(-)$ or right $(+)$ according to the control species at the present site.

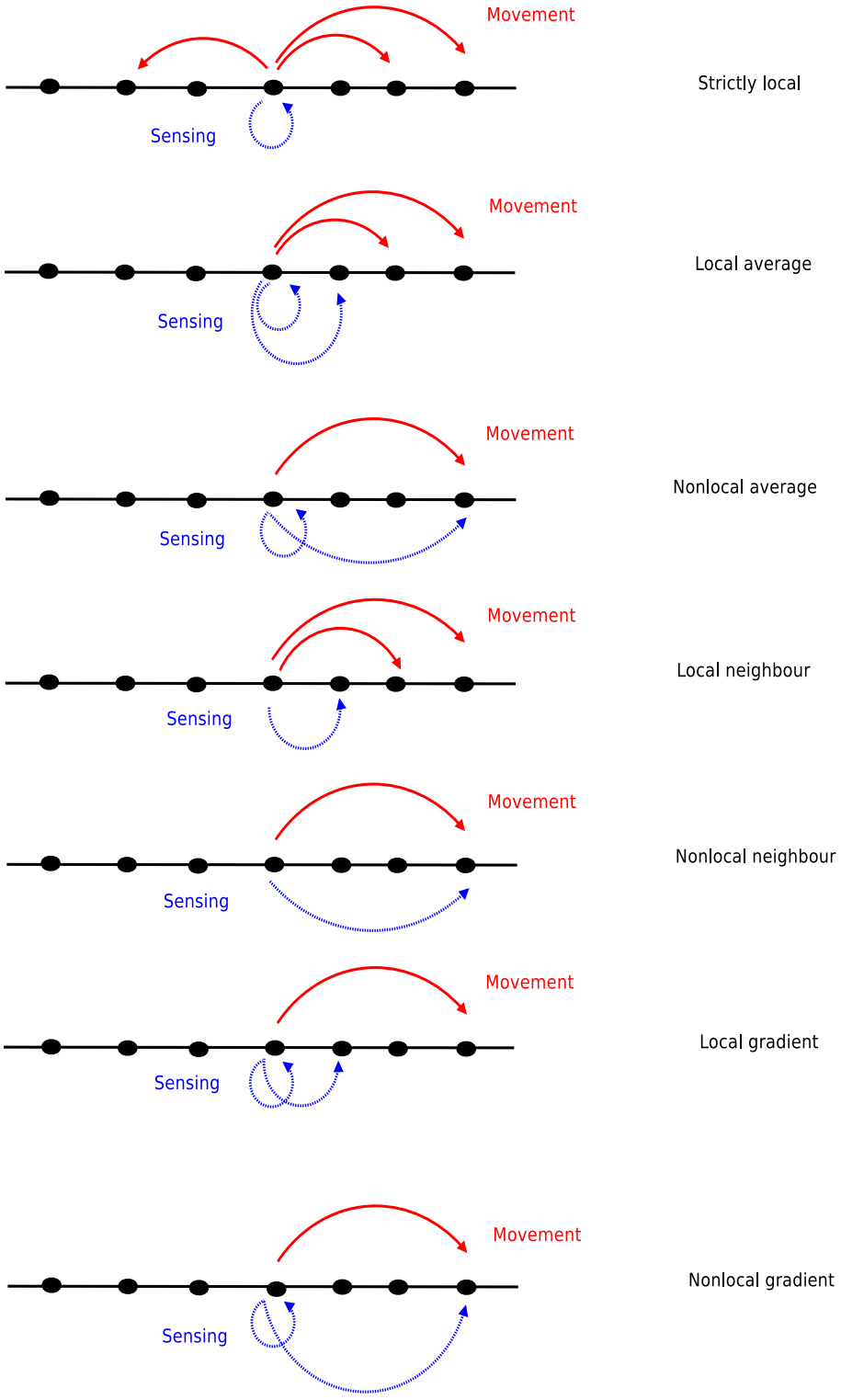

Figure 4.1: Illustration of the various sensing strategies for the movement of particles.

4.2.2 Strictly local model

In this model we assume that the probability of jumping to the $x \pm i^{th}$ node depends only on the densities $\mathbf{u}_x$ of the control species $u_1, ..., u_k$ at node x. Since the transition probabilities are independent of the lattice node and depend only on local densities $\mathbf{u}_x$, we thus have $\tau_x^{-i} = \tau_x^{+i} (\equiv \tau_x^i)$ and as a result equation (4.1) becomes

$$\frac{\partial p_x}{\partial t} = \sum_{i=1}^{m} [\tau_{x+i}^i(\mathbf{u}) p_{x+i} + \tau_{x-i}^i(\mathbf{u}) p_{x-i} - 2\tau_x^i(\mathbf{u}) p_x]. \tag{4.2}$$

We expand the right hand side as Taylor series. We reinterpret x as a continuous variable and terms of the form

$$\tau_{x\pm i}^i(\mathbf{u}) p_{x\pm i} = \tau^i(\mathbf{u}(x \pm ih, t)) p(x \pm ih, t)$$

are expanded about x to second order in ih, where h is the lattice spacing, as follows:

$$\tau^i(\mathbf{u}(x \pm ih, t)) = \tau^i(\mathbf{u}(x,t)) \pm ih \frac{\partial \tau^i(\mathbf{u}(x,t))}{\partial x} + \frac{(ih)^2}{2} \frac{\partial^2 \tau^i(\mathbf{u}(x,t))}{\partial x^2} \pm O((ih)^3);$$
$$p(x \pm ih, t) = p(x,t) \pm ih \frac{\partial p(x,t)}{\partial x} + \frac{(ih)^2}{2} \frac{\partial^2 p(x,t)}{\partial x^2} \pm O((ih)^3).$$

Substituting the above into equation (4.2), and simplifying leads to:

$$\frac{\partial p}{\partial t} = \sum_{i=1}^{m} [(ih)^2 \frac{\partial^2 \tau^i(\mathbf{u}) p}{\partial x^2} + O((ih)^4)]. \tag{4.3}$$

We assume a scaling of the transition rates $\tau^i = \lambda \tau^i$ and assume the following parabolic limit exists:

$$lim_{\substack{\lambda \longrightarrow \infty \\ h \longrightarrow 0}} \lambda h^2 = d \qquad \text{(constant)}. \tag{✦}$$

Consequently, we obtain the following equation for the continuous population distribution of a random walker executing multiple jumps of differing lengths $i = 1, ..., m$:

$$\begin{aligned}\frac{\partial p}{\partial t} &= d\sum_{i=1}^{m}[i^2\frac{\partial^2(\tau^i(\mathbf{u})p)}{\partial x^2}],\\ &= d\sum_{i=1}^{m}[i^2\frac{\partial}{\partial x}(\tau^i(\mathbf{u})\frac{\partial p}{\partial x}+p\frac{\partial \tau^i}{\partial \mathbf{u}}.\frac{\partial \mathbf{u}}{\partial x})].\end{aligned} \tag{4.4}$$

We note that the second line shows the expansion into a diffusive and advective/ taxis type component: we discuss this in more detail later in this chapter.

4.2.3 Local average & Nonlocal average models

The local and nonlocal average models are based on the assumption that transition rates depend on the average information between the current node and that in the direction of the target site. As described earlier, for a cell this could occur through the sampling of the environment in its surroundings via a filopodial extension.

4.2.3.1 Local average model

In this formulation the jump of a particle at node x to node $x \pm i$ depends on the averaged information of the control species between the current and nearest neighbour in the direction of the target node:

$$\tau_x^{+i}(\mathbf{u}) = \boldsymbol{\tau}^i(\frac{1}{2}(\mathbf{u}_x + \mathbf{u}_{x+1})); \qquad \tau_x^{-i}(\mathbf{u}) = \boldsymbol{\tau}^i(\frac{1}{2}(\mathbf{u}_x + \mathbf{u}_{x-1})).$$

We apply the same process as previously (see Appendix B.1.1 for more details): we substitute the above into equation (4.1), expand through a Taylor series, simplify and assume the parabolic scaling (✦). This yields the PDE:

$$\begin{aligned}\frac{\partial p}{\partial t} &= d\sum_{i=1}^{m}[(i^2-i)p\frac{\partial^2\boldsymbol{\tau}^i(\mathbf{u})}{\partial x^2}+(2i^2-i)\frac{\partial \boldsymbol{\tau}^i(\mathbf{u})}{\partial x}\frac{\partial p}{\partial x}+i^2\boldsymbol{\tau}^i(\mathbf{u})\frac{\partial^2 p}{\partial x^2}],\\ &= d\sum_{i=1}^{m}[i^2\frac{\partial^2\boldsymbol{\tau}^i(\mathbf{u})p}{\partial x^2}-i\frac{\partial}{\partial x}(p\frac{\partial \boldsymbol{\tau}^i(\mathbf{u})}{\partial x})].\end{aligned} \tag{4.5}$$

4.2.3.2 Nonlocal average model

In this case the transitional probability for the jump of the particle at node x to node $x \pm i$ is taken to depend on the average information of the control species between the current and target node, as described below:

$$\tau_x^{+i}(\mathbf{u}) = \boldsymbol{\tau}^i(\frac{1}{2}(\mathbf{u}_x + \mathbf{u}_{x+i})); \qquad \tau_x^{-i}(\mathbf{u}) = \boldsymbol{\tau}^i(\frac{1}{2}(\mathbf{u}_x + \mathbf{u}_{x-i})).$$

We apply the same process as previously (see Appendix B.1.2 for more details): we substitute the above into equation (4.1), expand through a Taylor series, simplify and assume the parabolic scaling (✦). This yields the PDE:

$$\frac{\partial p}{\partial t} = d\sum_{i=1}^{m}[i^2\frac{\partial}{\partial x}(\boldsymbol{\tau}^i(\mathbf{u})\frac{\partial p}{\partial x})]. \tag{4.6}$$

4.2.4 Local neighbour & Nonlocal neighbour models

In the neighbourhood models it is assumed that the transition rates depend only on information in the direction of the target jump site. Here we assume two different types of neighbour based models:

4.2.4.1 Local neighbour model

The jump of a particle at node x to node $x \pm i$ is assumed to depend only on the control species at the nearest neighbour in the direction of the arrival point, as described below:

$$\tau_x^{+i}(\mathbf{u}) = \boldsymbol{\tau}^i(u_{x+1}); \qquad \tau_x^{-i}(\mathbf{u}) = \boldsymbol{\tau}^i(u_{x-1}).$$

We apply the same process as previously (see Appendix B.2.1 for more details): we substitute the above into equation (4.1), expand through a Taylor series, simplify

and assume the parabolic scaling (✦). This yields the PDE:

$$\begin{aligned}\frac{\partial p}{\partial t} &= d\sum_{i=1}^{m}[i^2\boldsymbol{\tau}^i(\mathbf{u})\frac{\partial^2 p}{\partial x^2} + 2(i^2-i)\frac{\partial \boldsymbol{\tau}^i}{\partial x}\frac{\partial p}{\partial x} + (i^2-2i)p\frac{\partial^2 \boldsymbol{\tau}^i}{\partial x^2}],\\ &= d\sum_{i=1}^{m}[i^2\frac{\partial^2}{\partial x^2}(\boldsymbol{\tau}^i(\mathbf{u})p) - 2i\frac{\partial}{\partial x}(p\frac{\partial \boldsymbol{\tau}^i}{\partial x})].\end{aligned} \tag{4.7}$$

4.2.4.2 Nonlocal neighbour model

For the non local neighbour model we assume the probability of a jump for a particle at node x to node $x \pm i$ depends on the control species at the arrival point $x \pm i$ as described below:

$$\tau_x^{+i}(\mathbf{u}) = \boldsymbol{\tau}^i(\mathbf{u}_{x+m}); \qquad \tau_x^{-i} = \boldsymbol{\tau}^i(\mathbf{u}_{x-m}).$$

We apply the same process as previously (see Appendix B.2.2 for more details): we substitute the above into equation (4.1), expand through a Taylor series, simplify and assume the parabolic scaling (✦). This yields the PDE:

$$\frac{\partial p}{\partial t} = d\sum_{i=1}^{m}[i^2\frac{\partial}{\partial x}(\boldsymbol{\tau}^i(\mathbf{u})\frac{\partial p}{\partial x} - p\frac{\partial \boldsymbol{\tau}^i(\mathbf{u})}{\partial x})]. \tag{4.8}$$

4.2.5 Local gradient & Nonlocal gradient models

In these models the transition rate probabilities are assumed to depend on the difference between the density of control species at the current and a node in the direction of the target. Again we split into a "local" and "nonlocal" formulation.

4.2.5.1 Local gradient model

In the local gradient model we assume the transition rates depend linearly on the difference between the density of control species at the current node and the nearest neighbor in the direction of the arrival node. For the one space dimension lattice, the transition rates are written as :

$$\tau_x^{+i} = a_i + b_i(\boldsymbol{\tau}^i(\mathbf{u}_{x+1}) - \boldsymbol{\tau}^i(\mathbf{u}_x)); \qquad \tau_x^{-i} = a_i + b_i(\boldsymbol{\tau}^i(\mathbf{u}_{x-1}) - \boldsymbol{\tau}^i(\mathbf{u}_x)).$$

In the above, $\tau : \mathbf{R}^k \to \mathbf{R}$, and $a_{1,\ldots,m} \geq 0$ and $b_{1,\ldots,m}$ are constants. We apply the same process as previously (see Appendix B.3.1 for more details): we substitute the above into equation (4.1), expand through a Taylor series, simplify and assume the parabolic scaling (✦). This yields the PDE:

$$\frac{\partial p}{\partial t} = d\sum_{i=1}^{m}[a_i i^2 \frac{\partial^2 p}{\partial x^2} - 2ib_i \frac{\partial}{\partial x}(p\frac{\partial \tau^i}{\partial x})]. \tag{4.9}$$

4.2.5.2 Nonlocal gradient model

Finally, we assume the transition rate depends on the difference between the density of the control species at the current node and the arrival node. Again taking a linear dependence gradient, we let the transtion rates at node x be given as:

$$\tau_x^{+i} = a_i + b_i(\boldsymbol{\tau}^i(\mathbf{u}_{x+m}) - \boldsymbol{\tau}^i(\mathbf{u}_x)); \qquad \tau_x^{-i} = a_i + b_i(\boldsymbol{\tau}^i(\mathbf{u}_{x-m}) - \boldsymbol{\tau}^i(\mathbf{u}_x)).$$

In the above, $\tau : \mathbf{R}^k \to \mathbf{R}$, and $a_{1,\ldots,m} \geq 0$ and $b_{1,\ldots,m}$ are constants. We apply the same process as previously (see Appendix B.3.2 for more details): we substitute the above into equation (4.1), expand through a Taylor series, simplify and assume the parabolic scaling (✦). This yields the PDE:

$$\begin{aligned}\frac{\partial p}{\partial t} &= d\sum_{i=1}^{m}[a_i i^2 \frac{\partial^2 p}{\partial x^2} - 2b_i i^2 \frac{\partial \boldsymbol{\tau}^i}{\partial x}\frac{\partial p}{\partial x} - 2b_i i^2 \frac{\partial^2 \boldsymbol{\tau}^i}{\partial x^2} p], \\ &= d\sum_{i=1}^{m}[a_i i^2 \frac{\partial^2 p}{\partial x^2} - 2b_i i^2 \frac{\partial}{\partial x}(p\frac{\partial \boldsymbol{\tau}^i}{\partial x})].\end{aligned} \tag{4.10}$$

4.2.6 Summary

To summarise the various models, we consider the case of a single control species i.e $\mathbf{u} = u$. Considering classical continuous modelling, we suppose the partial differential equation is written as

$$\frac{\partial p}{\partial t} + \nabla.\mathbf{j} = 0, \tag{4.11}$$

where $\mathbf{j}$ is the flux. In many models of biological movement, the flux is assumed to have a diffusive and tactic component as follows

$$\mathbf{j} = -\overbrace{D(u)\nabla p}^{\text{Diffusive}} + \overbrace{p\chi(u)\nabla u}^{\text{Taxis}}. \tag{4.12}$$

The diffusive flux represents diffusion of the population, potentially depending on the control species u and $D(u)$ defines the diffusion coefficient. The taxis flux represents movement of the population in response to gradients of u, where $\chi(u)$ defines chemotactic coefficient. Note that:

- $\chi(u) > 0 \Rightarrow$ movement up gradients of u and accumulation of the population at concentration peaks (positive taxis);
- $\chi(u) < 0 \Rightarrow$ movement down gradients of u and accumulation of the population at troughs of u (negative taxis).

We will consider two forms for the transitional probabilities:

- T1 : Increasing form $\tau^i(u) = \frac{\alpha_i u}{k_i + u}$;
- T2: Decreasing form $\tau^i(u) = \frac{\alpha_i k_i}{k_i + u}$.

Where $\alpha_i \in [0, \infty)$ define the maximum transition probability rates corresponding to the i^{th} jump type, while k_i are positive constants.

4.2.6.1 Strictly local model

In this case the particle flux is given by

$$\mathbf{j} = -d\sum_{i=1}^{m}[i^2(\tau^i(u)\nabla p + p\tau^{i'}(u)\nabla u)], \tag{4.13}$$

where $\tau^{i'}(u)$ is the first derivative of τ^i respect to u. This can be written as

$$\mathbf{j} = \sum_{i=1}^{m}[-di^2\tau^i(u)\nabla p + p\chi(u)\nabla u], \tag{4.14}$$

where $\chi(u) \equiv \sum_{i=1}^{m}[-di^2\tau^{i'}(u)]$ describes the taxis sensitivity. If $\tau^{i'}(u) < 0$, the taxis is positive and the flux is up the gradient of u. Whereas, the flux is down the gradient if the taxis is negative (i.e. $\tau^{i'}(u) > 0$).

- Under T1: the diffusion coefficient is $\sum_{i=1}^{m}[di^2\frac{\alpha_i u}{k_i+u}]$ and the taxis sensitivity is $\chi(u) = \sum_{i=1}^{m}[-di^2\frac{\alpha_i k_i}{(k_i+u)^2}]$. The taxis is negative, and the particle flux is down concentration gradients of u.

- Under T2: the diffusion coefficient is $\sum_{i=1}^{m}[di^2\frac{\alpha_i k_i}{k_i+u}]$ and the taxis sensitivity is $\chi(u) = \sum_{i=1}^{m}[-di^2\frac{-\alpha_i k_i}{(k_i+u)^2}]$. The taxis is positive, and the particle flux is up gradients of u, with accumulation at high concentrations of u.

4.2.6.2 Local average model

Recalling, we have

$$\frac{\partial p}{\partial t} = d\sum_{i=1}^{m}[i^2\boldsymbol{\tau}^i(\mathbf{u})\frac{\partial^2 p}{\partial x^2} + (2i^2 - i)\frac{\partial \boldsymbol{\tau}^i(\mathbf{u})}{\partial x}\frac{\partial p}{\partial x} + (i^2 - i)p\frac{\partial^2 \boldsymbol{\tau}^i(\mathbf{u})}{\partial x^2}], \tag{4.15}$$

which can be written as

$$\frac{\partial p}{\partial t} = d\sum_{i=1}^{m}[i^2\frac{\partial^2}{\partial x^2}(\boldsymbol{\tau}^i(u)p) - i\frac{\partial}{\partial x}(p\frac{\partial \tau^i}{\partial x})], \tag{4.16}$$

or

$$\frac{\partial p}{\partial t} = d\sum_{i=1}^{m}[\frac{\partial}{\partial x}(i^2\tau^i(u)\frac{\partial p}{\partial x} + (i^2 - i)p\frac{\partial \tau^i}{\partial x})]. \tag{4.17}$$

Hence, the particle flux is

$$\mathbf{j} = -d\sum_{i=1}^{m}[i^2(\tau^i(u)\nabla p + (i^2 - i)p\tau^{i'}(u)\nabla u)], \tag{4.18}$$

where $\tau^{i'}(u)$ is the first derivative of τ^i respect to u. This can be written as

$$\mathbf{j} = \sum_{i=1}^{m}[-di^2\tau^i(u)\nabla p + p\chi(u)\nabla u], \tag{4.19}$$

where $\chi(u) \equiv \sum_{i=1}^{m}[-d(i^2 - i)\tau^{i'}(u)]$ is a taxis sensitivity. If $i \neq 1$ and/or $\tau^{i'}(u) \neq 0$, the flux contains both a diffusive and tactic. In the special case where individuals

can only jump a maximum of 1 lattice node, there is no taxis of the population.

- Under T1: the diffusion coefficient is $\sum_{i=1}^{m}[di^2\frac{\alpha_i u}{k_i+u}]$ and the taxis sensitivity is $\chi(u) = \sum_{i=1}^{m}[-d(i^2-i)\frac{\alpha_i k_i}{(k_i+u)^2}]$. The taxis is negative for $i > 1$ and particles accumulate where u is small.

- Under T2: the diffusion coefficient is $\sum_{i=1}^{m}[di^2\frac{\alpha_i k_i}{k_i+u}]$ and the taxis sensitivity is $\chi(u) = \sum_{i=1}^{m}[-d(i^2-i)\frac{-\alpha_i k_i}{(k_i+u)^2}]$. The taxis is positive for $i > 1$ and particles tend to accumulate where u is high.

4.2.6.3 Nonlocal average model

Recalling, we have

$$\frac{\partial p}{\partial t} = d\sum_{i=1}^{m}[i^2\frac{\partial}{\partial x}(\boldsymbol{\tau}^i(\mathbf{u})\frac{\partial p}{\partial x}], \tag{4.20}$$

where the particle flux will be given by

$$\mathbf{j} = -d\sum_{i=1}^{m}[i^2(\tau^i(u)\nabla p)]. \tag{4.21}$$

In this case the flux consists solely of a diffusive component with coefficient

$$d\sum_{i=1}^{m}[i^2(\tau^i(u)].$$

Long term we therefore expect evolution to a uniform distribution of p, regardless of the u distribution and regardless of the length of jumps made.

4.2.6.4 Local neighbour model

Recalling, we have

$$\frac{\partial p}{\partial t} = d\sum_{i=1}^{m}[i^2\frac{\partial^2}{\partial x^2}(\boldsymbol{\tau}^i(\mathbf{u})p) - 2i\frac{\partial}{\partial x}(p\frac{\partial \boldsymbol{\tau}^i}{\partial x})]. \tag{4.22}$$

The particle flux is

$$\mathbf{j} = -d\sum_{i=1}^{m}[i^2(\tau^i(u)\nabla p + (i^2-2i)p\tau^{i'}(u)\nabla u)]. \tag{4.23}$$

In this case $\chi(u) \equiv \sum_{i=1}^{m}[-d(i^2-2i)\tau^{i'}(u)]$ is the taxis sensitivity. We note that in this case the taxis type depends on both τ and the jump length.

- Under T1: the diffusion coefficient is $\sum_{i=1}^{m}[di^2\frac{\alpha_i u}{k_i+u}]$ and the taxis sensitivity is $\chi(u) = \sum_{i=1}^{m}[-d(i^2-2i)\frac{\alpha_i k_i}{(k_i+u)^2}]$. The taxis is negative for jump lengths $i > 2$, and particles tend to move forward u is small. The taxis is positive if $i < 2$.

- Under T2: the diffusion coefficient is $\sum_{i=1}^{m}[di^2\frac{\alpha_i k_i}{k_i+u}]$ and the taxis sensitivity is $\chi(u) = \sum_{i=1}^{m}[-d(i^2-2i)\frac{-\alpha_i k_i}{(k_i+u)^2}]$. The taxis is positive if $i > 2$, and particles will move to regions where u is high.

4.2.6.5 Nonlocal neighbour model

Recalling, we have

$$\frac{\partial p}{\partial t} = d\sum_{i=1}^{m}[i^2\frac{\partial}{\partial x}(\boldsymbol{\tau}^i(\mathbf{u})\frac{\partial p}{\partial x} - p\frac{\partial \boldsymbol{\tau}^i(\mathbf{u})}{\partial x})]. \tag{4.24}$$

The particle flux is

$$\mathbf{j} = -d\sum_{i=1}^{m}[i^2(\tau^i(u)\nabla p - p\tau^{i'}(u)\nabla u)], \tag{4.25}$$

where $\tau^{i'}(u)$ is the first derivative of τ^i respect to u. Hence $\chi(u) \equiv \sum_{i=1}^{m}[di^2\tau^{i'}(u)]$ is the taxis sensitivity.

- Under T1: the diffusion coefficient is $\sum_{i=1}^{m}[di^2\frac{\alpha_i u}{k_i+u}]$ and the taxis sensitivity is $\chi(u) = \sum_{i=1}^{m}[di^2\frac{\alpha_i k_i}{(k_i+u)^2}]$. The taxis is positive, and particles accumulate at high concentrations of u.

- Under T2: the diffusion coefficient is $\sum_{i=1}^{m}[di^2\frac{\alpha_i k_i}{k_i+u}]$ and the taxis sensitivity is $\chi(u) = \sum_{i=1}^{m}[di^2\frac{-\alpha_i k_i}{(k_i+u)^2}]$. The taxis is negative, and particles accumulate at low concentrations of u.

4.2.6.6 Local gradient model

Recalling, we have

$$\frac{\partial p}{\partial t} = d\sum_{i=1}^{m}[i^2 a_i \frac{\partial^2 p}{\partial x^2} - 2ib_i \frac{\partial}{\partial x}(p\frac{\partial \tau^i}{\partial x})]. \tag{4.26}$$

The particle flux in this case is

$$\mathbf{j} = -d\sum_{i=1}^{m}[i^2 a_i \nabla p - 2ib_i p\tau^{i'}(u)\nabla u)], \tag{4.27}$$

where $\tau^{i'}(u)$ is the first derivative of τ^i respect to u and $\chi(u) \equiv \sum_{i=1}^{m}[2dib_i\tau^{i'}(u)]$ is a taxis sensitivity.

- Under T1: the diffusion coefficient is $\sum_{i=1}^{m}[a_i di^2 \frac{\alpha_i u}{k_i+u}]$ and the taxis sensitivity is $\chi(u) = \sum_{i=1}^{m}[2dib_i \frac{\alpha_i k_i}{(k_i+u)^2}]$. The taxis is positive, and particles accumulate at high concentrations of u.

- Under T2: the diffusion coefficient is $\sum_{i=1}^{m}[di^2 \frac{\alpha_i k_i}{k_i+u}]$ and the taxis sensitivity is $\chi(u) = \sum_{i=1}^{m}[2dib_i \frac{-\alpha_i k_i}{(k_i+u)^2}]$. The taxis is negative, and particles accumulate at low concentrations of u.

4.2.6.7 Nonlocal gradient model

Recalling, we have

$$\frac{\partial p}{\partial t} = d\sum_{i=1}^{m}[a_i i^2 \frac{\partial^2 p}{\partial x^2} - 2b_i i^2 \frac{\partial}{\partial x}(p\frac{\partial \boldsymbol{\tau}^i}{\partial x})]. \tag{4.28}$$

The particle flux is

$$\mathbf{j} = -d\sum_{i=1}^{m}[i^2 a_i \nabla p - 2i^2 b_i p\tau^{i'}(u)\nabla u)], \tag{4.29}$$

where $\tau^{i'}(u)$ is the first derivative of τ^i respect to u and $\chi(u) \equiv \sum_{i=1}^{m}[2di^2 b_i\tau^{i'}(u)]$ is the taxis sensitivity.

- Under T1: the diffusion coefficient is $\sum_{i=1}^{m}[a_i di^2 \frac{\alpha_i u}{k_i+u}]$ and the taxis sensitivity

is $\chi(u) = \sum_{i=1}^{m}[2di^2 b_i \frac{\alpha_i k_i}{(k_i+u)^2}]$. The taxis is positive, and particles accumulate at high concentrations of u.

- Under T2: the diffusion coefficient is $\sum_{i=1}^{m}[a_i di^2 \frac{\alpha_i k_i}{k_i+u}]$ and the taxis sensitivity is $\chi(u) = \sum_{i=1}^{m}[2di^2 b_i \frac{-\alpha_i k_i}{(k_i+u)^2}]$. The taxis is negative, and particles accumulate where u is low.

We summarize the results of the above section in Table 4.1. Clearly, we see sensitive dependence on the form of model: for the same form of τ, population fluxes can be directed up or down gradients of u according to the form of sensing and the length of the jump.

Table 4.1: Sensing strategies in diffusion/taxis forms

Model	Diffusion coefficient	Taxis coefficient	Under T1	Under T2
Strictly local	$d\sum_{i=1}^{m}[i^2(\tau^i(u)]$	$\sum_{i=1}^{m}[-di^2\tau^{i'}(u)]$	-ve taxis	+ve taxis
Local average	$d\sum_{i=1}^{m}[i^2(\tau^i(u)]$	$\sum_{i=1}^{m}[-d(i^2-i)\tau^{i'}(u)]$	-ve taxis if $i>1$	+ve taxis if $i>1$
Non local average	$d\sum_{i=1}^{m}[i^2(\tau^i(u)]$	None	-	-
Local neighbour	$d\sum_{i=1}^{m}[i^2(\tau^i(u)]$	$\sum_{i=1}^{m}[-d(i^2-2i)\tau^{i'}(u)]$	-ve taxis if $i>2$	+ve taxis if $i>2$
Non local neighbour	$d\sum_{i=1}^{m}[i^2(\tau^i(u)]$	$\sum_{i=1}^{m}[di^2\tau^{i'}(u)]$	+ve taxis	-ve taxis
Local gradient	$d\sum_{i=1}^{m}[i^2 a_i(\tau^i(u)]$	$\sum_{i=1}^{m}[2dib_i\tau^{i'}(u)]$	+ve taxis	-ve taxis
Non local gradient	$d\sum_{i=1}^{m}[i^2 a_i(\tau^i(u)]$	$\sum_{i=1}^{m}[2di^2 b_i\tau^{i'}(u)]$	+ve taxis	-ve taxis

It is again clarified that we could potentially allow $m \to \infty$ to describe jumps that can occur to any other point in an infinitely long lattice: for example, the probability of jumping to some other site could, theoretically, be described by some jump probability distribution with positive probability rates for all jump lengths i, such as an exponentially decreasing function of the jump length ($\tau^i \equiv \exp^{-\alpha i}$ for some constant α). Of course, in such instances it is not immediately apparent whether the chosen parabolic limit would be appropriate as $h \to 0$: we would have to control carefully in each case whether it is appropriate or not.

In the context of animal or cell movement, however, it is perhaps unlikely to allow potentially infinite length jumps: movement distances are likely to be capped according to the natural limits of movement and hence we would expect the proba-

bilities to be effectively zero above some jump length i: hence, m would be finite in size and would be an indication of the maximum range of movement of an individual in a particular jump. In this case, the probabilities of performing a particular movement will become zero above some fixed value of m.

4.3 Verification of the strictly local PDE

Before we move to a specific study, we first verify whether simulations of the stochastic model quantitatively match with the derived PDE. The advantage of the latter lies in that it allows us to more efficiently study higher densities of particles for longer times, as well as providing a more analytically tractable form. Note that we will restrict our analysis for the rest of this chapter to the case of random movement based on strictly local information (i.e. equation (4.4)):

$$\frac{\partial p}{\partial t} = d\sum_{i=1}^{m}[i^2\frac{\partial^2(\tau^i(\mathbf{u})p)}{\partial x^2}]. \tag{4.30}$$

For simplicity, and to focus in this section on how the model works, we assume the transition probabilities are independent of the control species:

$$\tau^i(\mathbf{u}) = \alpha_i \qquad \forall i = 1, ..., m.$$

In the case of one step jumps of length h (i.e. $m = 1$) we simply have:

$$\frac{\partial p}{\partial t} = d\alpha_1\frac{\partial^2 p}{\partial x^2}. \tag{4.31}$$

We furnish the above with zero flux boundary conditions, therefore assuming that individuals do not jump outside the domain. Initially we consider a Dirac delta type function initial condition, assuming the particles are initially distributed in a concentrated mass and that the control species is uniformly distributed on the domain. We take an arbitrary value of $\alpha_1 = 1.0$. To solve the stochastic random walk model we use Gillespie's algorithm [46]: for more details of simulating stochastic diffusion processes using Gillespie's algorithm see [29]. We plot and compare the

stochastic random walk model and the derived PDE in Figure 4.3 at different times $t = [0, 10, 50, 80, 100]$, increasing the number of particles $N = [10, 10^3, 10^5]$ in each row. In the bottom row we plot the L_1-norm of the distance error between the stochastic simulations and the PDE at different times. When the number of particles is small ($N = 10$) and $t > 0$, the PDE only provides a crude approximation of the stochastic solution. However, for a large numbers of particles ($N = 10^5$), the stochastic solution is almost identical to the PDE and the error tends to zero.

For single jumps but of length $3h$, again solved subject to zero flux boundary conditions and a spike initial condition for the particles, simulations in Figure 4.4 show the error between the stochastic and PDE model is higher than the case where the particles perform just one jump per unit time, while increasing the numbers of particles has limited impact on the convergence between the models. The reason for this, however, does not lie in the failure of the PDE to approximate the stochastic model, but the artificial case of a single spike and only allowing fixed length jumps: particles are restricted to specific grid points and consequently the discrepancy is high, see Figure 4.2. Choosing much smoother initial conditions reduces the artificial nature of this scenario, and shows a much better match (Figure 4.5). Summarising, the PDE provides a good match to stochastic model, assuming "reasonable" initial conditions.

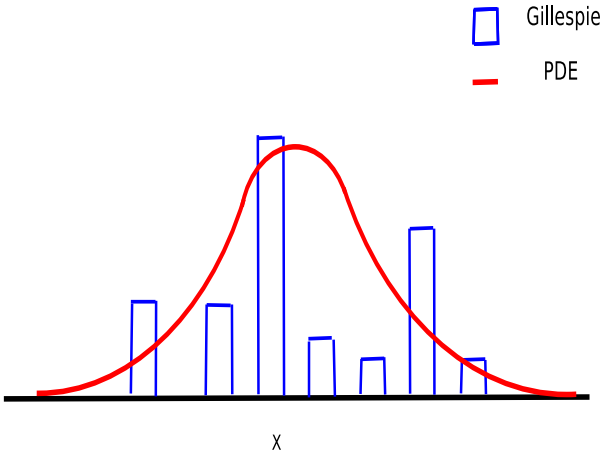

Figure 4.2: Sketch of Gillespie and PDE approximation of the numerical solution.

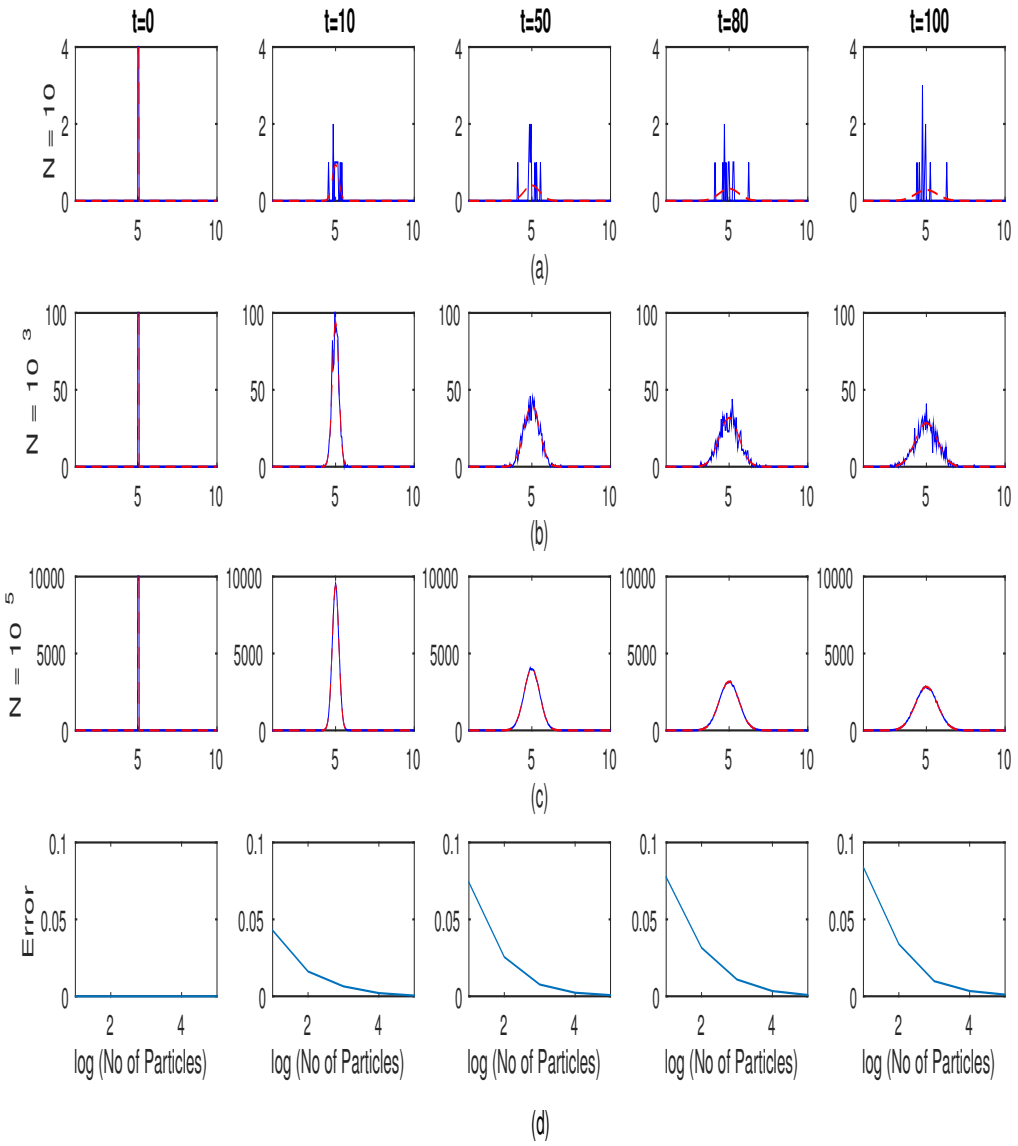

Figure 4.3: Simulations of the stochastic random walk model (blue line) and the derived PDE equation (4.31) (red line), with zero flux boundary conditions and a Dirac delta type initial condition of the particles. (a) Number of particles = 10, (b) Number of particles = 10^3, (c) Number of particles = 10^5, (d) The L_1-norm distance error between the stochastic simulations and the PDE at different times from left $t = [0, 10, 50, 80, 100]$. In these simulations $d = 0.0025$. The stochastic simulations are solved by Gillespie's algorithm [46] while the PDE model is solved through a method of lines approach in which the PDE is first discretised via a standard central difference scheme, and the subsequent ODEs solved using the "$ode15s$" solver in Matlab with a relative tolerance = 10^{-7}, absolute tolerance = 10^{-7} and grid spacing of $h = 0.05$.

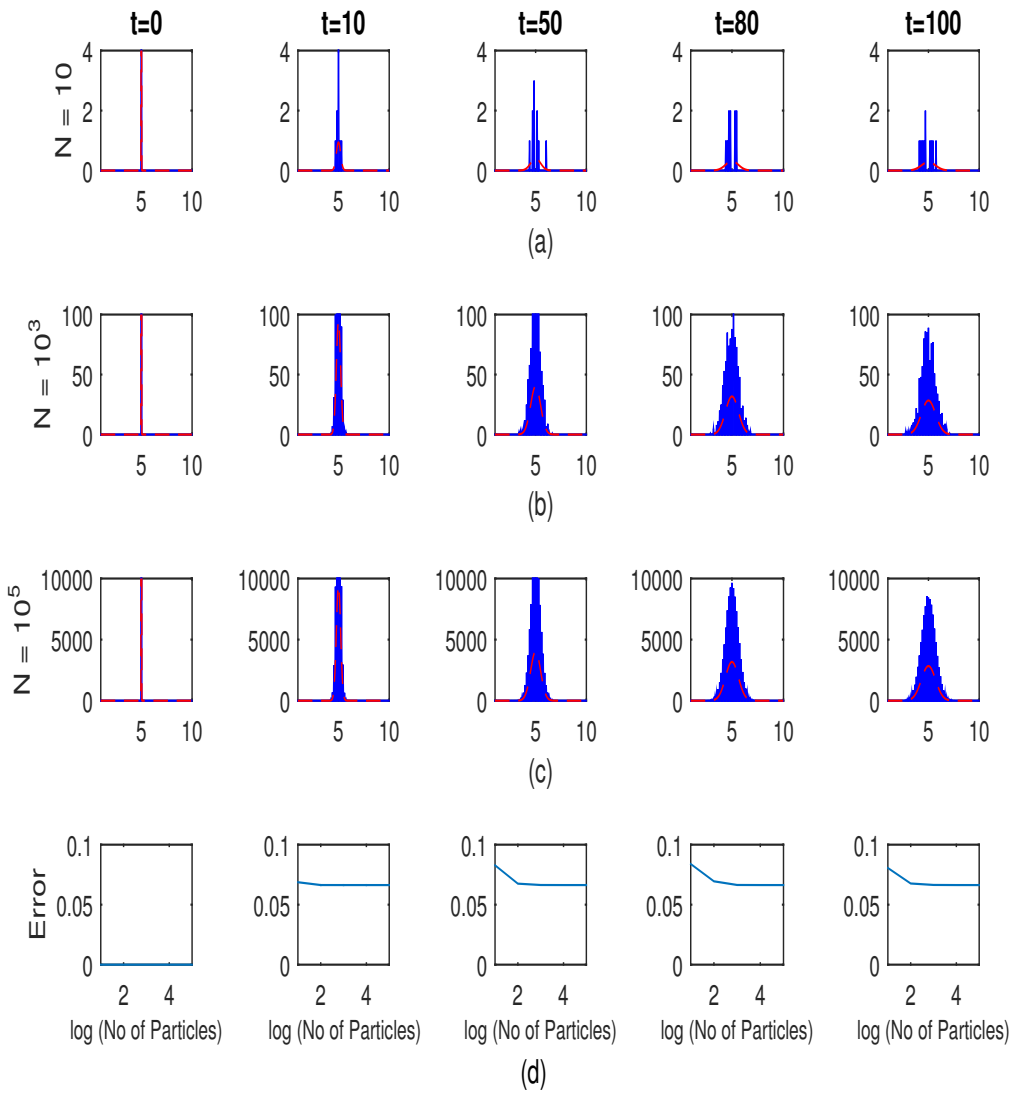

Figure 4.4: Simulations of the stochastic random walk model (blue line) and the derived PDE equation (4.4) (red line) with a Dirac delta type initial condition and step jumps of length $3h$. Numerical method as in Figure 4.3.

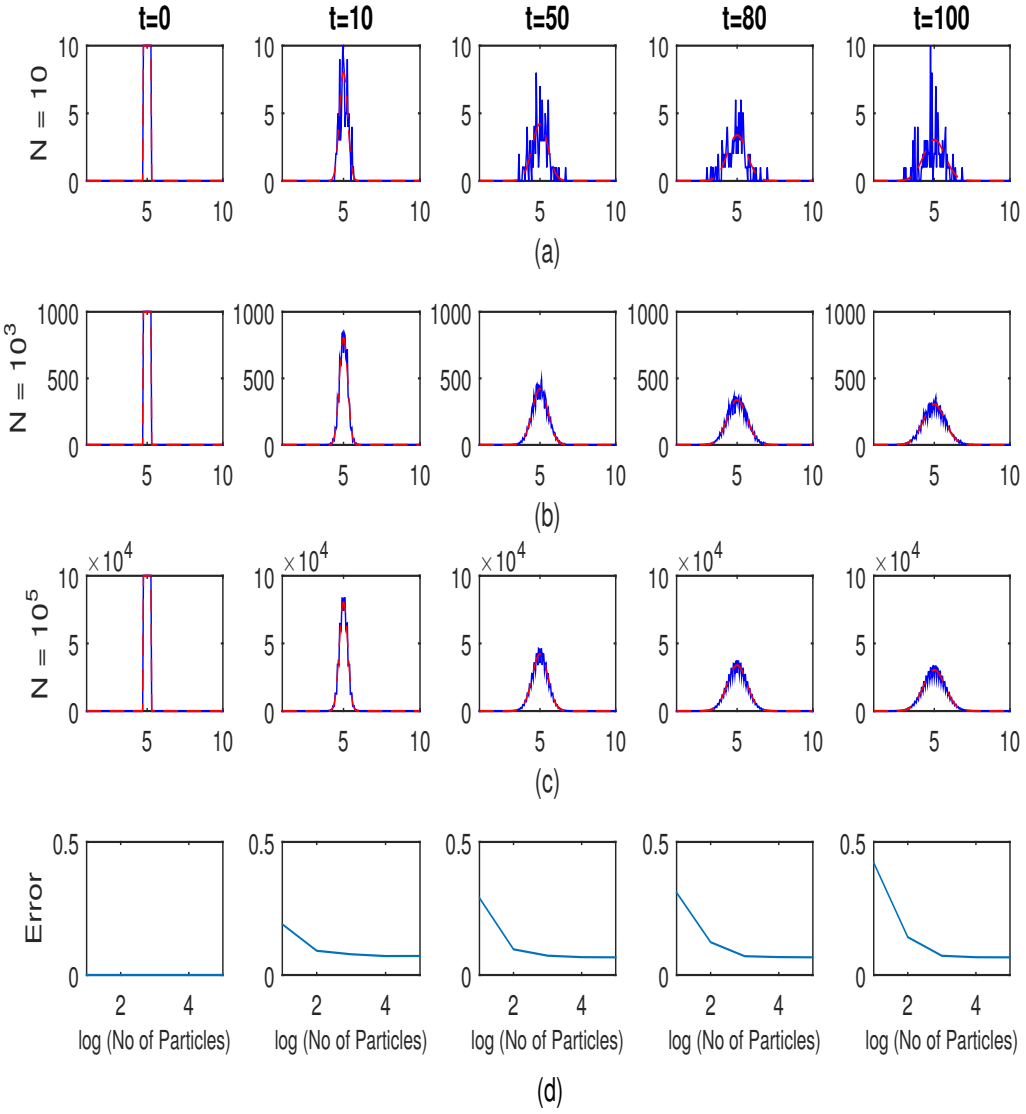

Figure 4.5: Simulations of the stochastic random walk model (blue line) and the derived PDE equation (4.4) (red line) with step function initial condition and step jumps of length $3h$. Numerical method as in Figure 4.3.

4.4 Efficient strategies for resource localisation

4.4.1 Motivation

In this section we will consider a theoretical application of our modelling to determine how making different decisions according to the environment can allow a population to optimally position itself within it. Our application could apply to a population of cancer cells that aims to seek the most nutrient rich region for its spatial growth, but is perhaps more intuitively described within the context of some animal species. As our prototype example we will consider a population of insects such as butterflies, bees or ladybirds distributed across some region of space, such as a field. The insects can decide either to perform relatively short range movements, e.g. flitting between flowers in a patch to find suitable nectar, or can undertake an (energetically demanding) longer range movement to a more distant region, potentially finding a better resource. We therefore consider as our principle variables (1) our motile population (e.g. bees) and (2) our resource (e.g. nectar). Our population will be allowed to perform two types of movement, short and long range, and will base that decision on the local nectar available. For succinctness we will restrict our focus to the strictly local model, effectively assuming our individuals are myopic and cannot see longer distances. In our first study we assume the resource is not consumed (i.e. it is in abundance, and minimally reduced by the population) while in the second study we allow for consumption of the nutrient resource. After setting up the model and defining suitable measures, our principal question will be as follows: what is the most efficient strategy of jumping to maximise the benefit from the environment?

4.4.2 Model set up

We denote our population by $p(x,t)$ and our resource by $u(x,t)$. Assuming our population makes multi-step jumps according to strictly local information, we have

$$\frac{\partial p}{\partial t} = d\sum_{i=1}^{m}[i^2\frac{\partial^2(\tau^i(u)p)}{\partial x^2}]. \tag{4.32}$$

For our two variables we assume a variety of distributions, concentrated such that they have the same average level, i.e $\int_0^L p(x,0) = \int_0^L u(x,0) = L$.

4.4.2.1 Initial distribution of particles

- Uniform: i.e we assume a homogeneous distribution $p(x,0) = 1$.
- Aggregated: we consider the particles to be initially localised as a Gaussian distribution, $p(x,0) = \frac{L}{\sigma_p\sqrt{2\pi}} \exp(-\frac{(x-\mu_p)^2}{2\sigma_p^2})$ where σ_p is the standard deviation and μ_p is the mean position of the aggregate.

4.4.2.2 Initial distribution of resource

- Uniform: we assume the resource to be initially homogeneously distributed across space $u(x,0) = 1$.
- Aggregated: we consider the resource to be initially localised as a Gaussian distribution, $u(x,0) = \frac{L}{\sigma_u\sqrt{2\pi}} \exp(-\frac{(x-\mu_u)^2}{2\sigma_u^2})$ where σ_u is the standard deviation and μ_u is the mean position of the aggregate.
- Randomised heterogeneous: We also choose a special case (Case*) of a random non-homogeneous function to describe the initial condition of the resource as example: we define our function by a sum of a random number of up to 20 Gaussian functions, each of which has a random mean position, height and steepness as below:

$$u(x,0) = NF \sum_{i=1}^{n} h_i \exp(-\sigma_i * (x - \mu_i)^2), \tag{4.33}$$

Where NF is a normalising factor, n is an integer random number uniformly distributed between 1 & 20, h_i, σ_i and μ_i are randomly chosen. We explain this choice in more detail later. Note that all the initial conditions are normalised to ensure the average initial density = 1.

4.4.2.3 Jump responses with respect to the resource

Our investigation will focus on how making different movement types (e.g. short or long) in response to the resource impacts on how efficiently our population explores its environment. To investigate this we assume the transition probability rate function takes three different forms with respect to the resource: a constant, an increasing or a decreasing function as shown in Figure 4.6.

1. Constant jump response. This response takes no account of the resource: jumps take place at a constant rate regardless of the resource distribution, i.e

$$\tau^i(u) = \alpha_i. \qquad (*)$$

2. Decreasing jump response. In this case the population performs jumps of a particular length at a faster rate when the amount of resource is low and at a lower rate when the amount of resource is high. Specifically, we take:

$$\tau^i(u) = \frac{2\alpha_i u^*}{u^* + u}, \qquad (**)$$

   where $2\alpha_i$ defines the maximum jump rate and u^* is taken to be the average density of resource, i.e $u^* = 1$.

3. Increasing jump response. In this case the population performs jumps of a particular length at a faster rate when the amount of resource is high and at a lower rate when the amount of resource is low. Specifically, we take:

$$\tau^i(u) = \frac{2\alpha_i u}{u^* + u}, \qquad (***)$$

   where $2\alpha_i$ defines the maximum jump rate and u^* is taken to be the average density of resource, i.e $u^* = 1$.

Note that for the above three forms (*), (**), (***), the value of $\tau^i(u)$ is the same when $u = u^* = 1$.

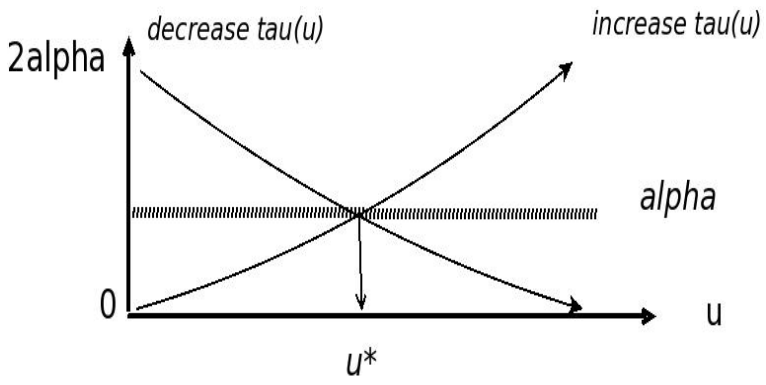

Figure 4.6: Sketch of the three forms of transition rate.

4.4.2.4 Benefit and cost measurements

In order to properly assess which searching strategy is best, we must consider appropriate measures for the benefits gained and costs accrued. For searching for food, benefits would clearly correspond to the amount of food the population encounters, while costs would relate to the effort expended looking for it. Thus, we define the cost and benefit as follows.

- Benefit is an estimate of how much resource (food) the particles contact over time. Specifically, we define the benefit as:

$$Benefit = \int_0^T \int_0^L p(x,t)u(x,t)\,dx\,dt. \tag{4.34}$$

- The cost relates to the effort expended over time. We assume this is subdivided into a movement-based and residual component as follows:

$$Cost = Cost_j + Cost_r. \tag{4.35}$$

  The movement-based cost depends on both the rate of jumps and the length of the jump taken: frequent long jumps would require much more energy than infrequent short jumps. Thus, we define the jump cost as

$$Cost_j = \int_0^T \int_0^L \sum_{i=1}^{m} p(x,t)\tau^i(\mathbf{u})ih\,dx\,dt.$$

  Where ih is the jump length. We also assume there is a residual cost associated

with simply existing, which we take to be small compared to the above,

$$Cost_r = \int_0^T \epsilon \, dt.$$

Note ϵ is taken to be 10% of the cost of a one-step jump.

- Benefit-Cost Ratio we take the ratio of the above benefits and costs to evaluate the optimal jump strategy. The benefit-cost ratio is simply

$$BCR = Benefit/Cost.$$

4.4.3 Initial distribution arrangements

According to the earlier proposed initial distribution, we consider the following arrangements for the initial distribution of the particles and the resource:

- Case 0 (Reference case): In this case the resource and particles are homogeneously distributed $u(x, 0) = p(x, 0) = 1$ (see Figure 4.7). We define this as our reference case as it will generate the same BCR for all choices of jump strategy, as we show in the next section.

- Case I: In this case, the resource is uniformly distributed across the field, whereas the distribution of the particles is localised at the centre of the domain (Figure 4.8 (a))).

- Case II: In this case the resource and particles are co-localised and centered on the domain (Figure 4.8 (b)).

- Case III: In this case the population and resource are both localised, but with distributions centered at different points (Figure 4.8 (c))).

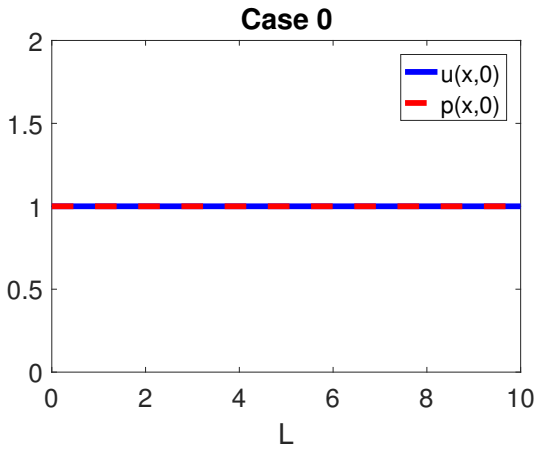

Figure 4.7: Illustration of initial distribution of resource (blue line), and particles (red dashed) for Case 0.

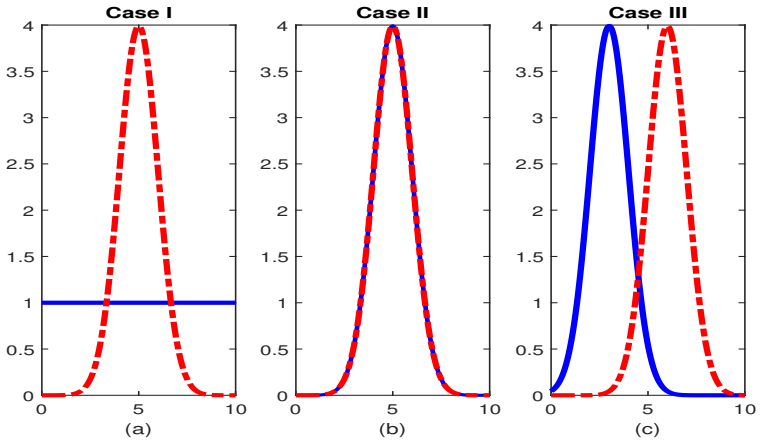

Figure 4.8: Illustration of initial distribution of resource (blue line), and particles (red dashed) for the three cases I-III. (a) $\mu_p = 5$ and $\sigma_p = 1.0$, (b) $\mu_{p,u} = 5$ and $\sigma_{p,u} = 1.0$, (c) $\mu_u = 3$, $\mu_p = 6$, $\sigma_{p,u} = 1.0$.

4.4.4 Results

In this section we analyse the effectiveness of different jump strategies. We allow our population to either:

1. perform a single short jump of length h ($i = 1$);
2. perform a single long jump of length $10h$ ($i = 10$);
3. perform both a short (length h, $i = 1$) or long (length $10h$, $i = 10$) jump.

For each scenario above we examine the impact of each of the transition rate functions (*),(**) or (***). Note that for the short jump case we set $\alpha_1 = \alpha_s = 0.5$, while for the long jump we set $\alpha_{10} = \alpha_l = \alpha_s/10 = 0.05$. When both jumps are performed we set $\alpha_1 = \alpha_s/2$ and $\alpha_{10} = \alpha_l/2$. We have $\alpha_i = 0$ for all $i \neq 1$ or 10. We note that these values for the $\alpha's$ are chosen to ensure that the cost of jumping is the same for all jump strategies when the resource is set at its average level, i.e. when $u = 1$. For all simulations we set $h = 0.05$

4.4.4.1 Constant transition rates

Reference case (Case 0): In this case both particles and resource remain uniformly distributed and we can directly calculate the cost and benefit of the three jump strategies (short, long, both). Using formulae (4.34) and (4.35) we find that for short, long and both jumps we have

$$Benefit = LT$$

$$Cost = \alpha_i ihLT + \varepsilon T$$

and consequently

$$BCR = \frac{L}{\alpha_i ihL + \varepsilon}$$

Under constant transition jump rates we plot the log-scale of the benefit-cost ratio in Figure 4.9 for the three cases of initial distribution for the particles and the resource above. Case I generates the same results as the reference case, since the resource is homogeneously distributed on the domain and the BCR remains the same over time. In Case II the particles are initially located at the control species: maximum benefit occurs at the early times, but particles subsequently displace. Particles performing short jumps have an advantage over these that only do long jumps or both, since they remain closer to the resource for longer. On the other hand, particles who only perform long jumps disperse from the resource faster than the rest. However, all particles see reduced benefit over time due to dispersal away from the resource. Case III generates the inverse results of Case II: early on, particles accrue little benefit due

to being located away from the resource. Particles performing longer jumps have a greater advantage as they reach the resource faster than the rest. Summarising, for the case where transition rates are independent on the resource, the best strategy is to perform short jumps when localised near the resource and long jumps when localised further away.

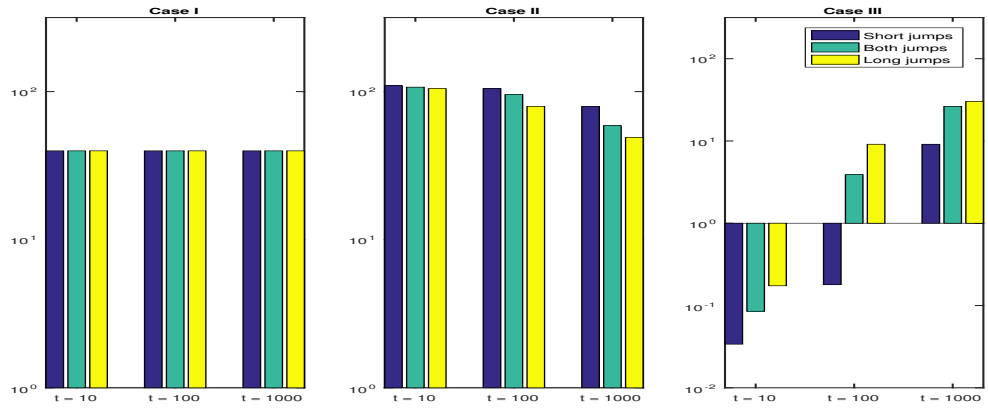

Figure 4.9: Log-scale plot of the benefit-cost ratio (BCR)for short (blue), both (green), and long (yellow) jump types for the three initial distributions (I-III) at different times. Here we have used constant transition rate functions, $\tau^i(u) = \alpha_i$, with parameters as set in the lext.

4.4.4.2 Decreasing transition rates

We now assume particles perform more jumps when the level of resource is low, and less jumps when the level of resource is high. We study the same cases above for different jump types over different times, see Figure 4.10. Case I again has identical results to the reference case: as the resource is homogeneously distributed, the benefit-cost ratio remains the same with time. We find again that a short jump strategy is the best strategy for case II, where the particles are located at the resource. In Case III the long jump is advantageous, since they reach the resource much faster. We note also that the decreasing transition rates give a better BCR over the constant rate for Case III: particles move quickly from low resource to high resource region.

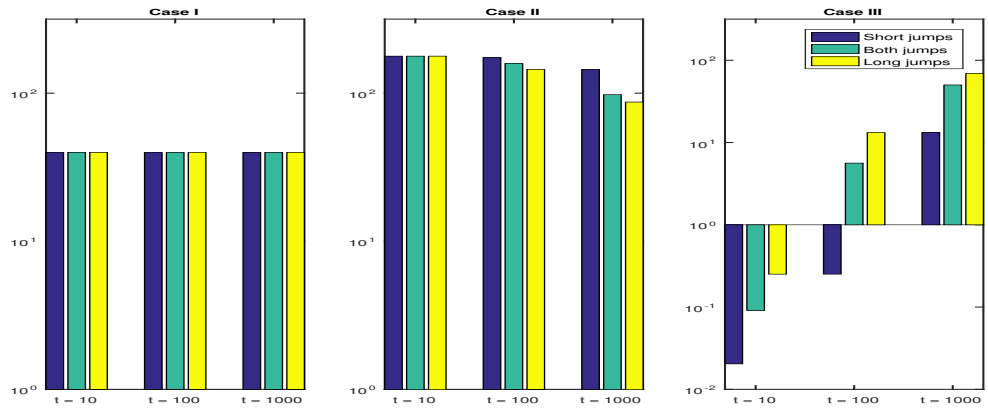

Figure 4.10: Log-scale plot of the benefit-cost ratio (BCR) for short (blue), both (green), and long (yellow) jump types for the three initial distributions (I-III) at different times. Here we have decreasing transition rate functions $\tau^i(u) = \frac{2\alpha_i u*}{u*+u}$, with parameters as set in the lext.

4.4.4.3 Increasing transition rates

We now assume particles perform more jumps when the level of resource is high and less jumps when the level of control resource is low. We study the same cases again, see Figure 4.11. Case I again generates the same benefit-cost ratio as the reference case. For Case II the best strategy is short jumps while long jumps are a better strategy for Case III at lower times, but less so after longer times. Overall, increasing transition rates appear to be less effective than either constant or decreasing forms.

4.4.4.4 Combined jump strategies

In the above sections we analysed different jump strategies individually. According to the distribution of the population/resource, different strategies perform more or less effectively. For example, if initially located far from the resource then the most effective strategy is to perform frequent long jumps, as this will allow the resource to be quickly located. If initially close to the resource, it is clearly better to stay as close as possible by limiting to shorter jumps.

We now investigate different combinations of strategy when performing both short and long jumps together. In particular, we will consider the impact of the following 4 combinations under the various distributions for population and resource:

- short and long jumps both increasing with the resource ($In_s + In_l$);

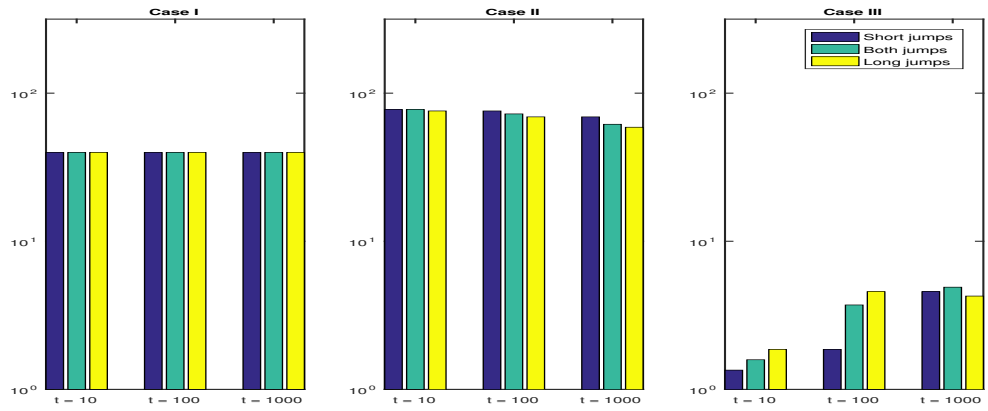

Figure 4.11: Log-scale plot of the benefit-cost ratio (BCR) for short (blue), both (green), and long (yellow) jump types for the three initial distributions (I-III) at different times. Here we have increasing transition rate functions $\tau^i(u) = \frac{2\alpha_i u}{u*+u}$, with parameters as set in the lext.

- short jumps increasing with the resource and long jumps decreasing with the resource ($In_s + De_l$);
- short and long jumps both decreasing with the resource ($De_s + De_l$);
- short jumps decreasing with the resource and long jumps increasing with the resource ($De_s + In_l$).

In Figure 4.12 we plot the log-scale of the benefit-cost ratio for the four strategies under the three arrangements of distributions (I-III). Case I shows ($In_s + De_l$) and ($De_s + In_l$) to be the best strategies. In Case II ($De_s + In_l$) generates the maximum benefit, followed second by ($In_s + De_l$). In Case III ($In_s + De_l$) perform the best over longer time periods.

4.4.4.5 Summary

Overall, when assessing the most effective strategy across the full range of initial distribution arrrangements, the ($In_s + De_l$) strategy appears to be the best combination: this strategy typically appears among the top two for any given initial arrangement of distribution. Intuitively, this makes logical sense. By performing long jumps only when the resource is low, the individuals only seek out new resource environments when in a poor one themselves. By performing short jumps

only when the food resource is high, the individuals tend to remain close to good resource regions.

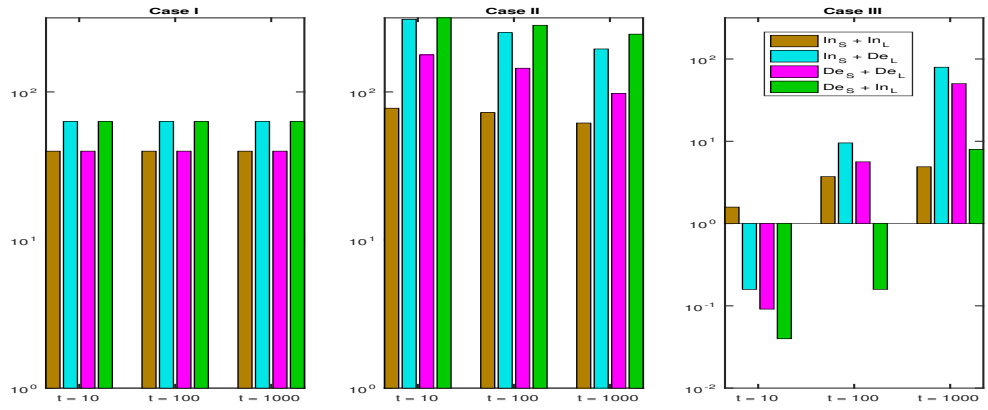

Figure 4.12: Log-scale of the benefit-cost ratio for combined short and long jump strategies at different times. See text for details.

4.5 Inclusion of resource consumption

We next extend our study to consider consumption of the resource: typically, a nutrient will be consumed over time leading to its depletion. We will investigate how quickly a population is able to find and reduce the resource. Specifically, we chose a decay function for $u(x,t)$ that describes consumption by the particles $p(x,t)$ over time, as follows:

$$\begin{aligned} \frac{\partial u}{\partial t} &= -\gamma u(x,t)p(x,t); \\ \frac{\partial p}{\partial t} &= d\sum_{i=1}^{m}[i^2\frac{\partial^2(\tau^i(u)p)}{\partial x^2}]. \end{aligned} \tag{4.36}$$

In the above γ is the rate of consumption. We assume as before that particles can perform both short and long jumps according to three different strategies: a constant rate of jumps, a rate that increases with the resource, and a rate that decreases with the resource, using the same functions (*),(**),(***) as before.

4.5.1 Initial condition for control species and particles

We use the same initial conditions for the resource and particles as before, see section 4.4.3 and Figure 4.8. We also consider the special case (Case*) of a randomised non-homogeneous function to describe the initial condition of the resource, along with a localised population as follows:

$$u(x,0) = NF \sum_{i=1}^{n} h_i \exp(-\sigma_i * (x-\mu_i)^2);$$
$$p(x,0) = \frac{L}{\sigma_p \sqrt{2\pi}} \exp(-\frac{(x-\mu_p)^2}{2\sigma_p^2}). \qquad (****)$$

Where NF is the normalising factor, n is an integer random number between 1 & 20, h_i, σ_i and μ_i are selected as uniformly distributed random variables, and σ_p is its standard deviation and μ_p is the mean of particles. We note that the above form for the resource represents a more naturally occurring resource distribution, varying across the environment: a representative example is shown in Figure 4.13.

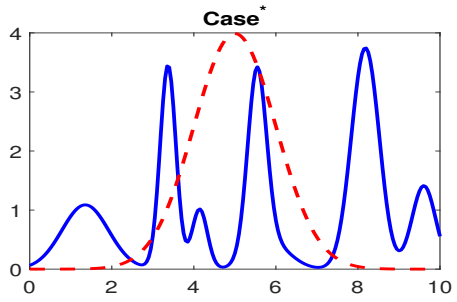

Figure 4.13: Illustration of initial distribution of resource (blue line), and particles (red dashed) for Case*. Fixing $\mu_p = 5$ and $\sigma_p = 1.0$

4.5.2 Measurement

To gauge the efficiency with which the population locates and consumes the resource we introduce as a measurement the time that the total resource is reduced to 10% of its initial value. We define our consumption time as t^*, such that:

$$\frac{1}{L}\int_0^L u(x,t^*)\,dx = \frac{0.1}{L}\int_0^L u(x,0)\,dx.$$

4.5.3 Results

We assume particles can perform either short or long jumps at rates that depend on the resource according to functions (*),(**),(***). Short jumps can occur at a constant rate C_s, a decreasing rate function De_s or increasing rate function In_s of the resource. Similarly, long jumps can occur at a constant rate C_l, a decreasing rate De_l or an increasing rate In_l according to the resource. Unsurprisingly, the shortest time it takes to reduce the resource by 90% occurs when the particles and the resource are initially colocalised (i.e Case II). Among the jump strategies, particles consume the resource at the fastest rate if both jump types occur at rates that decrease with the resource (De_s and De_l). While the choice of short jump strategy is relatively unimportant, the choice of long jump strategy is highly crucial: it is only effective to perform long jumps when the resource is low. Intuitively, lowering movement when the resource is high leads to its dissolution in a shorter time (see Figure 4.14 and 4.15).

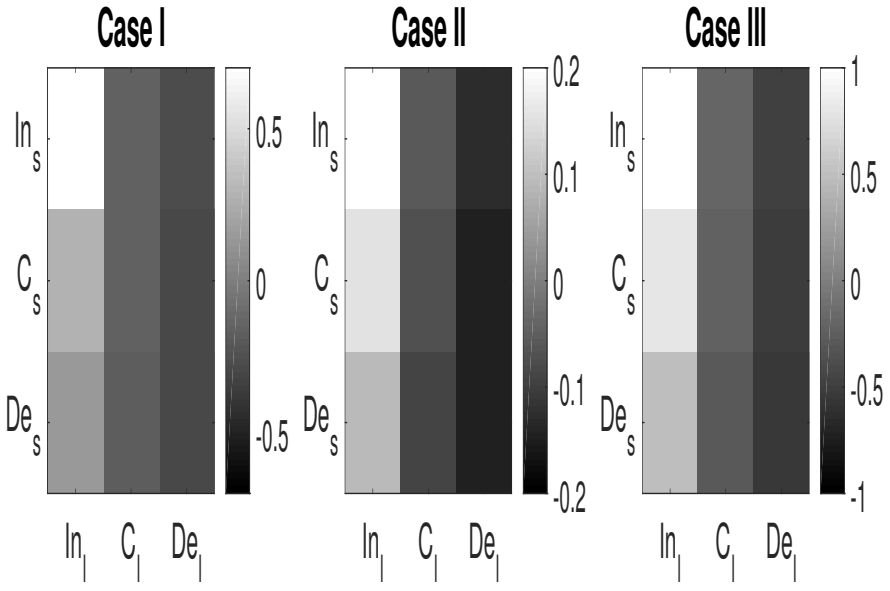

Figure 4.14: Plot of $\log_{10}$(consumption time/mean consumption time). Lighter colours represent a slower time of consumption and darker colour represents a faster time of consumption. Applying equations (4.36) with initial conditions in Section 4.4.3 and jump transition rates (*),(**),(***). Fixing $\alpha_s = 0.5$, $\alpha_l = 0.05$, $\Delta_s = h$, $\Delta_l = 10h$, where $h = 0.05$, $\gamma = 0.01$ and $d = 0.0025$. Numerics performed as in Figure 4.3.

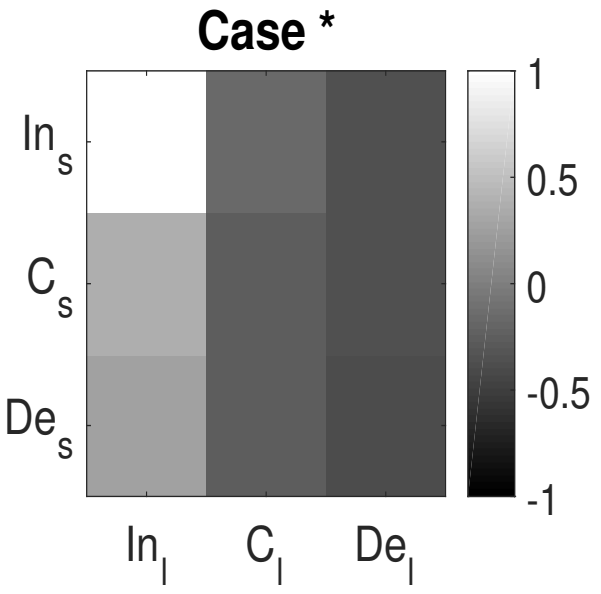

Figure 4.15: Plot of $\log_{10}$(consumption time/mean consumption time). Lighter colours represent slow times of consumption and darker colour represent faster times of consumption. Applying equations (4.36) with initial conditions (4.5.1) and jump transition rates (*),(**),(***). Fixing $\alpha_s = 0.5$, $\alpha_l = 0.05$, $\Delta_s = h$, $\Delta_l = 10h$, where $h = 0.05$, $\gamma = 0.01$ and $d = 0.0025$. Numerics performed as in Figure 4.3.

4.6 Application to glioma diffusion modelling

The poor prognosis of gliomas has been attributed to the highly invasive and diffuse nature of gliomas. In particular, an unknown fraction of tumour cells appear to travel far from the main tumour mass, remain undetected and subsequently evade localised therapies (e.g. surgery, radiotherapy). Consequently, cancer recurrence can occur in the peripheral regions of the original tumour, eventually leading to the patient's death. The patterns of invasion suggest that glioma cells can migrate along various structures that feature in the brain's microenvironment. In particular, observations suggest a tendency of glioma cells to infiltrate through both extracellular matrix as well as along oriented/linear structures of the brain, such as the white matter tracts comprised of bundles of neuronal axons or blood vessel capillaries [45, 42, 122, 11].

The vascular supply to different brain regions is far from homogeneous, with large differences in the capillary density and arrangement existing between grey and

white matter or among the various brain regions: the varying cellular and tissue composition of different brain regions demand very different levels of nutrient and oxygen supply from the blood vasculature. However, the interaction between the brain vasculature and glioma invasion is poorly understood [17, 73]. Histological examinations of both young and adult brain tissue indicates that gray matter has a significantly higher vessel density with a greater percentage area of blood vessels and lower mean area, breadth, length, perimeter and radius of blood vessels over white matter [9]. Other studies, albeit in rat brains [99], showed that while the capillary density is higher in gray matter (610±258 mm^{-2}) over white matter (417±209 mm^{-2}), edge-to-edge intermicrovessel distances are significantly less in gray matter (19.5±4.0 μm) than white matter (29.8±13.0 μm). In other words, there are more intrinsic capillaries with smaller intercapillary spaces in gray matter (where most neurons reside) than in white matter.

Similarly, the highly oriented tracts that form from bundles of neuronal axons are highly heterogeneous and anisotropic throughout the brain: while the neuronal cell bodies largely reside in gray matter, the long bundles of axons form a principal feature of the white matter, with the myelin-coated axons themselves giving the characteristically lighter shade of this tissue. The ability of glioma cells to invade along these axonal tracts [106] potentially allows the cells to move long distances through the brain.

Consequently, we can envisage that invasion/movements of glioma cells can follow various classes: from shortish range movements within the ECM, to medium range along oriented capillaries (before arriving at some capillary junction) to potentially very long range movements along white matter axonal tracts. In other words, the brain tissue environment can provide a complex network of B-roads, A-roads and motorways, allowing for distinct rates of invasion in different regions. In this preliminary study, we will use our modelling framework to phenomenologically show how the local tissue environment could potentially generate very different rates of invasion.

We introduce three different tissue types, where the structure of the tissue is

combined according to different percentages of axons, capillaries, and ECM. In *Case 1*, we consider

- Tissue 1: %50 capillaries, %25 axons, %25 ECM.
- Tissue 2: %50 axons, %25 capillaries , %25 ECM.
- Tissue 3: %50 ECM, %25 axons, %25 capillaries.

While in *Case 2*, we take more extreme variations:

- Tissue 1: %90 ECM, %5 axons, %5 capillaries.
- Tissue 2: %90 capillaries, %5 axons, %5 ECM.
- Tissue 3: %90 axons, %5 capillaries, %5 ECM.

We denote tissues containing more axons as (Axo), tissue with more capillaries as (Cap), and tissue with more ECM as (Ecm). In Figure 4.16 we illustrate a hypothetical example of tissue with %50 Axons, %25 ECM, and %25 Capillaries.

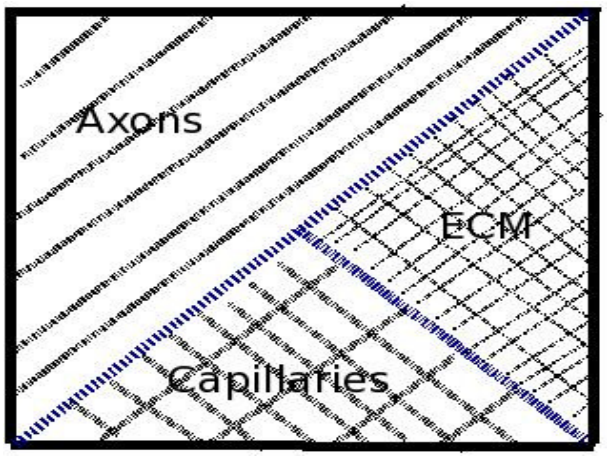

Figure 4.16: Sketch of tissue with %50 Axons, %25 ECM, and %25 Capillaries.

Furthermore, we assume glioma cells migrate along the different tissues as follows:

- (a) Short-range jumps (e.g. 1 step), for movements in ECM/high cellular areas.
- (b) Medium-range jumps (e.g. 3 steps), for movement along capillaries.
- (c) Long-range jumps (e.g. 10 steps, movement along axons).

4.6.1 Model set-up

We use a logistic form to represent the growth of glioma and assume the diffusion is derived from our multi-length random walk model. We investigate the invasion of glioma in the various tissue environments described above. We let $p(x,t)$ be the density of gliomas cells at a position x and time t, assuming $x \in [0, L]$, we have

$$\frac{\partial p}{\partial t} = d\sum_{i=1}^{m}[i^2\frac{\partial^2(\tau^i(\mathbf{u})p)}{\partial x^2}] + p(1-p), \tag{4.37}$$

with zero flux boundary conditions and initial conditions:

$$p(x,0) = \begin{cases} p_0(x) & \text{when } 0 \leq x \leq x^*, \\ 0 & \text{otherwise.} \end{cases} \tag{4.38}$$

We note that the above includes nondimensionalisation of cell density and time scale. The frequency of the different type of jumps is assumed to depend on how much of each type of structure is available for glioma invasion while the time for performing a jump will depend on the length of jump. Thus, we consider:

- $\tau^1(\text{Ecm}) \propto$ %ECM in the tissue;
- $\tau^2(\text{Cap}) \propto$ %Cap in the tissue;
- $\tau^3(\text{Axo}) \propto$ %Axo in the tissue.

Our focus will be on the following question: which tissue gives a greater rate of invasion?

4.6.2 Results

We solve equation (4.37) under initial condition (4.38) and zero flux bonundary conditions on the domain $x \in [0, 200]$. We calculate the invasion of glioma for each type of tissue in *Case 1* by tracking the position of the invasion wavefront at the final time of simulation $t = 500$, and compare it against a homogeneous tissue containing an equal percentage of ECM, capillaries, and axons (i.e $\frac{1}{3}capillaries, \frac{1}{3}axons, \frac{1}{3}ECM$).

Tissues with a high proportion of Axons show increased invasion depth, while those with more ECM or capillaries show decreased invasion. This indicates the greater invasion in white matter over grey matter, since long axons of white matter allow glioma cells to move long distance. Figure 4.17 shows the change of invasion for the three different heterogeneous tissues in relation to a homogeneous tissue. For the *Case 2* tissue types the invasion depths are greatly magnified (see Figure 4.18).

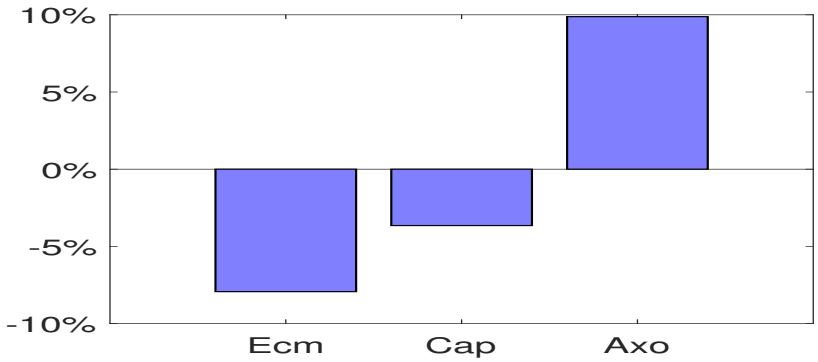

Figure 4.17: Degree of invasion for *Case 1*, in comparison to a homogeneous tissue.

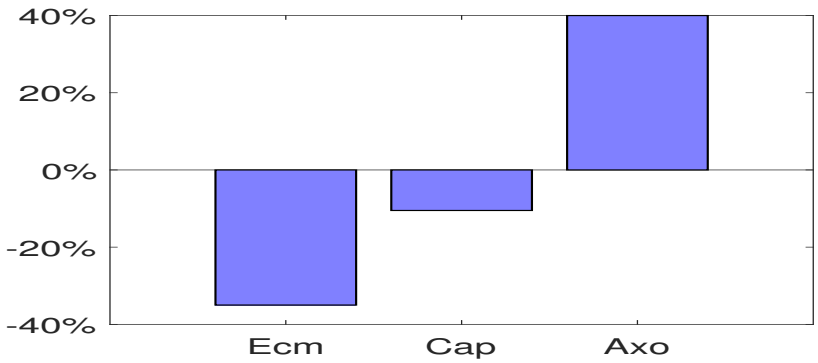

Figure 4.18: Degree of invasion for *Case 2*, in comparison to a homogeneous tissue.

4.6.3 Estimating the invasion speed analytically

We can also estimate the wave speed analytically by recalling that we effectively have Fisher's equation, with corresponding wave speed

$$\text{wave speed} = 2\sqrt{Df'(0)}.$$

We consider the minimum wave speed according to a diffusion coefficient varying for the transition probabilities under multiple length jumps:

$$D = d \sum_{i=1}^{m} [i^2 \tau^i(\mathbf{u})]. \tag{4.39}$$

Comparing to the study for *Case 1*, the analytical and simulated wave speed compare well (Figure 4.19).

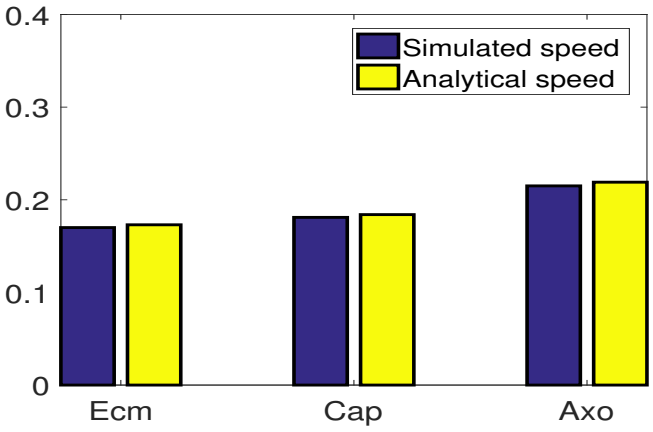

Figure 4.19: The analytical and simulated wave speed of three different tissues, Axons (Axo), ECM, and Capillaries (Cap).

4.6.4 Summary

Our multi jump length model can be applied to describe the dynamics of glioma invasion to take into consideration the heterogeneity of brain tissue. The results showed similar behaviour to in vivo glioma invasion [115, 51]: glioma cells have high invasion rates in white matter where there is a large number of axons. Of course this remains a preliminary and demonstrative pilot study and a future investigation should look more carefully at the parametrisation of the models.

4.7 Discussion

We have developed multi-step models based on random walks on a lattice. The models can be used to describe the movement of glioma cells as well as ecological movement. The model particles perform multiple-length jumps either to sites left or

right according to some transitional probability per unit time, which depends on the environmental information. We have shown that the stochastic version of the strictly local model corresponds well with its diffusion limit for high particle numbers. We have studied the efficiency of jump strategies for a constant and consumed resource environment. Under constant resource the long-jump strategy is the most effective if particles are located far from the resource, whereas, a short-jump strategy is better for the particles localised near the resource. For a consumed resource, if the particles perform short and long jumps types at rate that decrease with respect to the resource, they can consume it in a short amount of time. We have also applied the multiple-jump strictly local model to glioma invasion. The model takes into consideration the heterogeneity of brain tissue, with the probability of invasion per unit time depending on the brain components. The model shows that brain tissue with significant density of axons gives the highest glioma invasion.

Chapter 5

Conclusion and future work

The focus of this thesis has been divided into two components: modeling the go-or-grow mechanism of glioma cells under competition from healthy brain cells and modelling multi-jump-length random walks for movement under multiple resources.

5.1 Conclusion

- In Chapter 2 we reviewed some basic mathematical analysis and applied them to an ODE model to describe healthy-mutated cells interaction. The model was extended to cover the spatial dynamics of interaction and study how travelling wave solutions depended on model parameters. Numerical and analytical approaches were used to investigate the models. Simulating in vivo and in vitro scenarios, the results showed the importance of competition from healthy cells on controlling the invasion of tumour.

- In Chapter 3 we proposed a simple mathematical model based on the go-or-grow hypothesis for gliomas. The model built on an earlier model developed by Pham and others [91]. We have studied the model under constant and density dependent forms of probability for switching between proliferative and migratory cells phase. Simulations and stability analysis were performed for spatial and non-spatial versions of the model. The results suggest that increasing the probability of entering a migratory state may delay the rate at which a tumour overcomes the normal cells. Under density-dependent forms

we found that a decreasing switch function with the total density results in a greater proportion of proliferating cells in the system, and vice versa for increasing switching functions. Analysis into wave speeds indicates invasion of the tumour increases as the probability of switching to migratory cell increases until the probability of being in migratory state is equal to stationary state and then the wave speed starts to decrease. The results also showed the competition parameter of normal cells is the critical factor for reducing the invasion of tumour cells, as in simpler models.

- In Chapter 4 we presented a new framework for modelling movements of different characteristic lengths through a biased random walk in response to multiple resources. The model considered different hypotheses for movement based on a variety of local and nonlocal sensing strategies. We have investigated different strategies of movement with respect to some resource, and examined which strategy would allow a population to most efficiently search out its environment. Our results indicated that for static resources, a long-jump strategy is the most effective if particles are located far from the resource, whereas a short-jump strategy is better for the particles localised near the resource. For a consumed resource, if by performing movement at a rate that decreases with respect to the resource, they can quickly locate and consume it. We have also used a strictly local model to describe the invasion of glioma cells along different brain structures. The modelling suggests that brain tissue with a high density of axon can accelerate invasion.

5.2 Future work

Here we briefly outline some areas for future work.

5.2.1 Go-or-grow model extensions

- In our investigation in Chapter 3 we considered increasing and decreasing functions for a probability switch to migratory state. These switching forms

represent the pressure of the population [82] and contact inhibition [1] on cell motility respectively. Therefore, we could combine these hypotheses together: i.e cells become more migratory in a sparse environment (low density) and in a crowded environment (high density). Consequently, a bimodal function could be another possibility to describe the switch to migratory state.

- The outcome of our study of go-or-grow model within competition with normal/healthy cells showed the importance of the competitive nature of normal cells on the glioma cells in reducing the invasion of tumour, where the competition could arise from aspects such as limited nutrient supply or space. However, competitive interactions were not directly included into the migrating glioma cell population: we had an indirect competition, via the competition terms in the proliferating glioma cells, which would in turn lead to a reduced pool from which migrating cells could potentially arise. A more explicit representation of competition here would be to include the impact on migrating glioma cells of competition for, for example, space. One way to model this would be to add an additional term to equation (3.3) such as

$$\begin{aligned} \frac{\partial n}{\partial t} &= r_1 n(1 - \frac{n}{k_1} - a_1\frac{p+m}{k_2}); \\ \frac{\partial p}{\partial t} &= r_2 p(1 - \frac{p+m}{k_2} - a_2\frac{n}{k_1}) - \phi[\alpha(s)p - (1-\alpha(s))m]; \\ \frac{\partial m}{\partial t} &= D_m\frac{\partial^2 m}{\partial x^2} + \phi[\alpha(s)p - (1-\alpha(s))m] - a_3 n\frac{p+m}{k_2}. \end{aligned} \tag{5.1}$$

  where the above equations include new parameter a_3 representing the competition of normal cells on migrating glioma cells.

- We remark that migrating cells may be less sensitive to therapy than proliferating cells [72] and have the capacity to infiltrate and invade the brain along myelinated fiber tracts in the white matter [43]. Consequently, malignant tumours are generally found to recur following the original treatment phase. Therefore, an interesting development would be to investigate the go-or-grow mechanism under the effectiveness of treatment. For example, do different switching responses to cell densities create different responses to therapy? As

an example, if cells are more likely to switch into migrating cells at low densities, then therapies that reduce the cell density could trigger a greater switch into proliferating type and consequently accelerate invasion. Therefore, extending the model to include terms to describe treatment would be of interest. For instance: we assume proliferative tumour cells die due to chemotherapy. Therefore, we introduce a death term into equation (3.3) as follows

$$\begin{aligned} \frac{\partial n}{\partial t} &= r_1 n(1 - \frac{n}{k_1} - a_1\frac{p+m}{k_2}); \\ \frac{\partial p}{\partial t} &= r_2 p(1 - \frac{p+m}{k_2} - a_2\frac{n}{k_1}) - \phi[\alpha(s)p - (1-\alpha(s))m] - \overbrace{K(t)p}^{\text{death due chemotherapy}}; \\ \frac{\partial m}{\partial t} &= D_m\frac{\partial^2 m}{\partial x^2} + \phi[\alpha(s)p - (1-\alpha(s))m]. \end{aligned} \tag{5.2}$$

Where $K(t)$ is the temporal profile of the treatment.

- So far the parametrisation has been very minimal, but obviously there could be some modelling to investigate more realistic parameters. For example, different grades of tumours (e.g. high grade or low grade) can be modelled by different diffusion/proliferation rates [116, 14], and a more detailed study could look at a far more careful parametrisation of the model.

- It is believed that tumour aggressiveness is correlated with increasing glucose uptake [100]. However, upregulation of glycolysis leads to increasing the acidity of the microenvironment, and tumour cells in acidic environments promote unconstrained proliferation and invasion [40]. Furthermore, hypoxia and acidosis occur frequently, resulting in subsequent spread into regions of normal acidity [35]. Therefore, we could also link the competition in the model to the acidity of the environment. Further, we could incorporate the level of oxygen as a variable, along with how this will heterogeneously vary with the level of blood vasculature: the vascular supply to different brain regions is heterogeneous, with large differences in the capillary density and arrangement existing between grey and white matter or among the various brain region [9, 99].

- Analytically, we have performed a numerically based approach to studying

travelling wave speeds. It could therefore be interesting to try more formal mathematical analysis, perhaps by looking at simpler systems.

5.2.2 Multi-step jump models for movement extensions

- In our resource based study we have considered just one control species u. However, we could consider multiple resources in the environment, which could have different degrees of benefit (e.g high/low nutrient value). Therefore, the transition rate of jumps will depend on more than one control species $\tau^i(u_1, u_2, ...)$.

- We could connect the model more formally to a specific ecological system, for example insects, where we may be able to find data on the frequency and length of different movements. Also, one could perhaps extend the model to bring in population dynamics or the impact of population densities: for example, if the population becomes one of the control species (i.e $\tau^i(u, p)$), one could investigate when is it better to be a more adventurous individual that moves away from a decent but crowded resource, i.e. where one has to compete with others, to make a long distance move to somewhere that may prove to be better (i.e. less crowded and decent resource) or worse (i.e. poor resource).

- We have also only focused on the strictly local model in our analysis, but clearly a more detailed approach would examine the impact of the different methods for sensing the environment, and how this determines what type of jumping strategy would be better.

- We also considered the control species as either a constant or decaying function. However, the resource can also grow and extension to consider its growth dynamic could be of interest. Moreover, a competition of two or more population types that perform different jump strategies can be considered as a future investigation. An example of this in nature would be the consumption of small fishes by eagles or larger fishes. For instance: we propose a model of

fish (F) as our control species, and two competing populations, eagles (E) and larger fish (L) as following

$$\begin{aligned}
\frac{\partial F}{\partial t} &= \text{growth} + \text{movement} - \text{death by E} - \text{death by L};\\
\frac{\partial E}{\partial t} &= d\sum_{i=1}^{m}[i^2\frac{\partial^2(\tau^i(F)E)}{\partial x^2}] + \text{growth} - \text{competition with L};\\
\frac{\partial L}{\partial t} &= d\sum_{j=1}^{n}[j^2\frac{\partial^2(\tau^j(F)L)}{\partial x^2}] + \text{growth} - \text{competition with E}.
\end{aligned} \tag{5.3}$$

Where i and j represent multi step jumps.

- Further investigation of the data of sharks movement could also be performed to examine whether the multi-length jump model gives the same result for Levy flight model [57], or more carefully compare how they differ.

- We have briefly studied glioma movement along different environmental structures. This would, of course, be hugely benefited by a much more careful parametrisation. For example, from some of the experimental studies it may be possible to evaluate how average movement steps vary according to whether the individual cell is moving along capillaries, axons.

- Another interesting direction would be to combine the work on multi-step jump processes with the competitive model for glioma invasion. For example, we could model a population of normal cells which compete with a population of glioma cells that switch between proliferating and migrating phenotypes according to the go or grow hypothesis. In this case, the density of normal and glioma cells in the environment (or the degree of competition between them) could lead to both an increased probability of becoming a migratory cell and an increased probability of subsequently performing a long range jump.

$$\begin{aligned}
\frac{\partial p}{\partial t} &= d\sum_{i=1}^{m}[i^2\frac{\partial^2(\tau^i(\mathbf{u},\mathbf{n})p)}{\partial x^2}] + r_1 p(1-p/k_1),\\
\frac{\partial n}{\partial t} &= d\sum_{j=1}^{m}[j^2\frac{\partial^2(\tau^j(\mathbf{u})n)}{\partial x^2}] + r_2 n(1-n/k_2).
\end{aligned} \tag{5.4}$$

Here i and j represent multi step jumps.

- Clearly, a more careful modelling of the heterogeneity of the brain would be of interest: for example, DTI imaging can give information on the arrangement of axons while other imaging techniques can give rise to a picture of the vasculature levels as an example, microcomputed tomography (micro-CT). Therefore movement to either a 2D or 3D model (along the lines of Swanson et al [115]) to investigate the heterogeneous spread of tumours and how it varied across the different regions of the brain would be an exciting study: previous work has tended to focus on just the grey/white matter distinction, but clearly incorporating the variable vasculature arrangement could be crucial to the overall spread. Also, given that the vasculature arrangement is changed by the tumour (via angiogenesis), one could potentially make the capillary density a dynamic control species, boosted by the tumour and hence facilitating the path of invasion.

Appendix A

Steady States And Linear Stability Analysis Of First and Second Order ODEs

A.1 Steady states and linear stability analysis of first order ODE

We review stability analysis for a general first order ordinary differential equation (ODE), and then apply it to the equation (2.2). Consider the general form equation for the first order ODE

$$u_t = f(u), \tag{A.1}$$

with initial condition

$$u(0) = u_0,$$

we say u^* is steady state if the condition $f(u^*) = 0$ is satisfied.

We linearize equation (A.1) around the steady state u^* by $u = u^* + \varepsilon$, where ε is very small. Hence, using Taylor expansion

$$f(u) = f(u^* + \varepsilon) = f(u^*) + \varepsilon f^{'}(u^*) + h.o.t$$

where *h.o.t* is an abbreviation for higher order terms. Then

$$\frac{d\varepsilon}{dt} = \varepsilon f^{'}(u^*),$$

which has solution $\varepsilon(t) = \varepsilon_0 e^{f^{'}(u^*)}$. It is clear that the long term behaviour of the solution is depend on the sign of $f^{'}(u^*)$. If $f^{'}(u^*) > 0$ then, close to steady state, ε is exponential increasing as $t \longrightarrow \infty$, and the steady state u^* is unstable. Whereas, If $f^{'}(u^*) < 0$ the steady state is stable since ε is exponential decreasing to zero $\varepsilon \longrightarrow 0$ as $t \longrightarrow \infty$.

A.2 Steady states and linear stability analysis of second order ODE

Linear stability analysis extends naturally to the case of two (or more) species. Consider first the general system of two first-order ordinary differential equations:

$$\begin{aligned} \frac{dx}{dt} &= f(x, y), \\ \frac{dy}{dt} &= g(x, y), \end{aligned} \tag{A.2}$$

to be solved with two initial conditions

$$x(0) = x_0, \qquad y(0) = y_0$$

Suppose x^* and y^* are steady states, i.e.

$$f(x^*, y^*) = 0,$$

$$g(x^*, y^*) = 0.$$

We consider perturbations $\tilde{x} = x - x^*$ and $\tilde{y} = y - y^*$, substitute into the above equations (A.2) and expand the RHS terms as a Taylor's expansion. Ignoring the

non-linear terms, we obtain

$$\frac{dx}{dt} = f_x\tilde{x} + f_y\tilde{y},$$

$$\frac{dy}{dt} = g_x\tilde{x} + g_y\tilde{y},$$

where $f_x = \frac{\partial f}{\partial x}|_{x^*,y^*}$, $f_y = \frac{\partial f}{\partial y}|_{x^*,y^*}$,$g_x = \frac{\partial g}{\partial x}|_{x^*,y^*}$ and $g_y = \frac{\partial g}{\partial y}|_{x^*,y^*}$.

In Matrix form

$$\frac{d}{dt}\begin{pmatrix}\tilde{x}\\ \tilde{y}\end{pmatrix} = \begin{pmatrix}f_x & f_y\\ g_x & g_y\end{pmatrix}\begin{pmatrix}\tilde{x}\\ \tilde{y}\end{pmatrix} = J\begin{pmatrix}\tilde{x}\\ \tilde{y}\end{pmatrix},$$

where J is the Jacobian matrix.

Solutions of the linearised equations have the form $(\tilde{x}, \tilde{y}) \sim \text{cst}\underline{w}_1.e^{\lambda_1 t} + \text{cst}.\underline{w}_2 e^{\lambda_2 t}$ where $\lambda_{1,2}$ are the eigenvalues and $\underline{w}_{1,2}$ are the eignvector of J. If the real part of ($\lambda_{1,2}) < 0$, our perturbations will decay to zero and the steady state is linearly stable.

We can determine the sign of the eigenvalues from the characteristic equation of J

$$\lambda^2 - \beta\lambda + \gamma = 0 \Rightarrow \lambda = 1/2(\beta \pm \sqrt{\beta^2 - 4\gamma}).$$

Hence for $Re(\lambda) < 0$ we need $\beta < 0$ & $\gamma > 0$ where $\beta = \text{tr } J$, $\gamma = \det J$.

A.3 Travelling waves in Fisher's equation

Fisher's equation (2.10) is considered as one of the simple examples of nonlinear reaction diffusion equation. It was suggested by Fisher [33], and, while it has has no analytical solution in general, it is easy to solve numerically and obtain analytical solutions near the steady states. The advantage of using this equation lie in its ability to generate travelling wavefront solutions (constant shape and speed). Fisher's equation is given by

$$\frac{\partial u}{\partial t} = D\frac{\partial^2 u}{\partial x^2} + ru(1-u), \tag{A.3}$$

where D is the diffusion coeffiant and $rc(1-c)$ describes logistic growth. To analyse travelling waves we rescale with

$$t^* = rt, \qquad x^* = x\sqrt{\frac{r}{D}},$$

to obtain the dimensionless form with carrying capacity $k = 1$,

$$\frac{\partial u}{\partial t} = \frac{\partial^2 u}{\partial x^2} + u(1-u). \tag{A.4}$$

The above equation has two uniform steady states: an unstable steady state $u = 0$ and a stable steady state $u = 1$. For travelling waves, the shape and speed c of the solution $u(x,t)$ is constant. We therefore introduce the wave variable z, and assume travelling waves, i.e:

$$u(x,t) = U(x-at) = U(z), \qquad z = x - ct.$$

With this, the partial differential equations in x and t becomes a second order ordinary differential equation in z:

$$U'' + cU' + U(1-U) = 0, \tag{A.5}$$

where the primes denote differentiation with respect to z. For travelling waves connecting $(1,0)$ and $(0,0)$, we set

$$\lim_{z\to\infty} U(z) = 0, \qquad \lim_{z\to-\infty} U(z) = 1.$$

To analyse this system we explore the (U,V) phase plane, where

$$U' = V, \qquad V' = -cV - U(1-U).$$

This system of two ordinary differential equations has two steady states $(0,0)$ and $(1,0)$. A linear stability shows that for the $(0,0)$ steady state the eigenvalues λ are

given by

$$\lambda_{\pm} = \frac{1}{2}[-c \pm (c^2 - 4)^{1/2}] \Rightarrow \begin{cases} \text{stable node} & \text{if } c^2 \geq 4 \\ \text{stable spiral} & \text{if } c^2 < 4 \end{cases}.$$

For the $(1, 0)$ steady state, the eigenvalues λ are given by

$$\lambda_{\pm} = \frac{1}{2}[-c \pm (c^2 + 4)^{1/2}] \Rightarrow \text{saddle point.}$$

We see the origin $(0, 0)$ is a stable node if $c \geq c_{min} = 2$ and from the phase plane sketch (see Figure A.1) a trajectory from $(1, 0)$ to $(0, 0)$ that lies entirely in the quadrant $U \geq 0$, $U' \leq 0$ only occurs for wave speeds $c \geq c_{min} = 2$. Hence, this gives a minimum wave speed for biologically realistic solution.

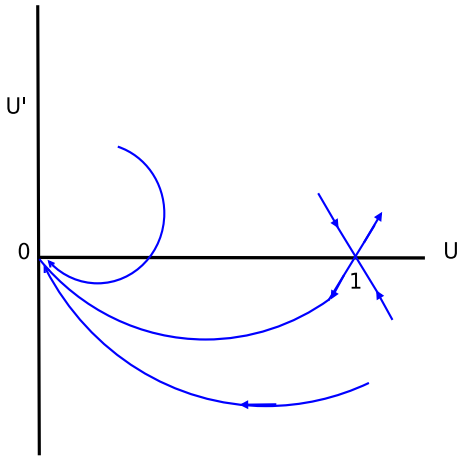

Figure A.1: Phase plane trajectories.

In the original dimensional equation (2.10) the wave speed satisfy

$$c \geq c_{min} = 2\sqrt{rD}. \tag{A.6}$$

There are travelling wave solution for the origin $(0, 0)$ if $a < 2$ but they are (biologically) unrealistic since in this case we have spirals and hence negative solution values. The dependence of the wave speed c on the initial conditions has been widely studied. For example, Kolmogoroff et al. proven that if the initial condition $u(x, t)$ has compact support, then the solution $u(x, t)$ of evolves to a travelling wavefront solution $U(z)$ at the minimum speed $c_{min} = 2$. For other initial conditions the solution depends on the behaviour of $u(x, 0)$ as $x \to \pm\infty$.

Appendix B

Multi step jumps of movement models

B.1 Local average & Nonlocal average

The local average models are based on the assumption that transition rates depend on the average information between the current and target node.

B.1.1 Local average model

Local average implies that the individual does a small amount of sampling both locally and nearby, but then still does a leap into the unknown. The jump of particle at node x to node $x \pm i$ depends on the average information of the control species between the current and nearest neighbour, in the direction of the target node as described below:

$$\tau_x^{+1}(\mathbf{u}) = \boldsymbol{\tau}^1(\frac{1}{2}(\mathbf{u}_x + \mathbf{u}_{x+1})); \qquad \tau_x^{-1}(\mathbf{u}) = \boldsymbol{\tau}^1(\frac{1}{2}(\mathbf{u}_x + \mathbf{u}_{x-1}));$$

$$\tau_x^{+2}(\mathbf{u}) = \boldsymbol{\tau}^2(\frac{1}{2}(\mathbf{u}_x + \mathbf{u}_{x+1})); \qquad \tau_x^{-2}(\mathbf{u}) = \boldsymbol{\tau}^2(\frac{1}{2}(\mathbf{u}_x + \mathbf{u}_{x-1}));$$

$$\tau_x^{+i}(\mathbf{u}) = \boldsymbol{\tau}^i(\frac{1}{2}(\mathbf{u}_x + \mathbf{u}_{x+1})); \qquad \tau_x^{-i}(\mathbf{u}) = \boldsymbol{\tau}^i(\frac{1}{2}(\mathbf{u}_x + \mathbf{u}_{x-1})).$$

Similarly, at site $x \pm i$:

$$\tau_{x-1}^{+1}(\mathbf{u}) = \boldsymbol{\tau}^1(\frac{1}{2}(\mathbf{u}_{x-1} + \mathbf{u}_x)); \qquad \tau_{x+1}^{-1}(\mathbf{u}) = \boldsymbol{\tau}^1(\frac{1}{2}(\mathbf{u}_{x+1} + \mathbf{u}_x));$$

$$\tau_{x-2}^{+2}(\mathbf{u}) = \boldsymbol{\tau}^2(\frac{1}{2}(\mathbf{u}_{x-2} + \mathbf{u}_{x-1})); \qquad \tau_{x+2}^{-2}(\mathbf{u}) = \boldsymbol{\tau}^2(\frac{1}{2}(\mathbf{u}_{x+2} + \mathbf{u}_{x+1}));$$

$$\tau_{x-m}^{+m}(\mathbf{u}) = \boldsymbol{\tau}^m(\frac{1}{2}(\mathbf{u}_{x-m} + \mathbf{u}_{x-(m-1)})); \qquad \tau_{x+m}^{-m}(\mathbf{u}) = \boldsymbol{\tau}^m(\frac{1}{2}(\mathbf{u}_{x+m} + \mathbf{u}_{x+(m-1)})).$$

We provide a scaling of the transition rates $\tau^i = \lambda\tau^i$, and take the limit

$$lim_{\lambda\to\infty, h\to 0}\lambda h^2 = d,$$

to obtain the diffusion equation:

$$\frac{\partial p}{\partial t} = d\sum_{i=1}^{m}[(i^2 - i)p\frac{\partial^2\boldsymbol{\tau}^i(\mathbf{u})}{\partial x^2} + (2i^2 - i)\frac{\partial\boldsymbol{\tau}^i(\mathbf{u})}{\partial x}\frac{\partial p}{\partial x} + i^2\boldsymbol{\tau}^i(\mathbf{u})\frac{\partial^2 p}{\partial x^2}. \tag{B.1}$$

B.1.2 Nonlocal average model

The nonlocal average model implies that individuals have a capacity to detect the environment where it plans on moving to (e.g. a cell that extends filopodia or an animal that visually spies the site). The jump of a particle at node x to node $x \pm i$ depends on the average information of the control species between the current and target node as described below:

$$\tau_x^{+1}(\mathbf{u}) = \boldsymbol{\tau}(\frac{1}{2}(\mathbf{u}_x + \mathbf{u}_{x+1})); \qquad \tau_x^{-1}(\mathbf{u}) = \boldsymbol{\tau}(\frac{1}{2}(\mathbf{u}_x + \mathbf{u}_{x-1}));$$

$$\tau_x^{+2}(\mathbf{u}) = \boldsymbol{\tau}(\frac{1}{2}(\mathbf{u}_x + \mathbf{u}_{x+2})); \qquad \tau_x^{-2}(\mathbf{u}) = \boldsymbol{\tau}(\frac{1}{2}(\mathbf{u}_x + \mathbf{u}_{x-2}));$$

$$\tau_x^{+m}(\mathbf{u}) = \boldsymbol{\tau}(\frac{1}{2}(\mathbf{u}_x + \mathbf{u}_{x+m})); \qquad \tau_x^{-m}(\mathbf{u}) = \boldsymbol{\tau}(\frac{1}{2}(\mathbf{u}_x + \mathbf{u}_{x-m}));$$

Similarly at site $x \pm i$:

$$\tau_{x-1}^{+1}(\mathbf{u}) = \boldsymbol{\tau}(\frac{1}{2}(\mathbf{u}_{x-1} + \mathbf{u}_x)); \qquad \tau_{x+1}^{-1}(\mathbf{u}) = \boldsymbol{\tau}(\frac{1}{2}(\mathbf{u}_{x+1} + \mathbf{u}_x));$$

$$\tau^{+2}_{x-2}(\mathbf{u}) = \tau(\frac{1}{2}(\mathbf{u}_{x-2} + \mathbf{u}_x)); \qquad \tau^{-2}_{x+2}(\mathbf{u}) = \tau(\frac{1}{2}(\mathbf{u}_{x+2} + \mathbf{u}_x));$$

$$\tau^{+m}_{x-m}(\mathbf{u}) = \tau(\frac{1}{2}(\mathbf{u}_{x-m} + \mathbf{u}_x)); \qquad \tau^{-m}_{x+m}(\mathbf{u}) = \tau(\frac{1}{2}(\mathbf{u}_{x+m} + \mathbf{u}_x)).$$

We provide a scaling of the transition rates $\tau^i = \lambda\tau^i$, and take the limit

$$lim_{\lambda\to\infty,h\to 0}\lambda h^2 = d,$$

to obtain the diffusion equation

$$\frac{\partial p}{\partial t} = d\sum_{i=1}^{m}[i^2\frac{\partial}{\partial x}(\tau^i(\mathbf{u})\frac{\partial p}{\partial x}]. \tag{B.2}$$

B.2 Local neighbour & Nonlocal neighbour models

The neighbour models are based on an assumption that the transition rates depend only on the information at the target jump site. Here we assume two different scenarios of neighbor based models as follows:

B.2.1 Local neighbour model

Here, the jump of a particle at node x to node $x \pm i$ is assumed to depend on the control species at the nearest neighbour in the direction of the arrival point as described below:

$$\tau^{+1}_{x}(\mathbf{u}) = \tau(u_{x+1}); \qquad \tau^{-1}_{x}(\mathbf{u}) = \tau(u_{x-1});$$

$$\tau^{+2}_{x}(\mathbf{u}) = \tau(u_{x+1}); \qquad \tau^{-2}_{x}(\mathbf{u}) = \tau(u_{x-1});$$

$$\tau^{+m}_{x}(\mathbf{u}) = \tau(u_{x+1}); \qquad \tau^{-m}_{x}(\mathbf{u}) = \tau(u_{x-1}).$$

Similarly at site $x \pm i$:

$$\tau^{+1}_{x-1}(\mathbf{u}) = \tau(u_x); \qquad \tau^{-1}_{x+1}(\mathbf{u}) = \tau(u_x);$$

$$\tau^{+2}_{x-2}(\mathbf{u}) = \tau(u_{x-1}); \qquad \tau^{-2}_{x+2}(\mathbf{u}) = \tau(u_{x+1});$$

$$\tau^{+m}_{x-m}(\mathbf{u}) = \boldsymbol{\tau}(u_{x-(m-1)}); \qquad \tau^{-m}_{x+m}(\mathbf{u}) = \boldsymbol{\tau}(u_{x+(m-1)}).$$

We substitute the new form of τ in the master equation (4.1) and expand the RHS using Taylor series. Taking the same scaling as previously, we obtain the following equation for multiple jumps of length $i = 1, ..., m$ for the local neighbour model:

$$\frac{\partial p}{\partial t} = d\sum_{i=1}^{m}[i^2\boldsymbol{\tau}(\mathbf{u})\frac{\partial^2 p}{\partial x^2} + 2(i^2 - i)\frac{\partial \boldsymbol{\tau}}{\partial x}\frac{\partial p}{\partial x} + (i^2 - 2i)p\frac{\partial^2 \boldsymbol{\tau}}{\partial x^2}]. \tag{B.3}$$

B.2.2 Nonlocal neighbour model

Here, the jump of a particle at node x to node $x \pm i$ is assumed to depend on the control species at the arrival point $x \pm i$ as described below:

$$\tau^{+1}_{x}(\mathbf{u}) = \boldsymbol{\tau}(\mathbf{u}_{x+1}); \qquad \tau^{-1}_{x} = \boldsymbol{\tau}(\mathbf{u}_{x-1});$$

$$\tau^{+2}_{x}(\mathbf{u}) = \boldsymbol{\tau}(\mathbf{u}_{x+2}); \qquad \tau^{-2}_{x} = \boldsymbol{\tau}(\mathbf{u}_{x-2});$$

$$\tau^{+m}_{x}(\mathbf{u}) = \boldsymbol{\tau}(\mathbf{u}_{x+m}); \qquad \tau^{-m}_{x} = \boldsymbol{\tau}(\mathbf{u}_{x-m}).$$

Similarly at site $x \pm i$:

$$\tau^{+1}_{x-1}(\mathbf{u}) = \boldsymbol{\tau}(\mathbf{u}_{x}); \qquad \tau^{-1}_{x+1} = \boldsymbol{\tau}(\mathbf{u}_{x});$$

$$\tau^{+2}_{x-2}(\mathbf{u}) = \boldsymbol{\tau}(\mathbf{u}_{x}); \qquad \tau^{-2}_{x+2} = \boldsymbol{\tau}(\mathbf{u}_{x});$$

$$\tau^{+m}_{x-m}(\mathbf{u}) = \boldsymbol{\tau}(\mathbf{u}_{x}); \qquad \tau^{-m}_{x+m} = \boldsymbol{\tau}(\mathbf{u}_{x}).$$

We substitute the new form of τ into the master equation (4.1) and expand the RHS using Taylor series. We take the standard scaling of the transition rates as before: $\tau^i = \lambda\tau^i$ and take the limit $lim_{\lambda\to\infty,h\to 0}\lambda h^2 = d$. We obtain the following diffusion equation for multiple jumps of length $i = 1, ..., m$ for the nonlocal neighbour model:

$$\frac{\partial p}{\partial t} = d\sum_{i=1}^{m}[i^2\frac{\partial}{\partial x}(\boldsymbol{\tau}(\mathbf{u})\frac{\partial p}{\partial x} - p\frac{\partial \boldsymbol{\tau}(\mathbf{u})}{\partial x})]. \tag{B.4}$$

B.3 Local gradient & Nonlocal gradient models

In this models the transition rate depends on the difference between the density of control species at the current and target node. Here we also have two different scenarios:

B.3.1 Local gradient model

The local gradient model is based on the assumption that the transition rates depends linearly on the difference between the density of control species at the current node and the nearest neighbour in the direction of the arrival node . In one space dimension the transition rate can be written as :

$$\tau_x^{+1} = a_1 + b_1(\tau(u_{x+1}) - \tau(u_n)); \qquad \tau_x^{-1} = a_1 + b_1(\tau(u_{x-1}) - \tau(u_x));$$

$$\tau_x^{+2} = a_2 + b_2(\tau(u_{x+1}) - \tau(u_n)); \qquad \tau_x^{-2} = a_2 + b_2(\tau(u_{x-1}) - \tau(u_x));$$

$$\tau_x^{+m} = a_m + b_m(\tau(u_{x+1}) - \tau(u_n)); \qquad \tau_x^{-m} = a_m + b_m(\tau(u_{x-1}) - \tau(u_x)).$$

Similarly at site $x \pm i$:

$$\tau_{x-1}^{+1} = a_1 + b_1(\tau(u_x) - \tau(u_{x-1})); \qquad \tau_{x+1}^{-1} = a_1 + b_1(\tau(u_x) - \tau(u_{x+1}));$$

$$\tau_{x-2}^{+2} = a_2 + b_2(\tau(u_{x-1}) - \tau(u_{x-2})); \qquad \tau_{x+2}^{-2} = a_2 + b_2(\tau(u_{x+1}) - \tau(u_{x+2}));$$

$$\tau_{x-m}^{+m} = a_m + b_m(\tau(u_{x-(m-1)}) - \tau(u_{x-m})); \qquad \tau_{x+m}^{-m} = a_m + b_m(\tau(u_{x+(m-1)}) - \tau(u_{x+m})).$$

In the above, $\tau : \mathbf{R}^k \to \mathbf{R}$, and $a_{1,\ldots,m} \geq 0$ and $b_{1,\ldots,m}$ are constants. We assume a scaling of the transition rates $\tau^i = \lambda\tau^i$ and take the limit

$$lim_{\lambda\to\infty, h\to 0} \lambda h^2 = d,$$

to obtain the diffusion equation

$$\frac{\partial p}{\partial t} = d \sum_{i=1}^{m} [a_i i^2 \frac{\partial^2 p}{\partial x^2} - 2ib_i \frac{\partial}{\partial x}(\frac{\partial \tau^i}{\partial x} p)]. \tag{B.5}$$

B.3.2 Nonlocal gradient model

Here, the transition rates depend on the difference between the density of the control species at the current node and the arrival node . For a linear dependence gradient in one space dimension, we assume the transtion rate at site x are as follow:

$$\tau_x^{+1} = a_1 + b_1(\tau(u_{x+1}) - \tau(u_x)); \qquad \tau_x^{-1} = a_1 + b_1(\tau(u_{x-1}) - \tau(u_x));$$

$$\tau_x^{+2} = a_2 + b_2(\tau(u_{x+2}) - \tau(u_x)); \qquad \tau_x^{-2} = a_2 + b_2(\tau(u_{x-2}) - \tau(u_x));$$

$$\tau_x^{+m} = a_m + b_m(\tau(u_{x+m}) - \tau(u_x)); \qquad \tau_x^{-m} = a_m + b_m(\tau(u_{x-m}) - \tau(u_x)).$$

Similarly at site $x \pm i$:

$$\tau_{x-1}^{+1} = a_1 + b_1(\tau(u_x) - \tau(u_{x-1})); \qquad \tau_{x+1}^{-1} = a_1 + b_1(\tau(u_x) - \tau(u_{x+1}));$$

$$\tau_{x-2}^{+2} = a_2 + b_2(\tau(u_x) - \tau(u_{x-2})); \qquad \tau_{x+2}^{-2} = a_2 + b_2(\tau(u_x) - \tau(u_{x+2}));$$

$$\tau_{x-m}^{+m} = a_m + b_m(\tau(u_x) - \tau(u_{x-m})); \qquad \tau_{x+m}^{-m} = a_m + b_m(\tau(u_x) - \tau(u_{x+m})).$$

In the above, $\tau : \mathbf{R}^k \to \mathbf{R}$, and $a_{1,\ldots,m} \geq 0$ and $b_{1,\ldots,m}$ are constants. We scale of the transition rate and introduce the limit $lim_{\lambda\to\infty,h\to 0}\lambda h^2 = d$ to obtain the diffusion equation:

$$\frac{\partial p}{\partial t} = d\sum_{i=1}^{m}[a_i i^2 \frac{\partial^2 p}{\partial x^2} - 2b_i i^2 \frac{\partial \tau}{\partial x}\frac{\partial p}{\partial x} - 2b_i i^2 \frac{\partial^2 \tau}{\partial x^2} p]. \tag{B.6}$$

Bibliography

[1] M. Abercrombie. The croonian lecture, 1978: the crawling movement of metazoan cells. *Proceedings of the Royal Society of London B: Biological Sciences*, 207(1167):129–147, 1980.

[2] H.-O. Adami. *Textbook of cancer epidemiology*. Oxford University Press, USA, 2008.

[3] T. Alarcón, H. M. Byrne, and P. K. Maini. A multiple scale model for tumor growth. *Multiscale Modeling & Simulation*, 3(2):440–475, 2005.

[4] F. Albrecht, H. Gatzke, A. Haddad, and N. Wax. The dynamics of two interacting populations. *Journal of Mathematical Analysis and Applications*, 46(3):658–670, 1974.

[5] E. C. Alvord Jr and C. Shaw. Neoplasms affecting the nervous system of the elderly. *The Pathology of the Aging Human Nervous System. Philadelphia: Lea and Fabiger*, pages 210–286, 1991.

[6] D. Andow, P. M. Kareiva, S. A. Levin, and A. Okubo. Spread of invading organisms. *Landscape Ecology*, 4(2):177–188, 1990.

[7] D. Aronson. The role of diffusion in mathematical population biology: Skellam revisited. In *Mathematics in biology and medicine*, pages 2–6. Springer, 1985.

[8] M. Assanah, R. Lochhead, A. Ogden, J. Bruce, J. Goldman, and P. Canoll. Glial progenitors in adult white matter are driven to form malignant gliomas by platelet-derived growth factor-expressing retroviruses. *The Journal of neuroscience*, 26(25):6781–6790, 2006.

[9] P. Ballabh, A. Braun, and M. Nedergaard. Anatomic analysis of blood vessels in germinal matrix, cerebral cortex, and white matter in developing infants. *Pediatric Research*, 56(1):117–124, 2004.

[10] A. T. Beliën, P. A. Paganetti, and M. E. Schwab. Membrane-type 1 matrix metalloprotease (mt1-mmp) enables invasive migration of glioma cells in central nervous system white matter. *The Journal of cell biology*, 144(2):373–384, 1999.

[11] A. C. Bellail, S. B. Hunter, D. J. Brat, C. Tan, and E. G. Van Meir. Microregional extracellular matrix heterogeneity in brain modulates glioma cell invasion. *The international journal of biochemistry & cell biology*, 36(6):1046–1069, 2004.

[12] K. Böttger, H. Hatzikirou, A. Chauviere, and A. Deutsch. Investigation of the migration/proliferation dichotomy and its impact on avascular glioma invasion. *Mathematical Modelling of Natural Phenomena*, 7(1):105–135, 2012.

[13] N. Britton. *Essential mathematical biology*. Springer Science & Business Media, 2012.

[14] P. K. Burgess, P. M. Kulesa, J. D. Murray, and E. C. Alvord Jr. The interaction of growth rates and diffusion coefficients in a three-dimensional mathematical model of gliomas. *Journal of Neuropathology & Experimental Neurology*, 56(6):704–713, 1997.

[15] H. Byrne, T. Alarcon, M. Owen, S. Webb, and P. Maini. Modelling aspects of cancer dynamics: a review. *Philosophical Transactions of the Royal Society of London A: Mathematical, Physical and Engineering Sciences*, 364(1843):1563–1578, 2006.

[16] H. Byrne and M. Chaplain. Mathematical models for tumour angiogenesis: numerical simulations and nonlinear wave solutions. *Bulletin of mathematical biology*, 57(3):461–486, 1995.

[17] M. Cavaglia, S. M. Dombrowski, J. Drazba, A. Vasanji, P. M. Bokesch, and D. Janigro. Regional variation in brain capillary density and vascular response to ischemia. *Brain research*, 910(1):81–93, 2001.

[18] N. Cheng, A. Chytil, Y. Shyr, A. Joly, and H. L. Moses. Transforming growth factor-β signaling–deficient fibroblasts enhance hepatocyte growth factor signaling in mammary carcinoma cells to promote scattering and invasion. *Molecular Cancer Research*, 6(10):1521–1533, 2008.

[19] M. R. Chicoine and D. L. Silbergeld. Assessment of brain tumor cell motility in vivo and in vitro. *Journal of neurosurgery*, 82(4):615–622, 1995.

[20] M. R. Chicoine and D. L. Silbergeld. The in vitro motility of human gliomas increases with increasing grade of malignancy. *Cancer*, 75(12):2904–2909, 1995.

[21] R. Chignola, A. Schenetti, G. Andrighetto, E. Chiesa, R. Foroni, S. Sartoris, G. Tridente, and D. Liberati. Forecasting the growth of multicell tumour spheroids: implications for the dynamic growth of solid tumours. *Cell proliferation*, 33(4):219–229, 2000.

[22] R. Clark. *The molecular and cellular biology of wound repair*. Springer Science & Business Media, 2013.

[23] E. A. Codling, M. J. Plank, and S. Benhamou. Random walk models in biology. *Journal of the Royal Society Interface*, 5(25):813–834, 2008.

[24] T. E. Conturo, N. F. Lori, T. S. Cull, E. Akbudak, A. Z. Snyder, J. S. Shimony, R. C. McKinstry, H. Burton, and M. E. Raichle. Tracking neuronal fiber pathways in the living human brain. *Proceedings of the National Academy of Sciences*, 96(18):10422–10427, 1999.

[25] D. Cotter, D. Mackay, S. Landau, R. Kerwin, and I. Everall. Reduced glial cell density and neuronal size in the anterior cingulate cortex in major depressive disorder. *Archives of general psychiatry*, 58(6):545–553, 2001.

[26] V. Cristini and J. Lowengrub. *Multiscale modeling of cancer: an integrated experimental and mathematical modeling approach*. Cambridge University Press, 2010.

[27] V. A. Cuddapah, S. Robel, S. Watkins, and H. Sontheimer. A neurocentric perspective on glioma invasion. *Nature Reviews Neuroscience*, 15(7):455–465, 2014.

[28] S. E. Eikenberry, T. Sankar, M. Preul, E. Kostelich, C. Thalhauser, and Y. Kuang. Virtual glioblastoma: growth, migration and treatment in a three-dimensional mathematical model. *Cell proliferation*, 42(4):511–528, 2009.

[29] R. Erban, J. Chapman, and P. Maini. A practical guide to stochastic simulations of reaction-diffusion processes. *arXiv preprint arXiv:0704.1908*, 2007.

[30] A. Farin, S. O. Suzuki, M. Weiker, J. E. Goldman, J. N. Bruce, and P. Canoll. Transplanted glioma cells migrate and proliferate on host brain vasculature: a dynamic analysis. *Glia*, 53(8):799–808, 2006.

[31] S. Fedotov and A. Iomin. Migration and proliferation dichotomy in tumor-cell invasion. *Physical review letters*, 98(11):118101, 2007.

[32] R. D. Fields. *The other brain: From dementia to schizophrenia, how new discoveries about the brain are revolutionizing medicine and science*. Simon and Schuster, 2009.

[33] R. A. Fisher. The wave of advance of advantageous genes. *Annals of eugenics*, 7(4):355–369, 1937.

[34] R. Gatenby. Application of competition theory to tumour growth: implications for tumour biology and treatment. *European Journal of Cancer*, 32(4):722–726, 1996.

[35] R. Gatenby, K. Smallbone, P. Maini, F. Rose, J. Averill, R. B. Nagle, L. Worrall, and R. Gillies. Cellular adaptations to hypoxia and acidosis during so-

matic evolution of breast cancer. *British journal of cancer*, 97(5):646–653, 2007.

[36] R. A. Gatenby. Models of tumor-host interaction as competing populations: implications for tumor biology and treatment. *Journal of theoretical biology*, 176(4):447–455, 1995.

[37] R. A. Gatenby and E. T. Gawlinski. A reaction-diffusion model of cancer invasion. *Cancer research*, 56(24):5745–5753, 1996.

[38] R. A. Gatenby and E. T. Gawlinski. The glycolytic phenotype in carcinogenesis and tumor invasion insights through mathematical models. *Cancer research*, 63(14):3847–3854, 2003.

[39] R. A. Gatenby, E. T. Gawlinski, A. F. Gmitro, B. Kaylor, and R. J. Gillies. Acid-mediated tumor invasion: a multidisciplinary study. *Cancer research*, 66(10):5216–5223, 2006.

[40] R. A. Gatenby and R. J. Gillies. Why do cancers have high aerobic glycolysis? *Nature Reviews Cancer*, 4(11):891–899, 2004.

[41] R. A. Gatenby, P. K. Maini, and E. T. Gawlinski. Analysis of tumor as an inverse problem provides a novel theoretical framework for understanding tumor biology and therapy. *Applied Mathematics Letters*, 15(3):339–345, 2002.

[42] A. Giese, R. Bjerkvig, M. Berens, and M. Westphal. Cost of migration: invasion of malignant gliomas and implications for treatment. *Journal of clinical oncology*, 21(8):1624–1636, 2003.

[43] A. Giese, L. Kluwe, B. Laube, H. Meissner, M. E. Berens, and M. Westphal. Migration of human glioma cells on myelin. *Neurosurgery*, 38(4):755–764, 1996.

[44] A. Giese, M. A. Loo, N. Tran, D. Haskett, S. W. Coons, and M. E. Berens. Dichotomy of astrocytoma migration and proliferation. *International journal of cancer*, 67(2):275–282, 1996.

[45] A. Giese and M. Westphal. Glioma invasion in the central nervous system. *Neurosurgery*, 39(2):235–252, 1996.

[46] D. T. Gillespie. Exact stochastic simulation of coupled chemical reactions. *The journal of physical chemistry*, 81(25):2340–2361, 1977.

[47] M. L. Goodenberger and R. B. Jenkins. Genetics of adult glioma. *Cancer genetics*, 205(12):613–621, 2012.

[48] H. Greenspan. Models for the growth of a solid tumor by diffusion. *Stud. Appl. Math*, 51(4):317–340, 1972.

[49] H. Greenspan. On the growth and stability of cell cultures and solid tumors. *Journal of theoretical biology*, 56(1):229–242, 1976.

[50] D. Hanahan and R. A. Weinberg. Hallmarks of cancer: the next generation. *cell*, 144(5):646–674, 2011.

[51] H. L. Harpold, E. C. Alvord Jr, and K. R. Swanson. The evolution of mathematical modeling of glioma proliferation and invasion. *Journal of Neuropathology & Experimental Neurology*, 66(1):1–9, 2007.

[52] H. Hatzikirou, K. Böttger, and A. Deutsch. Model-based comparison of cell density-dependent cell migration strategies. *Mathematical Modelling of Natural Phenomena*, 10(1):94–107, 2015.

[53] H. Hatzikirou, A. Deutsch, C. Schaller, M. Simon, and K. Swanson. Mathematical modelling of glioblastoma tumour development: a review. *Mathematical Models and Methods in Applied Sciences*, 15(11):1779–1794, 2005.

[54] R. Hengeveld. *Dynamics of biological invasions*. Springer Science & Business Media, 1989.

[55] C. C. Hilgetag and H. Barbas. Are there ten times more glia than neurons in the brain? *Brain Structure and Function*, 213(4-5):365–366, 2009.

[56] J. D. Hood and D. A. Cheresh. Role of integrins in cell invasion and migration. *Nature Reviews Cancer*, 2(2):91–100, 2002.

[57] N. E. Humphries, N. Queiroz, J. R. Dyer, N. G. Pade, M. K. Musyl, K. M. Schaefer, D. W. Fuller, J. M. Brunnschweiler, T. K. Doyle, J. D. Houghton, et al. Environmental context explains lévy and brownian movement patterns of marine predators. *Nature*, 465(7301):1066–1069, 2010.

[58] S. Jbabdi, E. Mandonnet, H. Duffau, L. Capelle, K. R. Swanson, M. Pélégrini-Issac, R. Guillevin, and H. Benali. Simulation of anisotropic growth of low-grade gliomas using diffusion tensor imaging. *Magnetic Resonance in Medicine*, 54(3):616–624, 2005.

[59] E. R. Kandel, J. H. Schwartz, T. M. Jessell, et al. *Principles of neural science*, volume 4. McGraw-Hill New York, 2000.

[60] P. J. Kelly and C. Hunt. The limited value of cytoreductive surgery in elderly patients with malignant gliomas. *Neurosurgery*, 34(1):62–67, 1994.

[61] Y. Kim. Regulation of cell proliferation and migration in glioblastoma: new therapeutic approach. *Frontiers in oncology*, 3, 2013.

[62] Y. Kim, S. Lawler, M. O. Nowicki, E. A. Chiocca, and A. Friedman. A mathematical model for pattern formation of glioma cells outside the tumor spheroid core. *Journal of theoretical biology*, 260(3):359–371, 2009.

[63] Y. Kim, S. Roh, S. Lawler, and A. Friedman. mir451 and ampk mutual antagonism in glioma cell migration and proliferation: a mathematical model. *PloS one*, 6(12):e28293, 2011.

[64] J. P. Kirkpatrick and J. H. Sampson. Recurrent malignant gliomas. In *Seminars in radiation oncology*, volume 24, pages 289–298. Elsevier, 2014.

[65] J. Klafter, M. F. Shlesinger, and G. Zumofen. Beyond brownian motion. *Physics today*, 49(2):33–39, 1996.

[66] A. Koob. *The root of thought: unlocking glia–the brain cell that will help us sharpen our wits, heal injury, and treat brain disease.* FT Press, 2009.

[67] M. Kot, M. A. Lewis, and P. van den Driessche. Dispersal data and the spread of invading organisms. *Ecology*, 77(7):2027–2042, 1996.

[68] Y. Kuang, J. D. Nagy, and S. E. Eikenberry. *Introduction to Mathematical Oncology*, volume 59. CRC Press, 2016.

[69] D. A. Lauffenburger and A. F. Horwitz. Cell migration: a physically integrated molecular process. *Cell*, 84(3):359–369, 1996.

[70] M. A. Lewis, S. V. Petrovskii, and J. R. Potts. *The Mathematics Behind Biological Invasions*, volume 44. Springer, 2016.

[71] A. J. Lotka. Undamped oscillations derived from the law of mass action. *Journal of the american chemical society*, 42(8):1595–1599, 1920.

[72] R. Mangum and I. Nakano. Glioma stem cells and their therapy resistance. *J Carcinogene Mutagene S*, 1, 2011.

[73] M. Marín-Padilla. The human brain intracerebral microvascular system: development and structure. *Frontiers in neuroanatomy*, 6:38, 2012.

[74] N. K. Martin, E. A. Gaffney, R. A. Gatenby, and P. K. Maini. Tumour–stromal interactions in acid-mediated invasion: a mathematical model. *Journal of theoretical biology*, 267(3):461–470, 2010.

[75] P. Martin. Wound healing–aiming for perfect skin regeneration. *Science*, 276(5309):75–81, 1997.

[76] N. L. Martirosyan, E. M. Rutter, W. L. Ramey, E. J. Kostelich, Y. Kuang, and M. C. Preul. Mathematically modeling the biological properties of gliomas: A review. *Mathematical biosciences and engineering: MBE*, 12(4):879–905, 2015.

[77] M. Marušić, Ž. Bajzer, J. Freyer, and S. Vuk-Pavlović. Analysis of growth of multicellular tumour spheroids by mathematical models. *Cell proliferation*, 27(2):73–94, 1994.

[78] R. Mayor and S. Etienne-Manneville. The front and rear of collective cell migration. *Nature Reviews Molecular Cell Biology*, 2016.

[79] J. B. McGillen, E. A. Gaffney, N. K. Martin, and P. K. Maini. A general reaction–diffusion model of acidity in cancer invasion. *Journal of mathematical biology*, 68(5):1199–1224, 2014.

[80] V. Montana and H. Sontheimer. Bradykinin promotes the chemotactic invasion of primary brain tumors. *The Journal of Neuroscience*, 31(13):4858–4867, 2011.

[81] J. Murray. Mathematical biology. ii: Spatial models and biomedical applications, volume 17 of interdisciplinary appl. math, 2003.

[82] J. D. Murray. Mathematical biology i: An introduction, vol. 17 of interdisciplinary applied mathematics, 2002.

[83] A. Okubo and S. A. Levin. *Diffusion and ecological problems: modern perspectives*, volume 14. Springer Science & Business Media, 2013.

[84] M. Orme and M. Chaplain. A mathematical model of the first steps of tumour-related angiogenesis: capillary sprout formation and secondary branching. *Mathematical Medicine and Biology*, 13(2):73–98, 1996.

[85] H. G. Othmer, S. R. Dunbar, and W. Alt. Models of dispersal in biological systems. *Journal of mathematical biology*, 26(3):263–298, 1988.

[86] K. Painter and T. Hillen. Mathematical modelling of glioma growth: the use of diffusion tensor imaging (dti) data to predict the anisotropic pathways of cancer invasion. *Journal of theoretical biology*, 323:25–39, 2013.

[87] K. Painter, P. Maini, and H. Othmer. Development and applications of a model for cellular response to multiple chemotactic cues. *Journal of mathematical biology*, 41(4):285–314, 2000.

[88] K. J. Painter, N. J. Armstrong, and J. A. Sherratt. The impact of adhesion on cellular invasion processes in cancer and development. *Journal of theoretical biology*, 264(3):1057–1067, 2010.

[89] K. J. Painter and J. A. Sherratt. Modelling the movement of interacting cell populations. *Journal of theoretical biology*, 225(3):327–339, 2003.

[90] R. Pearl and L. J. Reed. On the rate of growth of the population of the united states since 1790 and its mathematical representation. *Proceedings of the National Academy of Sciences*, 6(6):275–288, 1920.

[91] K. Pham, A. Chauviere, H. Hatzikirou, X. Li, H. M. Byrne, V. Cristini, and J. Lowengrub. Density-dependent quiescence in glioma invasion: instability in a simple reaction–diffusion model for the migration/proliferation dichotomy. *Journal of biological dynamics*, 6(sup1):54–71, 2012.

[92] G. Powathil, M. Kohandel, S. Sivaloganathan, A. Oza, and M. Milosevic. Mathematical modeling of brain tumors: effects of radiotherapy and chemotherapy. *Physics in medicine and biology*, 52(11):3291, 2007.

[93] J. Raizer and A. Parsa. *Current Understanding and Treatment of Gliomas*. Springer, 2015.

[94] I. Rhee, M. Shin, S. Hong, K. Lee, S. J. Kim, and S. Chong. On the levy-walk nature of human mobility. *IEEE/ACM transactions on networking (TON)*, 19(3):630–643, 2011.

[95] A. J. Ridley, M. A. Schwartz, K. Burridge, R. A. Firtel, M. H. Ginsberg, G. Borisy, J. T. Parsons, and A. R. Horwitz. Cell migration: integrating signals from front to back. *Science*, 302(5651):1704–1709, 2003.

[96] R. Rockne, E. Alvord Jr, J. Rockhill, and K. Swanson. A mathematical model for brain tumor response to radiation therapy. *Journal of mathematical biology*, 58(4-5):561–578, 2009.

[97] J. H. Sampson. *The Duke Glioma Handbook*. Cambridge University Press, 2016.

[98] N. Sanai, A. Alvarez-Buylla, and M. S. Berger. Neural stem cells and the origin of gliomas. *New England Journal of Medicine*, 353(8):811–822, 2005.

[99] K. E. Schlageter, P. Molnar, G. D. Lapin, and D. R. Groothuis. Microvessel organization and structure in experimental brain tumors: microvessel populations with distinctive structural and functional properties. *Microvascular research*, 58(3):312–328, 1999.

[100] M. H. Schwarzbach, U. Hinz, A. Dimitrakopoulou-Strauss, F. Willeke, S. Cardona, G. Mechtersheimer, T. Lehnert, L. G. Strauss, C. Herfarth, and M. W. Büchler. Prognostic significance of preoperative [18-f] fluorodeoxyglucose (fdg) positron emission tomography (pet) imaging in patients with resectable soft tissue sarcomas. *Annals of surgery*, 241(2):286–294, 2005.

[101] M. Segarra, B. C. Kirchmaier, and A. Acker-Palmer. A vascular perspective on neuronal migration. *Mechanisms of development*, 138:17–25, 2015.

[102] C. J. Sherr. Cancer cell cycles. *Science*, 274(5293):1672–1677, 1996.

[103] J. A. Sherratt. Wavefront propagation in a competition equation with a new motility term modelling contact inhibition between cell populations. In *Proceedings of the Royal Society of London A: Mathematical, Physical and Engineering Sciences*, volume 456, pages 2365–2386. The Royal Society, 2000.

[104] N. Shigesada and K. Kawasaki. *Biological invasions: theory and practice*. Oxford University Press, UK, 1997.

[105] R. L. Siegel, K. D. Miller, and A. Jemal. Cancer statistics, 2015. *CA: a cancer journal for clinicians*, 65(1):5–29, 2015.

[106] D. L. Silbergeld and M. R. Chicoine. Isolation and characterization of human malignant glioma cells from histologically normal brain. *Journal of neurosurgery*, 86(3):525–531, 1997.

[107] D. L. Silbergeld, R. C. Rostomily, and E. C. Alvord Jr. The cause of death in patients with glioblastoma is multifactorial. *Journal of neuro-oncology*, 10(2):179–185, 1991.

[108] H. Sontheimer. Brain tumors. *Diseases of the Nervous System*, page 259, 2015.

[109] G. S. Stamatakos, V. P. Antipas, and N. K. Uzunoglu. A spatiotemporal, patient individualized simulation model of solid tumor response to chemotherapy in vivo: the paradigm of glioblastoma multiforme treated by temozolomide. *Biomedical Engineering, IEEE Transactions on*, 53(8):1467–1477, 2006.

[110] A. M. Stein, T. Demuth, D. Mobley, M. Berens, and L. M. Sander. A mathematical model of glioblastoma tumor spheroid invasion in a three-dimensional in vitro experiment. *Biophysical journal*, 92(1):356–365, 2007.

[111] A. Stevens and H. G. Othmer. Aggregation, blowup, and collapse: the abc's of taxis in reinforced random walks. *SIAM Journal on Applied Mathematics*, 57(4):1044–1081, 1997.

[112] D. Summers, Z. Y. Wu, and G. C. Sabin. Disturbed nonlinear multispecies models in ecology. *Mathematical biosciences*, 104(2):159–184, 1991.

[113] K. Swanson, E. Alvord, and J. Murray. Virtual resection of gliomas: effect of extent of resection on recurrence. *Mathematical and Computer Modelling*, 37(11):1177–1190, 2003.

[114] K. Swanson, H. Harpold, D. Peacock, R. Rockne, C. Pennington, L. Kilbride, R. Grant, J. Wardlaw, and E. Alvord. Velocity of radial expansion of contrast-enhancing gliomas and the effectiveness of radiotherapy in individual patients: a proof of principle. *Clinical Oncology*, 20(4):301–308, 2008.

[115] K. R. Swanson, E. Alvord, and J. Murray. A quantitative model for differential motility of gliomas in grey and white matter. *Cell proliferation*, 33(5):317–329, 2000.

[116] K. R. Swanson, C. Bridge, J. Murray, and E. C. Alvord. Virtual and real brain tumors: using mathematical modeling to quantify glioma growth and invasion. *Journal of the neurological sciences*, 216(1):1–10, 2003.

[117] M. Tektonidis, H. Hatzikirou, A. Chauvière, M. Simon, K. Schaller, and A. Deutsch. Identification of intrinsic in vitro cellular mechanisms for glioma invasion. *Journal of theoretical biology*, 287:131–147, 2011.

[118] J. P. Tian, A. Friedman, J. Wang, and E. A. Chiocca. Modeling the effects of resection, radiation and chemotherapy in glioblastoma. *Journal of Neuro-oncology*, 91(3):287–293, 2009.

[119] P. Tracqui. From passive diffusion to active cellular migration in mathematical models of tumour invasion. *Acta biotheoretica*, 43(4):443–464, 1995.

[120] P. Tracqui, G. Cruywagen, D. Woodward, G. Bartoo, J. Murray, and E. Alvord. A mathematical model of glioma growth: the effect of chemotherapy on spatio-temporal growth. *Cell proliferation*, 28(1):17–31, 1995.

[121] S. Turner and J. A. Sherratt. Intercellular adhesion and cancer invasion: a discrete simulation using the extended potts model. *Journal of Theoretical Biology*, 216(1):85–100, 2002.

[122] A. Vehlow and N. Cordes. Invasion as target for therapy of glioblastoma multiforme. *Biochimica et Biophysica Acta (BBA)-Reviews on Cancer*, 1836(2):236–244, 2013.

[123] P.-F. Verhulst. Notice sur la loi que la population suit dans son accroissement. correspondance mathématique et physique publiée par a. *Quetelet*, 10:113–121, 1838.

[124] V. Volterra. *Variazioni e fluttuazioni del numero d'individui in specie animali conviventi*. C. Ferrari, 1927.

[125] R. Weinberg. *The biology of cancer*. Garland science, 2013.

[126] D. Wodarz and N. L. Komarova. *Dynamics of cancer: mathematical foundations of oncology*. World Scientific, 2014.

[127] D. Woodward, J. Cook, P. Tracqui, G. Cruywagen, J. Murray, and E. Alvord. A mathematical model of glioma growth: the effect of extent of surgical resection. *Cell proliferation*, 29(6):269–288, 1996.

[128] M. Wurzel, C. Schaller, M. Simon, and A. Deutsch. Cancer cell invasion of brain tissue: guided by a prepattern? *Journal of Theoretical Medicine*, 6(1):21–31, 2005.

[129] V. Zaburdaev, S. Denisov, and J. Klafter. Lévy walks. *Reviews of Modern Physics*, 87(2):483, 2015.

[130] A. Zhigun, C. Surulescu, and A. Hunt. Global existence for a degenerate haptotaxis model of tumor invasion under the go-or-grow dichotomy hypothesis. *arXiv preprint arXiv:1605.09226*, 2016.